ADA062611

AFML-TR-76-81
Part III

LEVEL II

2

DEFECT-PROPERTY RELATIONSHIPS IN COMPOSITE MATERIALS

DDC FILE COPY

DEC 1978
F

VIRGINIA POLYTECHNIC INSTITUTE & STATE UNIVERSITY
BLACKSBURG, VIRGINIA 24061

JUNE 1978

TECHNICAL REPORT AFML-TR-76-81, Part III
Final Report for Period 3 February 1977 – 3 February 1978

Approved for public release; distribution unlimited.

AIR FORCE MATERIALS LABORATORY
AIR FORCE WRIGHT AERONAUTICAL LABORATORIES
AIR FORCE SYSTEMS COMMAND
WRIGHT-PATTERSON AIR FORCE BASE, OHIO 45433

78 12 20 003

When Government drawings, specifications, or other data are used for any purpose other than in connection with a definitely related Government procurement operation, the United States Government thereby incurs no responsibility nor any obligation whatsoever; and the fact that the government may have formulated, furnished, or in any way supplied the said drawings, specifications, or other data, is not to be regarded by implication or otherwise as in any manner licensing the holder or any other person or corporation, or conveying any rights or permission to manufacture, use, or sell any patented invention that may in any way be related thereto.

This report has been reviewed by the Information Office (ASD/OIP) and is releasable to the National Technical Information Service (NTIS). At NTIS, it will be releasable to the general public, including foreign nations.

This technical report has been reviewed and is approved for publication.

NJ Pagano
N. J. PAGANO
Project Engineer
Mechanics & Surface Interactions Br.
Nonmetallic Materials Division

S W Tsai
S. W. TSAI, Chief
Mechanics & Surface Interactions Br.
Nonmetallic Materials Division

FOR THE COMMANDER

J. M. KELBLE, Chief
Nonmetallic Materials Division

Copies of this report should not be returned unless return is required by security considerations, contractual obligations, or notice on a specific document.

AIR FORCE/56780/5 December 1978 — 200

SECURITY CLASSIFICATION OF THIS PAGE (When Data Entered)

REPORT DOCUMENTATION PAGE

READ INSTRUCTIONS
BEFORE COMPLETING FORM

1. REPORT NUMBER
AFML-TR-76-81-(Part III)

2. GOVT ACCESSION NO.

3. RECIPIENT'S CATALOG NUMBER

4. TITLE (and Subtitle)
DEFECT-PROPERTY RELATIONSHIPS IN COMPOSITE MATERIALS. Part III,

5. TYPE OF REPORT & PERIOD COVERED
Final Technical Report,
3 Feb 77 - 3 Feb 78

6. PERFORMING ORG. REPORT NUMBER

7. AUTHOR(s)
K. L. Reifsnider
E. G. Henneke
W. W. Stinchcomb

8. CONTRACT OR GRANT NUMBER(s)
F33615-77-C-5044

9. PERFORMING ORGANIZATION NAME AND ADDRESS
Virginia Polytechnic Institute & State Univ.
Blacksburg, VA 24061

10. PROGRAM ELEMENT, PROJECT, TASK AREA & WORK UNIT NUMBERS
24190313

11. CONTROLLING OFFICE NAME AND ADDRESS
Air Force Materials Laboratory (AFML/MBM)
Air Force Wright Aeronautical Laboratories
Air Force Systems Command
Wright-Patterson Air Force Base, Ohio 45433

12. REPORT DATE
June 1978

13. NUMBER OF PAGES
138

14. MONITORING AGENCY NAME & ADDRESS (if different from Controlling Office)

15. SECURITY CLASS. (of this report)
UNCLASSIFIED

15a. DECLASSIFICATION/DOWNGRADING SCHEDULE

16. DISTRIBUTION STATEMENT (of this Report)

Approved for public release; distribution unlimited.

17. DISTRIBUTION STATEMENT (of the abstract entered in Block 20, if different from Report)

18. SUPPLEMENTARY NOTES

19. KEY WORDS (Continue on reverse side if necessary and identify by block number)

Composite Materials, Graphite-epoxy, Defects, Properties, First Ply Failure, Nondestructive Testing, Delamination, Cracking

20. ABSTRACT (Continue on reverse side if necessary and identify by block number)

This report describes the results of an investigation of the nature of damage in two graphite-epoxy laminates under various loading histories, with special attention to the changes in mechanical properties caused by specific damage mechanisms. The results include several new findings, the development of unique investigative methods and some substantial deviations from common model predictions. The discovery of a "characteristic damage state" is reported.

DD FORM 1 JAN 73 1473 EDITION OF 1 NOV 65 IS OBSOLETE

SECURITY CLASSIFICATION OF THIS PAGE (When Data Entered)

78 12 20 003

PREFACE

This report describes the work completed under Contract F33615-77-C-5044 from the Air Force Materials Laboratory, Wright Patterson AFB between February 7, 1977 and February 6, 1978. The technical monitor of the contract is Dr. N. J. Pagano. All work described herein was executed at Virginia Polytechnic Institute and State University under the direction of Drs. Kenneth L. Reifsnider, Edmund G. Henneke, II and Wayne W. Stinchcomb. The authors gratefully acknowledge the support of the Air Force Materials Laboratory, and the enthusiastic encouragement and guidance provided by Dr. Pagano during the course of this work.

Appreciation is also extended to Phyllis Schmidt for typing this manuscript.

ACCESSION for

A

PRECEDING PAGE BLANK-NOT FILMED

TABLE OF CONTENTS

Section . . . . . . Page

I INTRODUCTION 1

II QUASI-STATIC DEVELOPMENT 5

III LOAD-HISTORY STUDIES 9

Experimental Procedures. 9
Replication Technique. 10
Replication Results. 11
    Type I. 12
    Type II 23
Vibrothermography Results. 27
Characteristics of Specimen Failures 32

IV FATIGUE SERIES 40

V ANALYSIS OF DAMAGE STATES. 56

1. Equilibrium Element Analysis 57
2. Finite Difference Formulation. 72

VI OBSERVATIONS WITH THERMOGRAPHY 91

VII CLOSURE. 130

REFERENCES 132

PRECEDING PAGE BLANK-NOT FILMED

SECTION I

INTRODUCTION

The description and prediction of the degradation and fracture of laminated composite materials presents a special problem. For unnotched laminates the common approach is to apply one of various "failure theories," such as the Tsai-Wu theory, to predict failure of each ply from a phenomenological standpoint. The final fracture strength is usually predicted by reducing the stiffnesses of each failed ply until the last ply breaks, strictly a phenomenological approach. When stress concentrators are present, the so-called notched response must be treated differently, usually by some "adjusted" or "fitted" linear elastic fracture mechanics approach, or a closely related restatement of single-flaw analysis with additional parameters [1]. Neither of these approaches has any direct relationship to the mechanisms of damage development or fracture. Neither of these approaches is sensitive to stacking sequences, edge effects, interlaminar stresses, interlaminar constraint effects on strength, or microstructural detail of any kind. The successes and failures of these two approaches are not the object of this report; there are a considerable number of each.

A rational general approach to the mechanics of failure of laminated composite materials has not been established, primarily because a thorough and complete understanding of damage has not been established, a characteristic damage state or condition has not been identified, and the corresponding mechanics problem has not been set. Indeed, it may not be possible to identify a single characteristic damage state for all laminates, but it is certainly not possible to deal with every crack on an individual basis. Nor can much real progress be made by continued refining of empirical or phenomenological descriptions which have very limited sensitivity to the physical damage involved.

In the context of these remarks, the following are the objectives of the present investigation.

1. To identify the precise nature of damage development in quasi-isotropic graphite-epoxy laminates under various load histories,
2. to determine the physical parameters which lead to a loss of strength and/or life,
3. to establish the mechanics of the individual and combined action of these parameters as they influence mechanical response, and
4. to address the question of how these findings can best be described by analysis.

The purpose of undertaking these objectives is to attempt to develop an understanding of the precise nature of damage so that a rational approach to the mechanics of failure can be determined. The motivations for these activities are both practical and academic. The designer who uses composite laminates, as well as the academician, should be able to predict laminate response from lamina response, to estimate notched or unnotched strength accurately, to estimate life, to predict the change in stiffness of a component, and to design materials and material systems for specific service (including reliability) specifications.

The approach to these objectives is two-fold. An experimental investigation of the precise nature of damage in AS3501 graphite epoxy laminates having stacking sequences of $[0,\pm 45,90]_s$ (hereafter called type I) and $[0,90,\pm 45]_s$ (hereafter called type II) was performed under quasi-static and cyclic loading. The following investigative techniques were used.

1. Light microscope observations during loading
2. Scanning electron microscope observations
3. Replication of surface damage patterns
4. Sequence sectioning with replication
5. Ultrasonic attenuation measurement
6. Acoustic emission measurement
7. Dynamic and static stiffness change observations
8. Video-thermography observations

The second part of the approach is analytical. The computations are used to assist in the interpretation of the data and the development of models, and the representation of the damage process. These activities have included:

1. two and three-dimensional finite element analyses of stress states in the composite laminates
2. a one-dimensional model of a characteristic damage state
3. and a three-dimensional finite difference solution of the stress balance equations for a variety of cracked-ply problems.

Some of the details of earlier work can be found in references [2-6]. A listing of material and mechanical properties appears in Table I and Table II, respectively.

TABLE I

ROOM TEMPERATURE MATERIAL PROPERTY DATA
TYPE AS/3501 GRAPHITE EPOXY

Property	Type I(1)	Type II(2)
Average 0° Tensile Strength (KSI)	232	225
Average 0° Tensile Modulus (MSI)	20.0	19.4
Fiber Volume (%)	63.8	60.4
Resin Content (%)	28.87	31.95
Density (lb/in.^{3})	0.0577	0.0570
Void Content (%)	0.13	0.04
Ply Thickness (in.)	0.0054	0.0054

(1) Panel No. 2206
(2) Panel No. 2506

TABLE II

AVERAGE MECHANICAL PROPERTIES OF
GRAPHITE EPOXY LAMINATES

Property	Type IA	Type IB	Type II
Elastic Modulus (MSI)	6.6	6.8	6.1
Tensile Strength (KSI)	72.6	65.8	70.5
Fracture Strain (μ in/in)	11,700	10,400	11,400

SECTION II

QUASI-STATIC DAMAGE DEVELOPMENT

Quasi-static tensile loading of the type I ($[0,\pm45,90]_s$) and type II ($[0,90,\pm45]_s$) laminates has been used to obtain basic data regarding the development of damage. Various details of this aspect of the investigation have been reported earlier [2-6]. Some additional results will appear in other sections of this report. In this section we will restrict our discussion to a particular type of static test recently initiated.

The test series to be discussed consists of step loading under displacement control with various nondestructive tests being run at each test interruption. These load steps are decreased in magnitude as the absolute load value increases, continuing to fracture. The objective of these tests is to study the development and interaction of damage in the latter stages of loading, especially the events immediately preceding fracture. Special attention is directed to the nature of the region where the final fracture event occurs in an attempt to identify any unique characteristics of that area of damage.

During loading of the specimens a thermographic camera was used to observe the transient energy release when damage events occurred. The largest such event is the final fracture which was recorded in each case. The nature of the energy release during final fracture, as indicated by the heat pattern and its subsequent changes, indicates the details of the damage involved in the final failure event. In particular, information regarding the location of failure initiation and the dynamic wave propagation associated with final fracture can, and have been determined using this videothermography technique. Since these results are still preliminary only general reference will be made to them at the end of this section.

Acoustic emission was also monitored during these tests. The equipment used is fairly standard. Emission events in the kilohertz range were recorded for the most part, and those events seem to correlate with other indications of damage development.

The major technique used to obtain damage records during these tests was (and is) surface replication. As described earlier, this method consists of placing cellulose acetate tape, softened by an acetone solution, in contact with the edge of a specimen, letting it dry, and then peeling it off for observation or reproduction. This technique allows us to obtain permanent records of all damage events along the specimen length for many situations, including different load levels, different load histories, and numerous tests. We have found no other method that allows the recovery of such a large volume of data with such fidelity to detail. Only this method allows us to generate the data base of types and numbers of cracks along with chronology and interactive detail necessary to firmly establish the precise nature of damage in a relatively short period of time. Examples of the crack patterns obtained with this method are shown in Figs 2-1 and 2-2. Both of these patterns were recorded at loads which were about 97 percent of the final break strength. The damage patterns are fairly typical of those observed on other occassions in the region which subsequently fractures. From data of that sort, and from data developed by the other methods described above, the following preliminary observations are made.

1. The type of damage that occurs is controlled by load level, but the number of incidences of each damage type is not the same from specimen to specimen for a given load level.

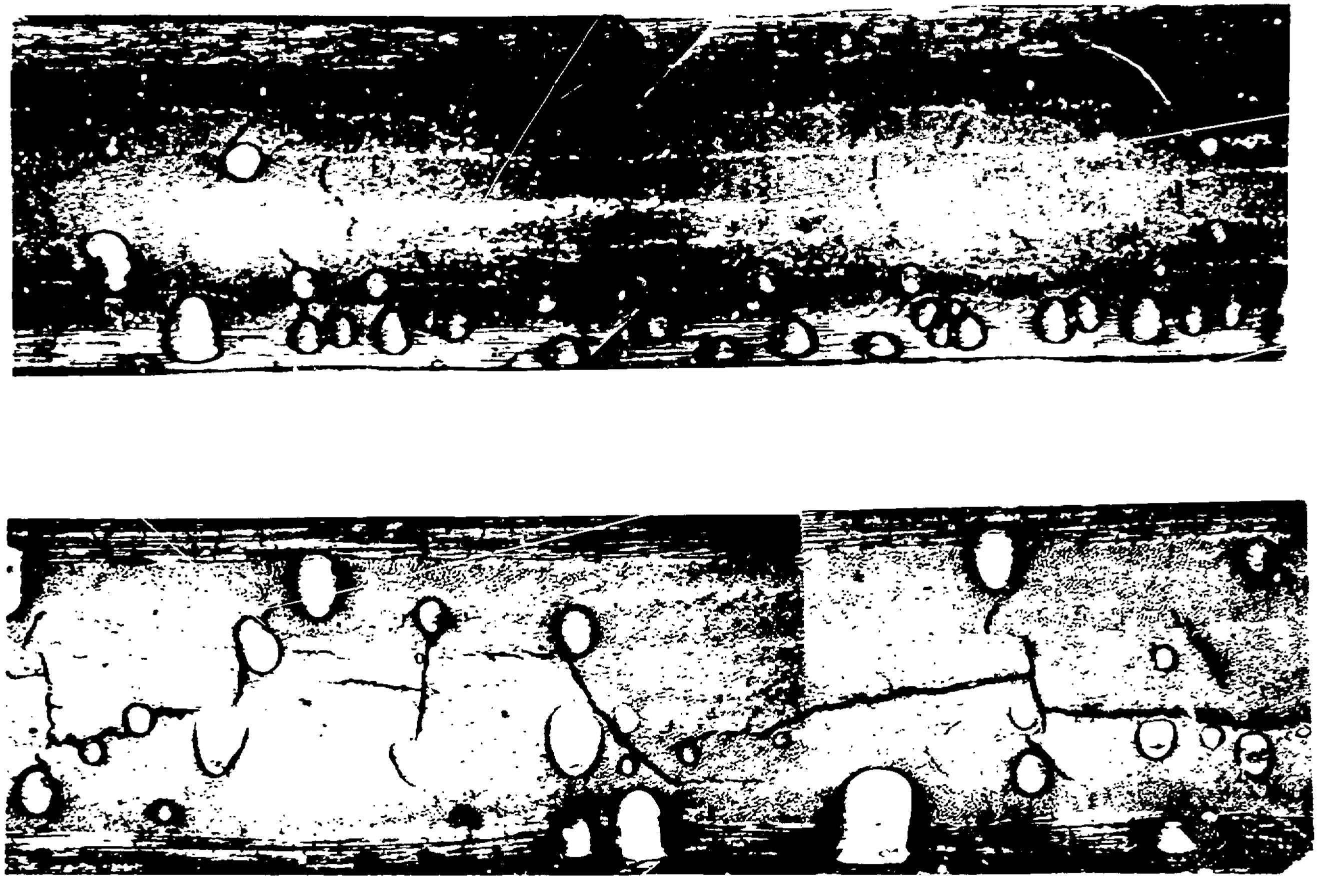

Fig. 2-1 and 2-2 Prefracture replica patterns

2. The number of incidences of a given damage type is less for quasi-static loading than for cyclic loading at a given load level.
3. The load-relaxation curves during hold periods (with displacement constant) were continuous; no single events could be distinguished by abrupt discontinuities.
4. The amount of damage initiation as a function of load increases sharply at median load levels then drops off to nearly zero near the fracture load. This is supported by replication data, by acoustic emission data, and by the amount of load relaxation during hold times.
5. Regions of high crack density and high crack connectivity form at localities which become the final fracture sites.
6. Some longitudinal cracking, delamination or debonding is nearly always present in the specimen prior to failure but there is no evidence that this mode of damage is directly involved in the final fracture event.
7. Thermographic records of final fracture have indicated that fracture initiated in the center of the width of the specimen in one case. In other cases a precise determination of fracture initiation position was not possible; in some cases the data suggested that fracture began at the edge of the specimen. The thermographic patterns, and their dissipation after fracture, do indicate the nature of the fracture-damage events, their magnitude and distribution.

SECTION III

LOAD-HISTORY STUDIES

The main objectives of this phase of the investigations were to apply the replication technique to document the effect of load history on damage development in the type I and type II laminates and to provide a detailed description of damage initiation, growth, and interactions. Damage was initiated in the laminates by tensile static loading of the specimens to various stress levels and then caused to grow by tension-tension fatigue cycling. Observations include the types of damage or cracking that occur and their growth and interactions with respect to the stress levels and repeated cycling.

Experimental Procedures

In the experimental investigation, uniform cyclic stresses were applied at a frequency of 1 Hz and a stress ratio R=0.1. The data reported are for maximum cyclic stresses of 234, 290, and 393 MPa, although other stress levels have been investigated. The three stress levels in this study represent cyclic stresses below, approximately equal to, and above the proportional limit, or knee, in the static stress-strain curve. Quasi-static preloads were applied using a 89 kN (20 kip) Instron machine at a crosshead displacement rate of 1.3 mm/min (0.05 in./min.) Load and strain gage data were recorded. Each test was stopped at 890 N (200 lbs.) and again at the load corresponding to the maximum cyclic load to be used in the fatigue test. While the crosshead was stopped, replicas were made of the free edges of the specimen. The replication technique is described in a later paragraph.

After the static preloads, each specimen was fatigued using an extensometer to measure strain over a 2.54 cm (1.0 in.) gage length. Cyclic testing was performed on an MTS servo-hydraulic, closed-loop machine with a tensile capacity of 89 kN (20 kips). Material responses were continuously monitored by a Tektronix WP 1100 data acquisition system. By sampling load and strain data, the system calculated and recorded maximum load, maximum strain, dynamic compliance, dissipated energy, and the specific damping ratio at preselected numbers of cycles. The maximum stress, in each case, corresponded to the preload stress. All the 234 and 290 MPa specimens were fatigued 10,000 cycles, and 500 cycles were applied to the 393 MPa specimens. The tests were stopped after 50, 500, 5000, and 10,000 cycles in order to make replicas of the loaded specimen edges. For the 393 MPa specimens, replicas were made after 50, 100, and 500 cycles.

Upon completion of the fatigue loading, strain gages were again mounted in the center of each specimen. The specimens were then loaded to failure at the same rate used for the static preloads. Load-strain curves were plotted to determine final stiffness and residual strengths.

Replication Technique

In the study of edge damage it is essential to have a quick, reliable method of permanently recording damage occurrences. Without such a method it is impossible to make extensive microscopic examination of the edges and draw reliable conclusions concerning load-damage history. An essential requirement of any such technique is that it must be capable to being performed on specimens that are mounted in a testing machine and subjected to load. This requirement makes it possible to monitor the development of damage due to static or fatigue loadings by making recordings at intervals throughout the test. In addition, these recordings or replicas made while the specimen is under load will contain the damage in its most enlarged or opened state. If the replication was made after the load was removed from the specimen, many of the smaller cracks would close and perhaps go undetected. Another necessary requirement is that the technique possess sufficient resolution to allow detection of the smallest cracks. Magnifications of forty power appear sufficient to detect all transverse cracks and delaminations as well as individual fiber bundles.

The replication technique is adapted from one used in microscopy for duplicating small areas of surfaces that are not suitable for direct observation. The replica is made by softening one side of a strip of 10 mil cellulose acetate replicating tape with acetone and pressing the tape against the edge of the specimen. It was found that the best way to make instantaneous replicas without slippage of the replicating tape was to fasten the tape in place along the edge of the specimen before applying any acetone. The acetone was evenly applied along the specimen-tape interface by injecting an even stream of acetone along the interface with a hypodermic syringe. After carefully removing the replica from the specimen, it can be examined in a microscope or used as a negative, along with a photographic enlarger, to make photographs of the damage along the entire edge of the specimen under load.

Replication Results

Although the interior inplane stresses in the two laminates are nearly identical, the out-of-plane stresses near the free edges are quite different not only in magnitude and distribution but in sign in the case of the normal stress σ_z. With different stress states in the material near the free edges, it is reasonable to expect different damage states to develop in the two quasi-isotropic laminates under load. The replicas reveal that this is indeed the case. Furthermore, by aligning replicas made at successive cyclic intervals side-by-side, the damage history of various regions can be traced, as shown for the following specimens:

Type I

Figure 3.1a represents a 5 mm (0.20 in.) length along the edge of a type I specimen at the 234 MPa static preload (1/2 cycle). Arrow 1 points out one of the four transverse cracks present in this region after the static preload had been applied. These cracks span the two inner 90° layers. The long white lines (arrow 2) are not cracks but are scratches left in the specimen by the cutting process in which the specimens are cut from larger panels. These saw marks are seen in many of the replicas. Figure 3.1b is of the same location as (a) but after 50 cycles. There are no changes except for a small "hooked" crack (arrow 3) that has branched into one of the inner 45° layers. Arrow 4 points out a piece of dust or lint that has stuck to the replica. Some experience is required to properly interpret the information that a replica contains. Confusing areas will be pointed out so that they will not distract from the value of the replication technique itself. As can be seen in Fig. 3.1c, arrow 5, an additional transverse crack has formed after 10,000 cycles. There is also a delamination along the -45°/90° interface at the bottom of the picture. A transverse crack has caused it to jump to the opposite 90°/-45° interface and then the crack at

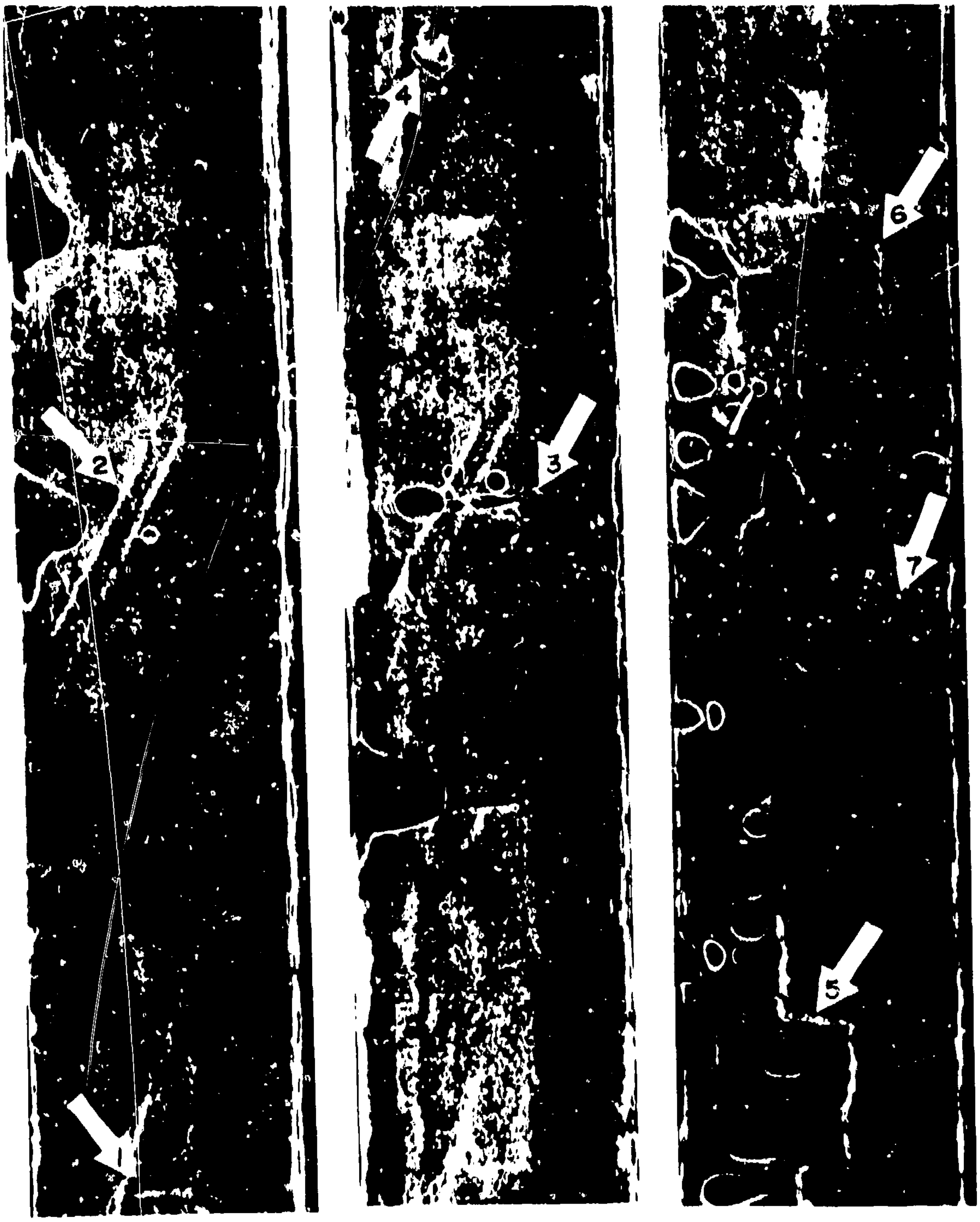

a) Static b) 50 Cycles c) 10,000 Cycles

Fig. 3-1 Damage along the edge of a type I specimen at 234 MPa after a) static preload, b) 50 cycles, c) 10,000 cycles

arrow 5 has caused it to jump back again. From the top of the picture a delamination along the 90°/90° interface appears to have grown downward until it was stopped by another transverse crack. In this case, instead of jumping to another interface, small "branch" delaminations begin to grow from the tips of the transverse crack along the +45°/-45° interfaces (arrow 6). The transverse crack below this also has branch delaminations originating from its crack tips as well as a small longitudinal crack which has grown into its center. This longitudinal crack may be the beginning of a major delamination. Other points of interest in this picture are the cracks through the outer + 45° layers that stem from the branch delaminations. One of these four cracks is pointed out by arrow 7.

Figure 3.2 contains an excellent illustration of the turning effect that a transverse crack can have on a delamination. Arrow 1, in Fig. 3.2a, points out a transverse crack with a hooked crack that hooks in the same direction in which the delamination is growing. As a result of this and the fact that the delamination is in the lower 90°/-45° interface, it is turned and forced down into the -45°/+45° interface (arrow 2). If the delamination had approached the transverse crack from the 90°/90° interface, it probably would have stopped at the crack and caused extensive growth of the branch delaminations. If the hooked crack had turned in the opposite direction from the delamination growth, then the delamination would probably have jumped to the upper -45°/90° interface. Both of these "if" conditions were illustrated in the previous figure. Also of interest in Fig. 3.2b are the four transverse cracks that have hooked cracks through the inner -45° layers but which are offset from the crack tip at the -45°/90° interface (arrow 3 points out one of these).

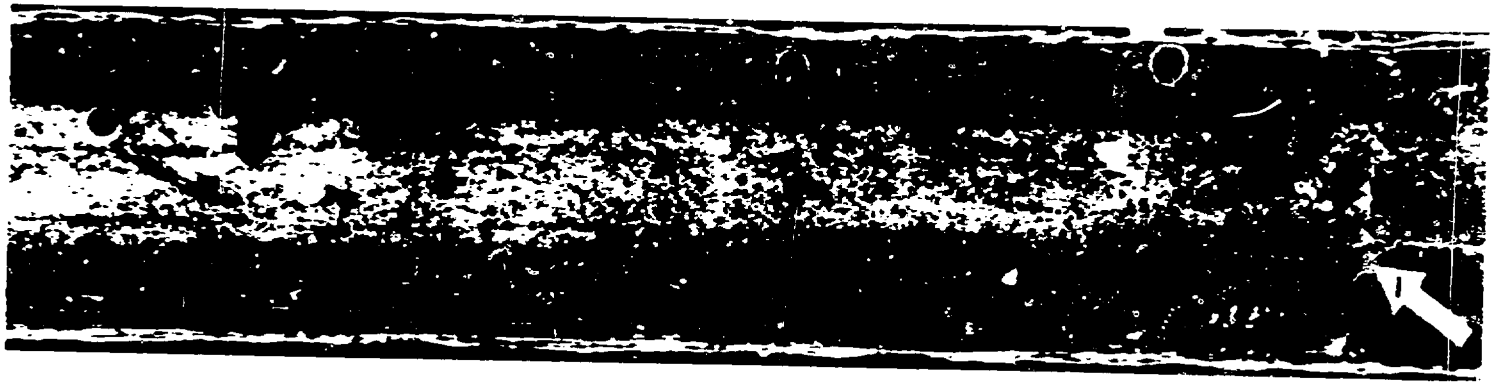

a) 50 Cycles

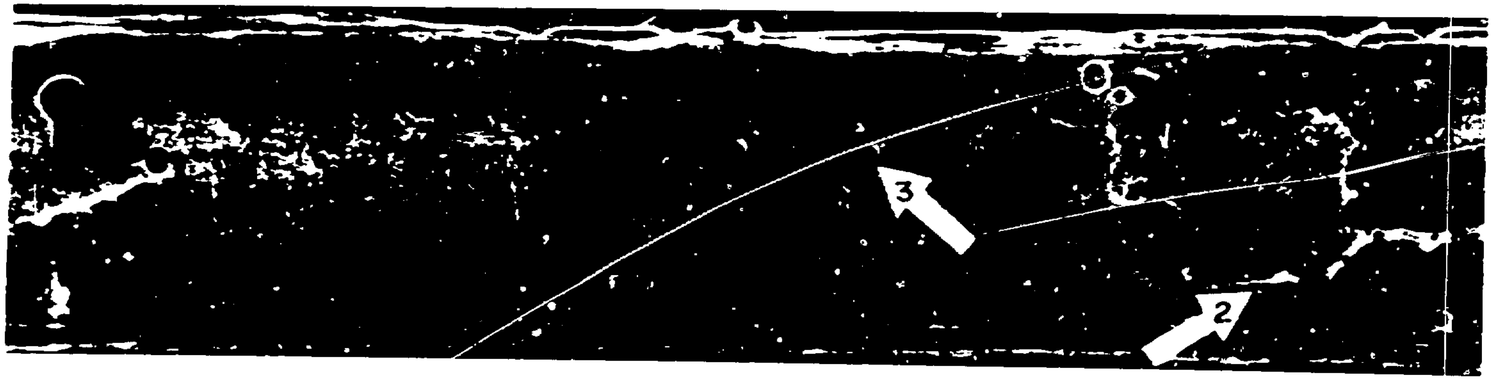

b) 10 000 Cycles

Fig. 3-2 Damage along the edge of a type I specimen at 234 MPa after a) 50 cycles, b) 10,000 cycles

A third section of this same 234 MPa specimen is shown in Fig. 3.3. The main purpose of this figure is to illustrate the magnitude of the delamination width at the most severe location. In (a), the delamination growing along the 90°/90° interface from the right hand side has been stopped by a transverse crack and a branch delamination has formed. However, after 10,000 cycles (Fig. 3.3b), it can be seen that the delamination broke through the crack and continued its growth. As observed earlier, there is no jumping between interfaces due to the transverse crack if the delamination is along the midplane. The branch delamination appears to stop growing when the delamination breaks through the parent transverse crack. Arrows 1 and 2 point out longitudinal cracking that has occurred prior to delamination as seen in (b), these cracks determine the path that the delamination will take. The delaminations from the left and right have continued to grow and finally met at the transverse crack pointed out by arrow 3.

The characteristics of the damage development observed in the 234 MPa specimen are also observed in the 290 MPa specimen, however, some of the individual phenomena and details, such as branch delamination and longitudinal cracking, appear more pronounced. For example, Fig. 3.4 represents a sequence of events from the 290 MPa specimen. In (a), it can be seen that this particular location on the specimen contained only one transverse crack. After 50 cycles, (b) indicates four, possibly five, transverse cracks, as well as three distinct hooked cracks in the inner -45° layer. One of these (arrow 1) does not appear to be associated with a parent transverse crack. Arrow 2 points out a turning point in the delamination. This may have been caused by a slanted or angle crack, a portion of which is visible above the turning point.

a) 50 Cycles

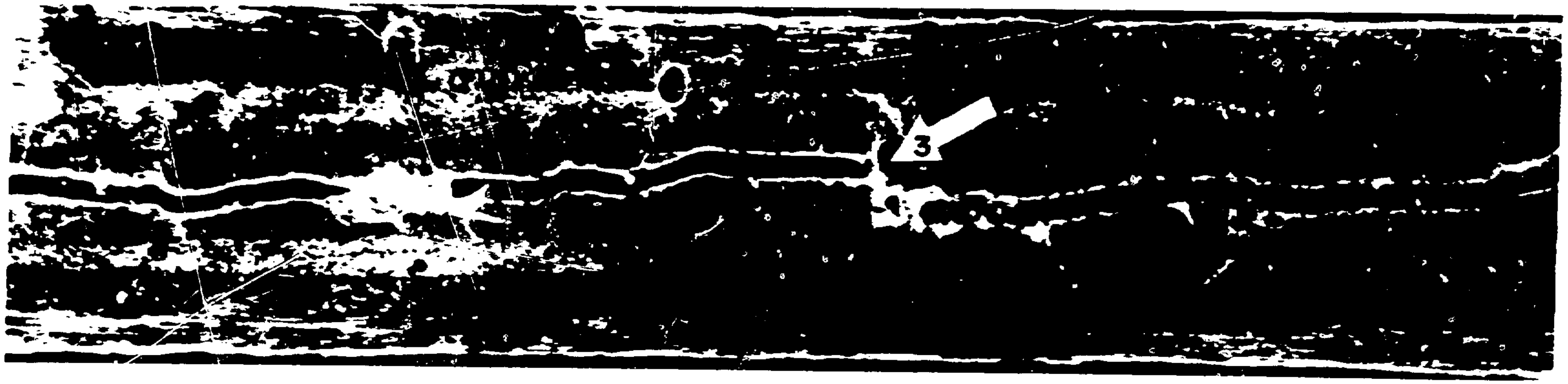

b) 10 000 Cycles

Fig. 3-3 Delamination in a type I specimen at 234 MPa after
a) 50 cycles, b) 10,000 cycles

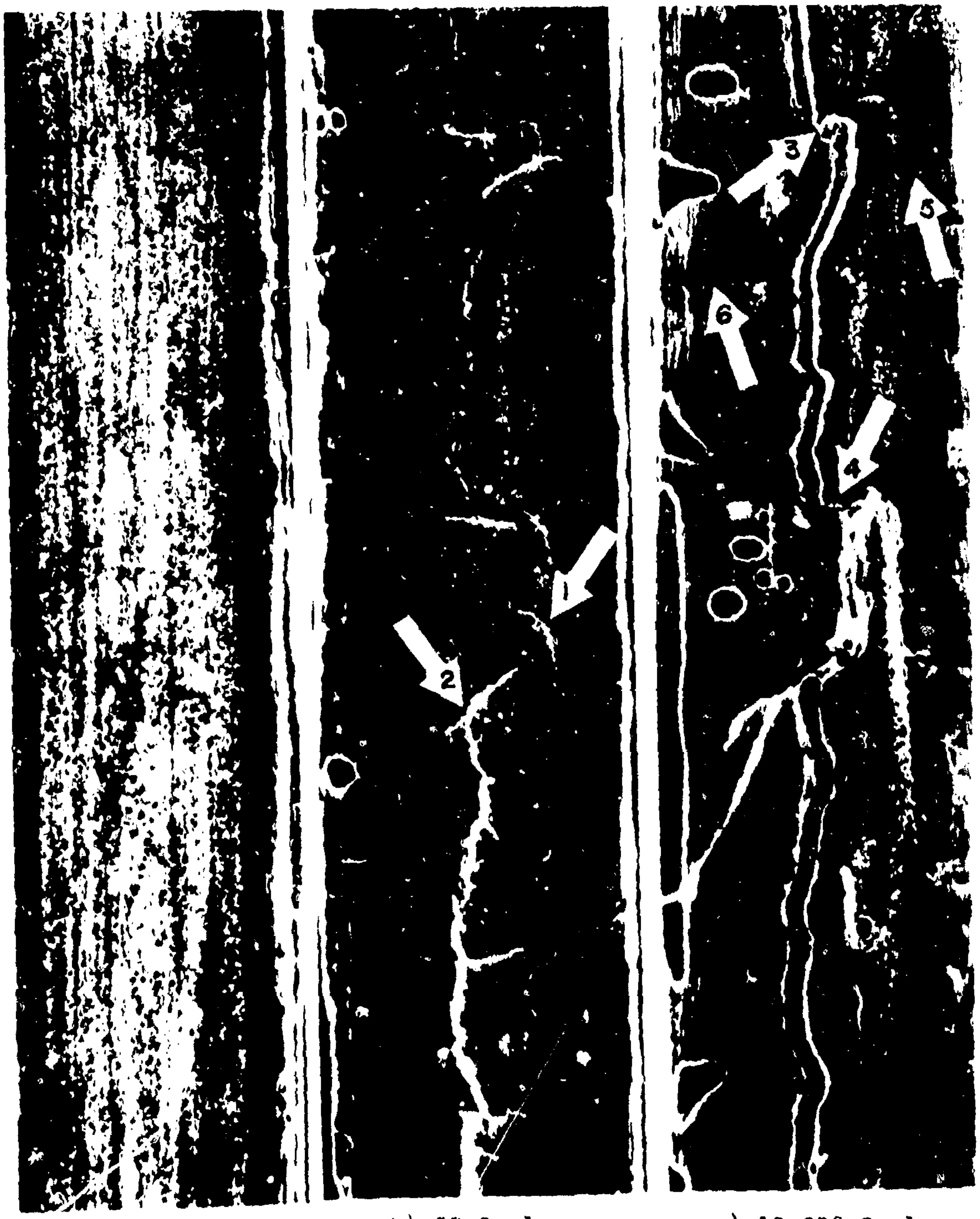

a) Static b) 50 Cycles c) 10 000 Cycles

Fig. 3-4 Damage along the edge of a type I specimen at 290 MPa after a) static preload, b) 50 cycles c) 10,000 cycles

After 10,000 cycles, a delamination has grown down from the top and stopped at a transverse crack (arrow 3). A small branch delamination formed; however, the major delamination did not continue. If it had done so, it would have continued straight along the 90°/90° interface. It appears that another delamination, independent of both the upper and lower ones, has bridged the gap between the transverse cracks at arrows 3 and 4. This delamination then caused the long branch delamination. Finally, the lower delamination grew upward to the transverse crack at arrow 4. Arrows 5 and 6 indicate the areas where the specimen fractured.

The most extreme case of branch delamination found in the 290 MPa specimen is shown in Fig. 3.5. Since the delamination did not break through the transverse crack, the branch delaminations had the time necessary to grow to such proportions. Consequently, when the specimen was loaded to failure, it fractured at this spot. The three arrows in this figure point out dust or lint that is stuck to the replica and should not be mistaken for cracks.

Figures 3.6 and 3.7 are of the 393 MPa specimen. The characteristics of damage development discussed for the previous specimens are found to be the same for this specimen. Even though it was only fatigued for 500 cycles, the amount of damage is similar to the 290 MPa specimen after 10,000 cycles, except that delaminations are more extensive. There is approximately 97 percent delamination for the 290 MPa specimen and 100 percent for the 393 MPa specimen but its maximum crack width is more than twice as large. As can be seen in Fig. 3.6a, a large number of transverse cracks occur when the specimen is loaded to the static preload. The spacing between these cracks is representative of the entire specimen. It tends to vary from about the thickness of the laminate

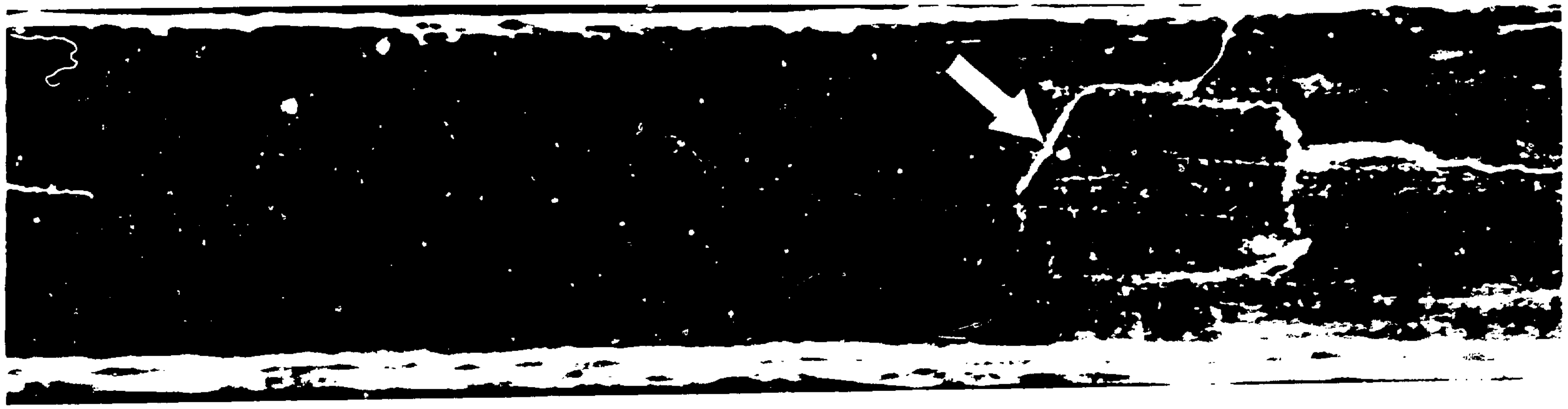

a) 500 Cycles

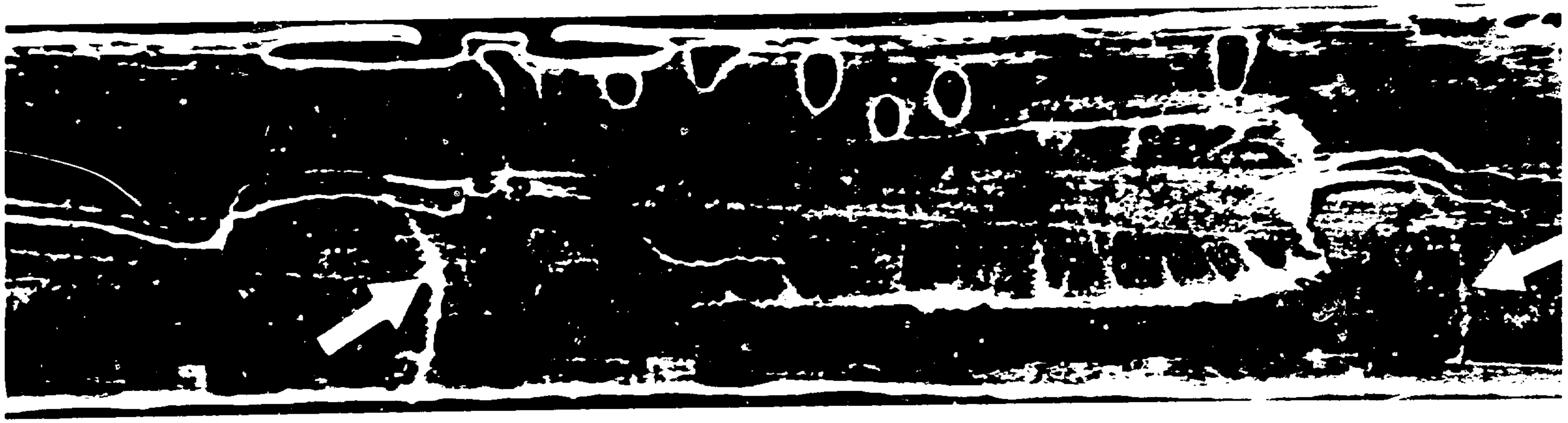

b) 10 000 Cycles

Fig. 3-5 Delamination of ±45° interface at 290 MPa after
a) 500 cycles, b) 10,000 cycles

a) Static

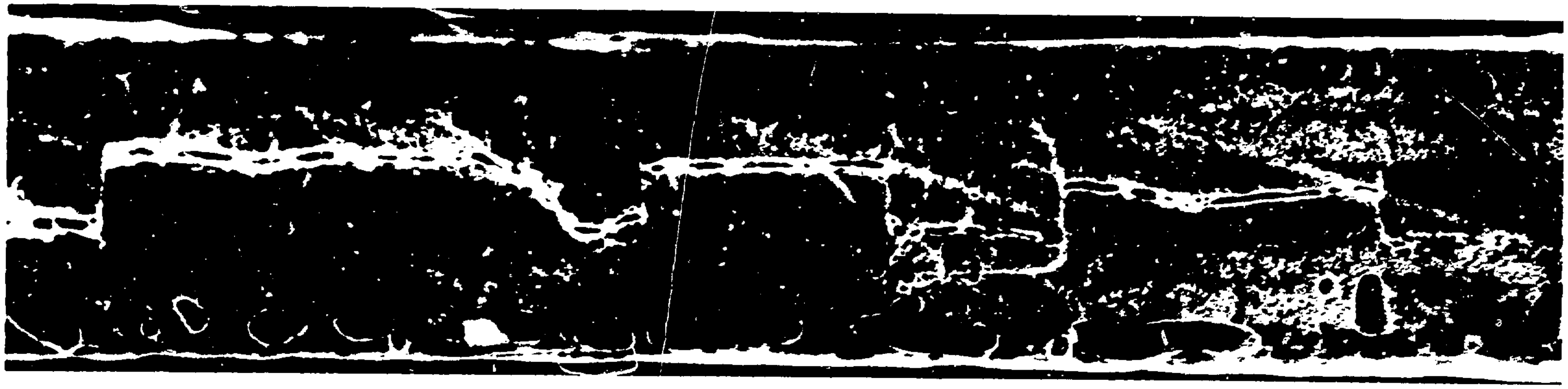

b) 50 Cycles

Fig. 3-6 Damage along the edge of a type I specimen at 393 MPa after a) static preload, b) 50 cycles

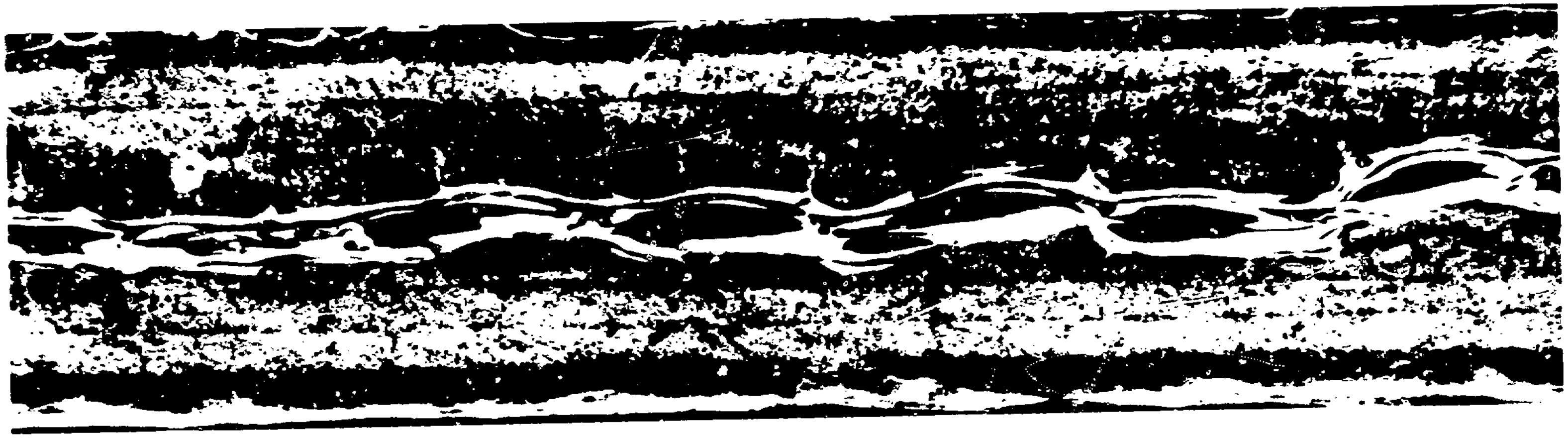

a) Static

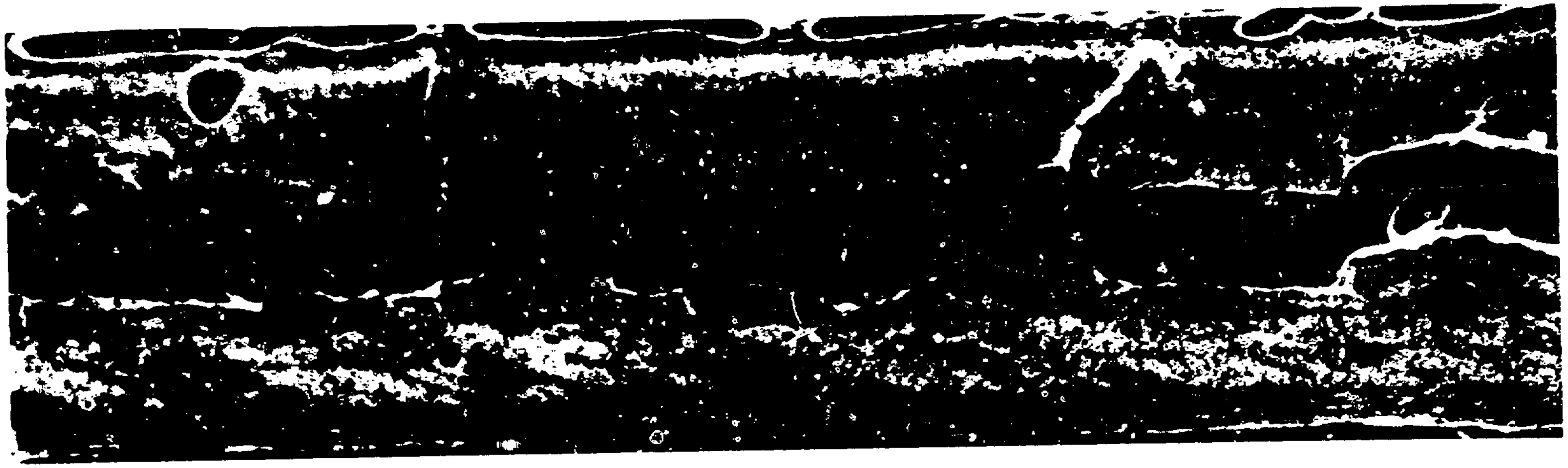

b) 50 Cycles

Fig. 3-7 Delamination in a type I specimen at 393 MPa after a) static preload, b) 50 cycles

down to a third of the thickness. No new transverse cracks formed after the preload. It has been observed for all type I specimens, regardless of load, that once an area has been delaminated, no new transverse cracks are formed. Arrow 1 indicates a slanted or angle crack which influences the path of the delamination, as can be seen in (b). Figure 3.7 illustrates the magnitude of the most severe crack opening. The 50 cycle replica is shown here because it is of much better quality than the 500 cycle replica. For this particular specimen, the crack width of the delamination was largest near the center and near the tab regions of the specimen.

Type II

In many ways the damage development in type II specimens is similar to type I, but there are also many differences. For example, the crack opening or width in type II material is much smaller and this makes the cracks more difficult to observe. A method, such as the replication technique, which allows observation of the specimen while subjected to maximum load, is essential.

A sequence of photographs of replicas from the 234 MPa, type II specimen is shown in Fig. 3.8. The two 90° layers are no longer together, but are adjacent to the two outer 0° layers. As with the type I material, the first damage that occurs is transverse cracking in the 90° layers. However, the cracks are only half the length of those in type I specimens; thus, they are more difficult to observe. Arrows 1 and 2 in (a) point out two of the six, or possibly more, transverse cracks present. An interesting observation is the epoxy-rich area pointed out by arrow 3. This may have been the "joint" between two pieces of prepreg tape that filled with epoxy as the material was cured. After 50 cycles, a

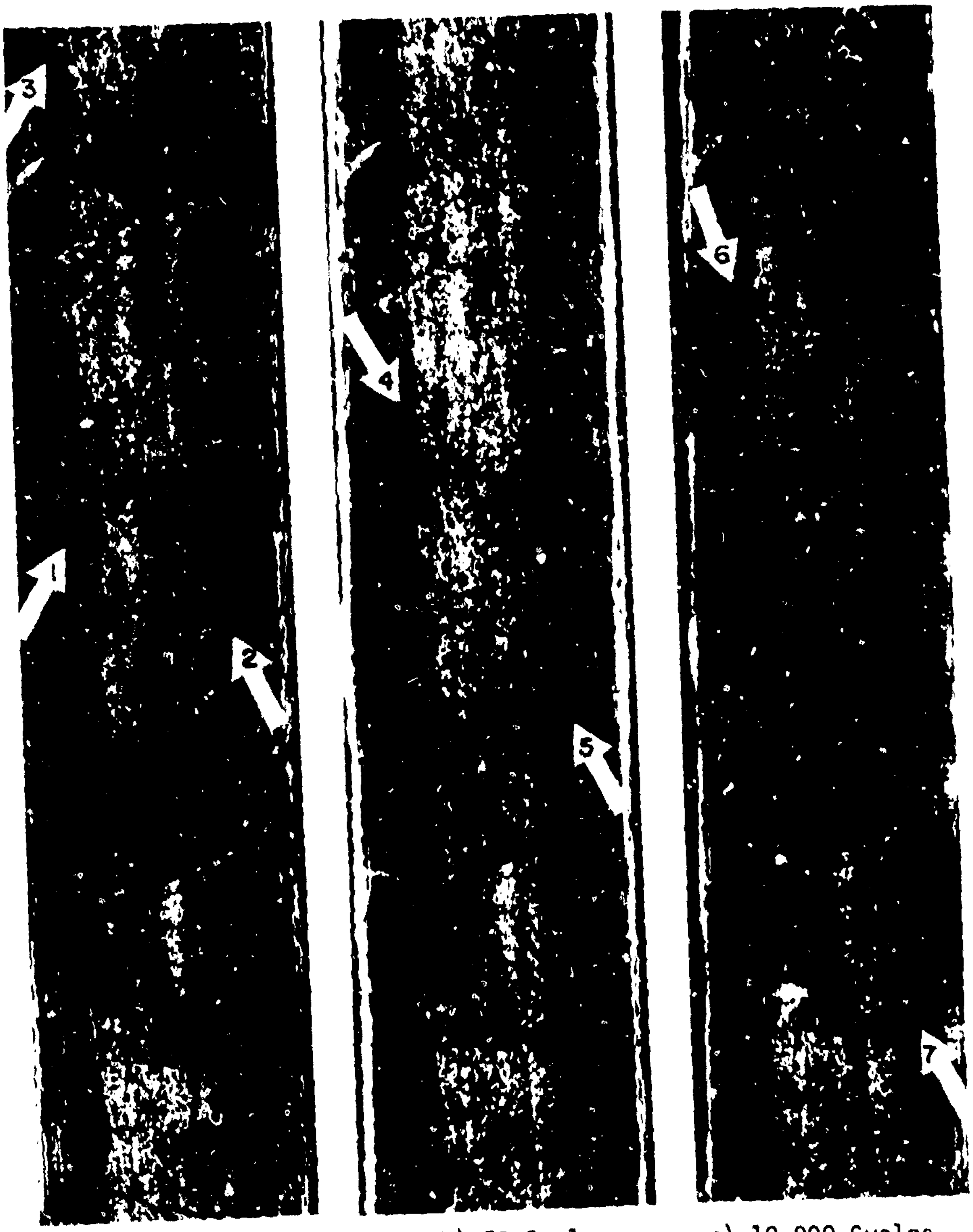

a) Static b) 50 Cycles c) 10 000 Cycles

Fig. 3-8 Damage along the edge of a type II specimen at 234 MPa after a) static preload, b) 50 cycles, c) 10,000 cycles

few additional cracks have formed, two of which are pointed out by arrows 4 and 5. Similarly, after 10,000 cycles, still more cracks have formed, two of which are indicated by arrows 6 and 7. The spacing of the two cracks at arrow 7 is about the thickness of one layer. This is about three times closer than any transverse cracks observed in the type I specimens.

A static preload of 290 MPa does not appear to cause much more damage than in the 234 MPa case (Fig. 3.9a). Arrows 1 and 2 indicate two of the transverse cracks present. The long black line is not a defect in the specimen, but is a deep scratch in the replica. After just 50 cycles (Fig. 3.9b), an extremely large number of cracks have formed. Many of these are spaced at a distance roughly equivalent to the thickness of one individual layer. A few of the cracks have even grown into the adjacent 45° layers (arrows 3 and 4). This characteristic was also observed in the type I specimens. It appears that few, if any, additional transverse cracks had formed in the 90° layers by 10,000 cycles (Fig. 3.9c), even though this is difficult to determine precisely due to the poor quality of this photograph. Of great interest, however, are the small delaminations that have begun to grow along the +45°/-45° interfaces (arrows 5 and 6). At arrow 6 there is even a small transverse crack beginning to develop in the inner -45° layer. The branch delaminations in the type I specimens grew along the same +45°/-45° interfaces.

Figure 3.10 is of two different areas on this same 290 MPa specimen after 10,000 cycles. The arrow on (a) indicates one of the three transverse cracks through the inner -45° layers. These cracks are connected to cracks through the outer +45° layers by the +45°/-45° interface

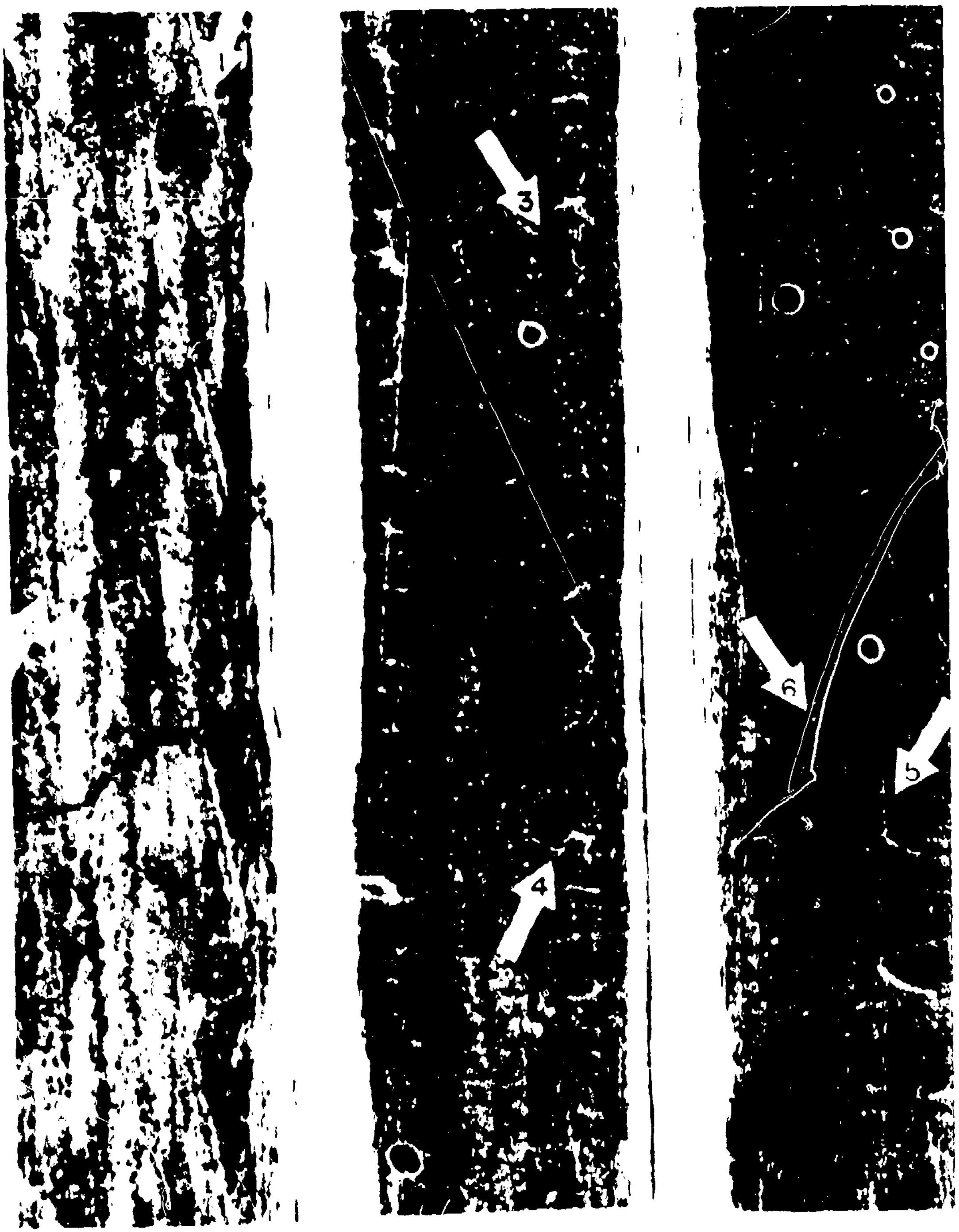

a) Static b) 50 Cycles c) 10 000 Cycl

Fig. 3-9 Damage along the edge of a type II specimen at 290 MPa after a) static preload, b) 50 cycles, c) 10,000 cycles

delaminations. This combination of cracking involves six of the eight layers of the specimen. Figure 3.10b is of an area near the tabs. These are the only regions in which such extensive longitudinal cracking occurs. This may be caused by an unresolved moment created by shear stresses between the grip wedges and the tabs.

After a static preload of 393 MPa, there is extensive cracking in the 90° layer (Fig. 3.11a). In addition, there are many cracks through the outer +45° layers and at least five cracks through the inner -45° layers, one of which is indicated by arrow 1. In Fig. 3.11b, after 50 cycles, it can be seen that the cracks in the 90° layers have opened up and have become more obvious, but there appear to be few, if any, additional cracks. The same holds true for the cracks in the outer +45° layers. Two new cracks have formed in the inner -45° layers. The spacing of these cracks is very similar to the spacing of the transverse cracks in the 90° layers for the type I specimens. After 500 cycles, little change has taken place. The cracks seemed to have opened up slightly and some additional delamination has grown along the +45°/-45° interface (arrow 2).

As was the case for the type I material, these replicas provided very consistent and detailed information concerning the types of edge damage, their interactions, and a chronological ordering of their development. This knowledge is essential to understanding the behavior of these materials.

Vibrothermography Results

The results of the vibrothermography technique (described in another section of this report) were very conclusive in terms of locating

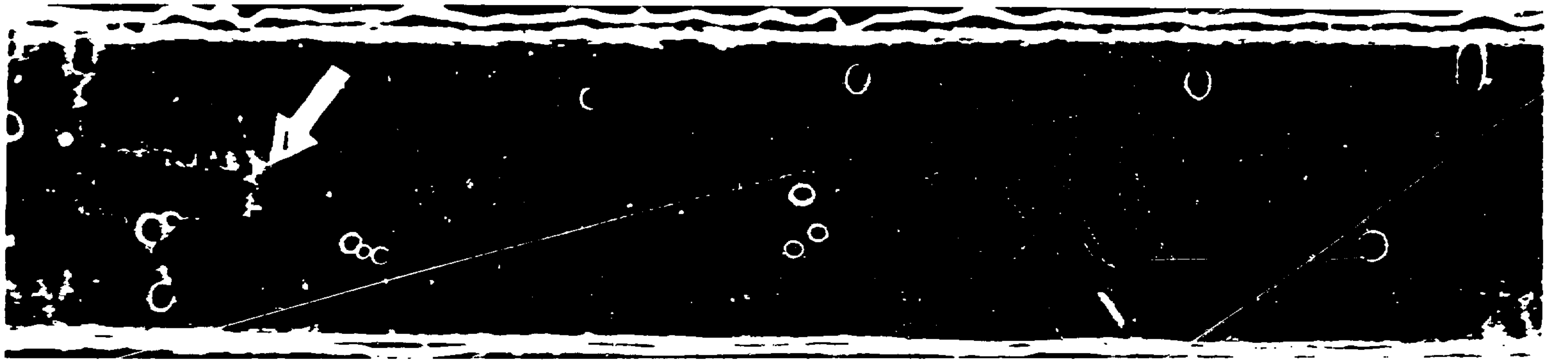

a) 10 000 Cycles

b) 10 000 Cycles

Fig. 3-10 a) Combination of cracks and delaminations through the interior six plies of a type II laminate at 290 MPa after 10,000 cycles.
b) Longitudinal cracking near the end tabs in a type II specimen at 290 MPa after 10,000 cycles

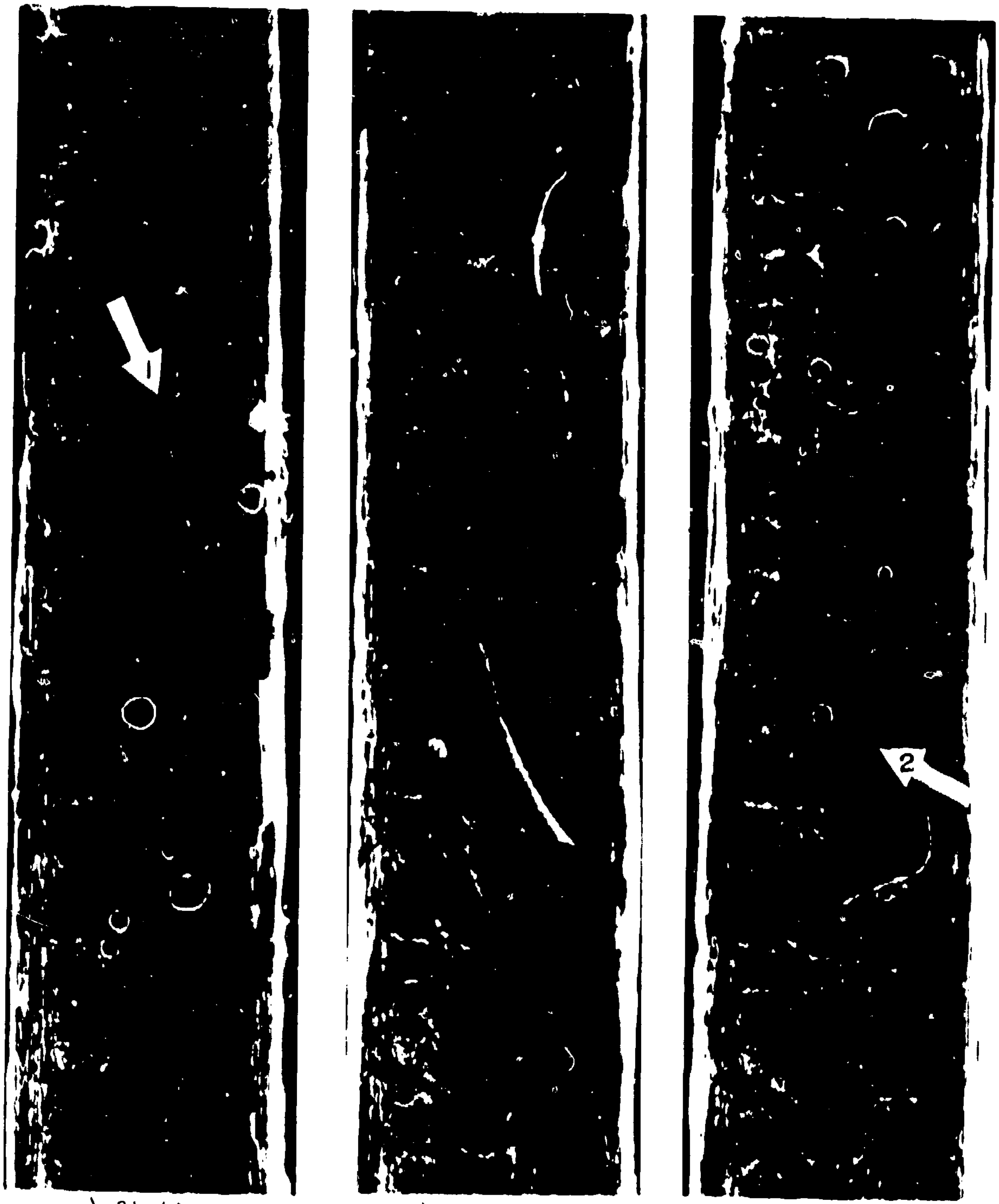

a) Static b) Cycles c) 500 Cycles

Fig. 3-11 Damage along the edge of a type II specimen at 393 MPa after a) static preload, b) 50 cycles, c) 500 cycles

delaminations in the x-y plane and making observations on their growth. Vibrothermography of type II specimens indicated no unusual hot areas. This supports the observations made from the replicas that no delaminations occurred along the free edges.

However, vibrothermography of type I specimens indicated numerous hot areas, all located along areas adjacent to the free edges (Fig. 3.12). These thermographs were made on a 2°C scale. A color band at the bottom of the figure indicates the color sequence in which each color represents a temperature of 0.2°C warmer than the color on its left. The large white areas or hot areas at the bottom of (a), (b), (c), and (f) represent heat from the gripping device of the ultrasonic transducer.

Figure 3.12a is of the 234 MPa specimen taken after 10,000 cycles. By comparing the hot areas between this and (c), the 290 MPa specimen after the same number of cycles, it can be seen that the higher load greatly increases the delaminated area. Thermograph (b) is of the 290 MPa specimen after the static preload but before fatigue. The absence of hot areas in this picture indicates that the fatigue cycling greatly increases the amount of delamination, (c). It was observed from the replicas that the edges contained extensive delaminations after the 290 MPa static preload; however, (b) does not indicate this. The reason for this may be that the delaminations were very shallow, confined very close to the edge, and therefore not detectable. After 10,000 cycles, the replicas indicated that there was a small increase in the total length of the delaminations but probably of more significance is their inward (through the width) growth. This would explain the reason for the discrepency between thermograph (b) and the replicas.

Thermograph (d) illustrates the degree of delamination due to a

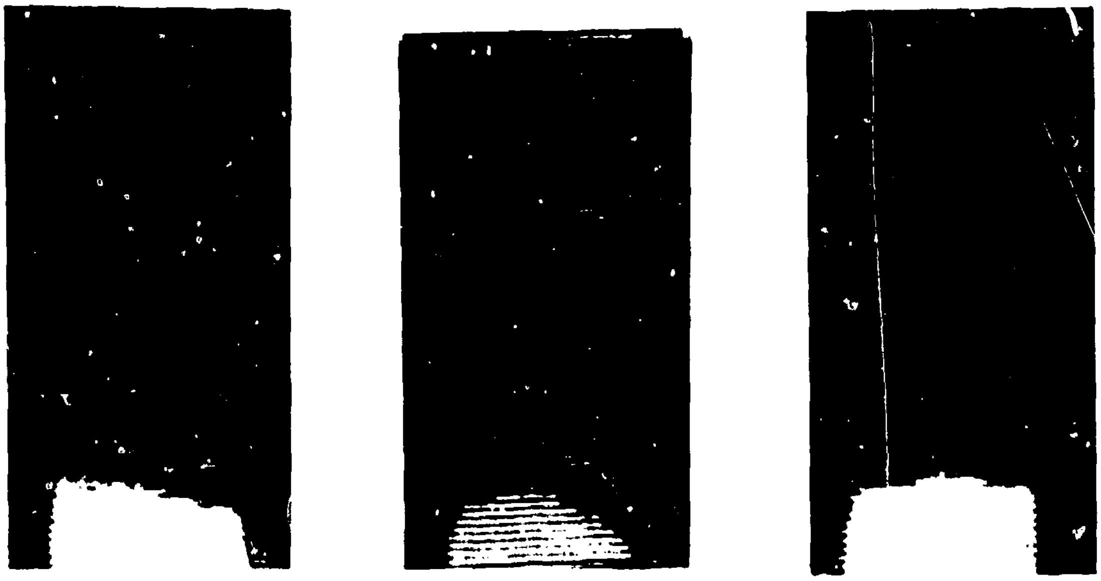

a) 234 MPa, N=10^4 cyc b) 290 MPa, N=1 cyc c) 290 MPa, N=10^4 cyc

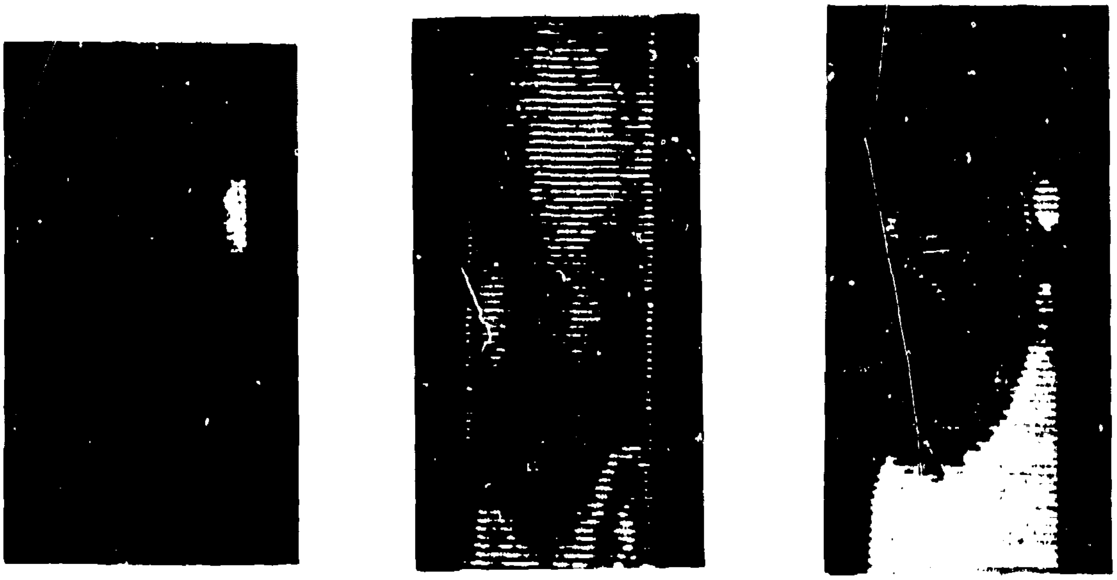

d) 393 MPa, N=1 cyc e) 393 MPa, N=500 cyc f) 393 MPa, N=500 cyc

Fig. 3-12 Vibrothermographs of type I specimens

393 MPa static preload. It shows considerable damage whereas the 290 MPa statically loaded specimen shows no significant damage. To add to the confusion of making comparisons, thermograph (d) has been taken from the opposite side of the specimen from (e) and (f). Therefore, its right side corresponds to the left side of (e) and (f). Thermographs (e) and (f) are both from the 393 MPa specimen after 500 cycles but they are taken at different excitation frequencies. Comparisons between the before and after fatigue cases are not very apparent and it is therefore difficult to make any conclusions concerning the delamination growth from these last three prints.

In summary, this technique clearly distinguishes between type I and type II specimens. Also, it appears to be capable of indicating a relative degree of delamination damage with respect to growth in the x-y plane.

Characteristics of Specimen Failures

A portion of this research was to investigate the fracture area of each specimen, observe any characteristic behavior, and determine if fracture occurred along cracking that had been previously recorded. After the fatigue cycling was completed, each specimen was statically loaded to failure. The fractured edges were replicated and then used to determine the exact location of the fracture from the post-fatigue replicas.

Several similar damage features were observed in both quasi-isotropic laminates. These include transverse cracks in 90° plies, cracks in 45° plies, and local delamination of the ±45° interfaces. Major delaminations were found only in the 90° plies of type I laminates, which have tensile σ_z stresses. However, the extent to which the damage had developed at a point in time was strongly dependent on the stacking sequence and loading history. Figure 3.13 shows the spacing between cracks in the 90° plies of the two laminates for three load histories. The plotted values, from reference 3, represent the average crack spacing measured over the entire three inch test section. At cyclic stress levels of 234 and 290 MPa in type I laminates, the number of cracks increased with cycles until a stable crack spacing of approximately 0.035 in. was reached before 10^4 cycles. At 393 MPa, the same crack spacing was reached by 1/2 cycle and no additional cracks in the 90° plies formed during cyclic loading. At each of the three stress levels, 90° ply delaminations formed only when the cracks in a local region reached the stable spacing. The delaminations lengthened with additional cycles, the cracks spread into the 45° plies, and short delaminations formed along the ±45° interfaces.

A stable spacing of cracks in the 90° plies of type II laminates subjected to maximum cyclic stresses of 290 and 393 MPa was reached before 100 cycles. The stable crack spacing in the type II laminates is smaller than that in type I laminates by a factor of about 2.5. At the 234 MPa stress level, the stable spacing had not been reached by 10^4 cycles, although the spacing steadily decreased during cyclic loading up to that point. Subsequent damage development included cracking of 45° plies and local delaminations along the ±45° interface.

It was observed that both type I and type II specimens fractured according to characteristic patterns. Figure 3.13 contains sketches of these patterns. For both types, the long delaminations occurred along

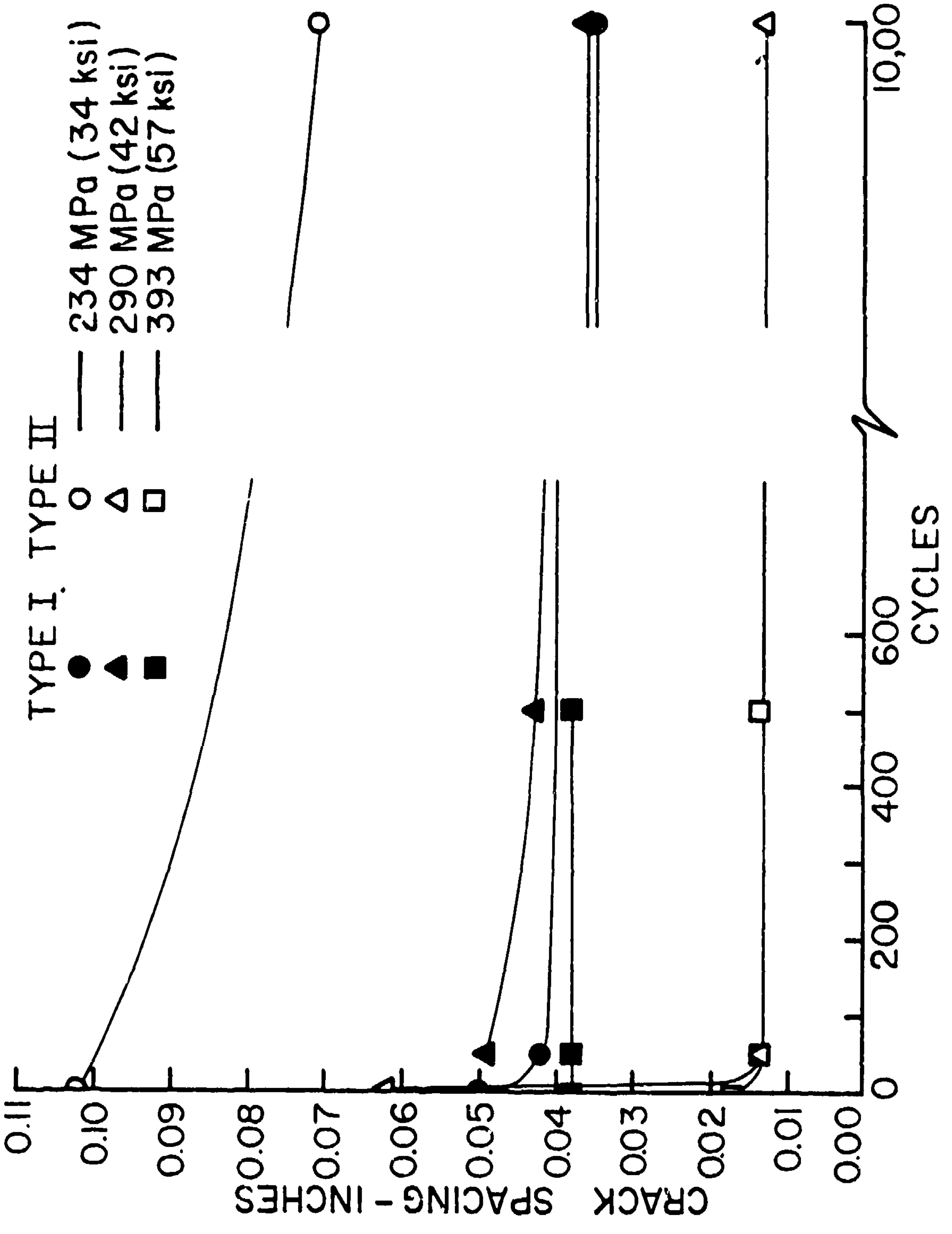

Fig. 3-13 Spacing of transverse cracks in the 90° plies of type I and type II specimens for several load histories

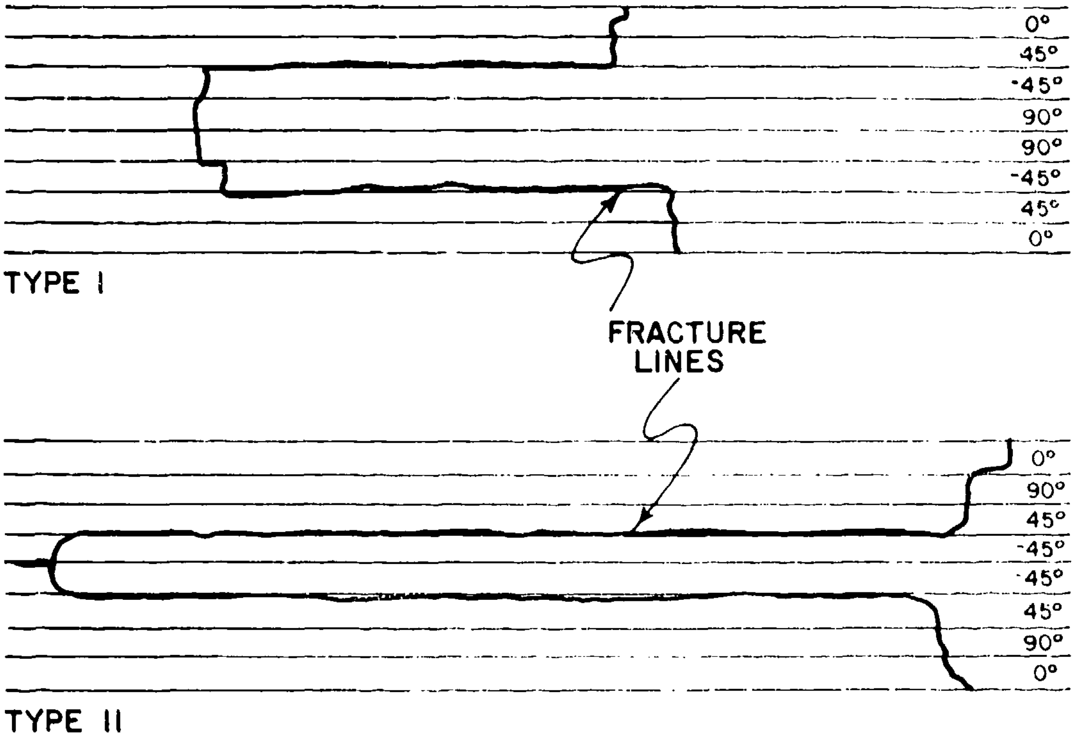
0°
45°
-45°
90°
90°
-45°
45°
0°
TYPE I
FRACTURE LINES
0°
90°
45°
-45°
-45°
45°
90°
0°
TYPE II

Fig. 3-14 Typical edge view fracture patterns for type I and type II specimens

the +45°/-45° interfaces where the τ_{xz} interlaminar shear stresses are large. In addition, for all six specimens, the cracks between the long delaminations and the outside edges were approximately across from each other. The average length of the sections that pulled out or separated for the type II specimens were considerably longer than those of type I. Pulled out sections for the type I materials varied from 0.132 - 0.224 in. in length and from 0.289 - 0.553 in. for type II. Type II specimens contained a central delamination originating from the tip of the pulled out section. This was probably caused by shear stresses acting along the long delaminations as the sections were pulled apart. The same phenomena may have occurred in type I specimens, however, it would not have been observed since the material contained extensive delaminations prior to failure.

Only one specimen, the 290 MPa type I specimen, fractured along previously observed cracks. For this case, a transverse crack and its long branch delaminations (Fig. 3.5b) formed the top of the section that separated. The fracture lines ran along the two +45°/-45° interfaces for 0.224 in. before breaking through the outer layers (arrows 5 and 6, Fig. 3.4c). It can be seen at arrow 5 that a crack already existed through the outer 45° layer prior to failure. No conclusive observations could be drawn from the other five specimens other than that the fracture did follow the characteristic patterns as indicated previously.

Residual strength and elastic modulus data are given in Table III-I. Even though extensive edge damage was present in each case, the residual strength values are still within or above the distribution of static tensile strengths for the two laminates, Fig. 3.15. However, the

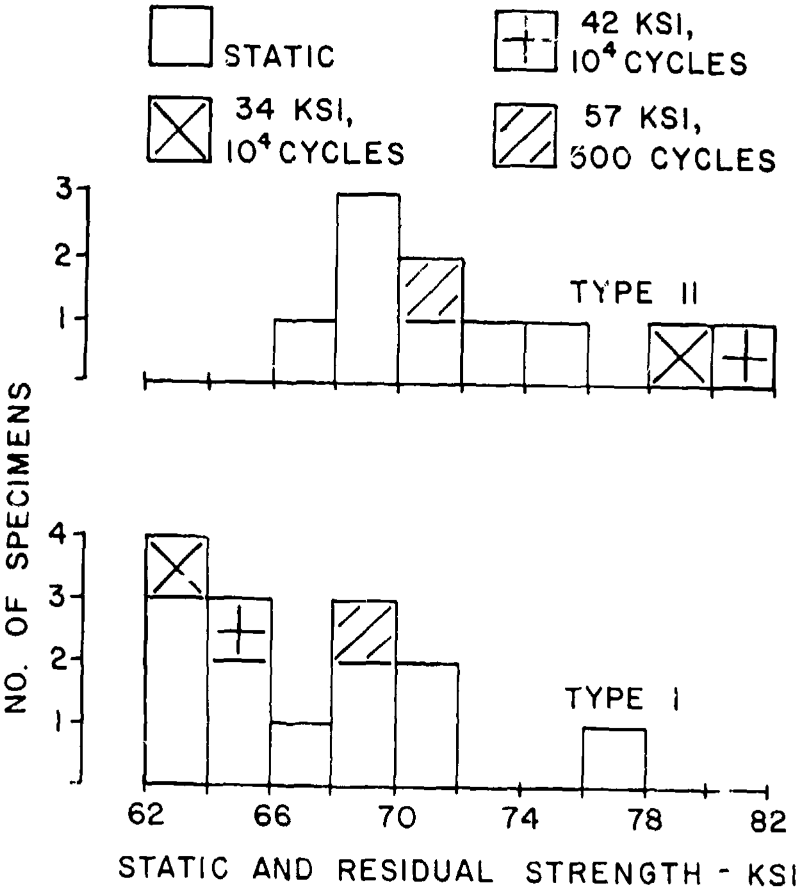

Fig. 3-15 Distribution of static and residual tensile strength values (1 ksi = 6.895 MPa)

TABLE III-I

Residual Strength and Stiffness Data

Type	Max. Cyclic Stress (MPa)	Max. Cyclic Stress (ksi)	Cycles	Residual Strength (MPa)	Residual Strength (ksi)	Percent Change in Stiffness
I	234	34	10^4	434	63.0	- 5.5
I	290	42	10^4	451	65.4	- 8.3
I	393	57	$5x10^2$	470	68.2	- 7.2
II	234	34	10^4	546	79.2	- 7.0
II	290	42	10^4	555	80.5	- 6.1
II	393	57	$5x10^2$	483	70.0	-13.6

elastic modulus decreased in each case indicating that although the damage did not reduce the strength during these relatively short fatigue tests, the stiffness suffered degradation.

SECTION IV

FATIGUE SERIES

A series of tests was performed to determine the nature of damage developed under high cycle fatigue conditions, i.e., after one million cycles of loading. Of particular interest was a comparison of damage developed under static, short term, and long term cyclic loading.

The approach to this objective was to investigate response to one million cycles of loading at three stress levels. A low stress level of 25 ksi (172 MPa) was choosen because it is a common "safe" design stress for this laminate, and it is below the stress level at which lamina cracking ("first ply failure," etc.) would occur if themal residual (cooling) stresses are not considered. A second stress level of 40 ksi (276 MPa) was choosen since it would be an upper bound design level, the stress at which first ply failure would "occur" if thermal residual stresses are neglected. Finally, a stress level of 45 ksi (310 MPa) was choosen because it was only slightly above an accepted limit, thereby providing a useful perspective on the criticality and significance of the 40 ksi level.

Specimens were cyclically loaded in tension (R=0.1) under load control. The tests were interrupted at several intervals for the purpose of making replicas of the edges to obtain a record of the damage development. The dynamic stiffness was recorded continuously by a data acquisition system. Static stiffness was measured at the end of each test as the residual strength of the specimen was determined.

Table IV-I shows a collection of data from these tests along with several details of a two parameter Weibull fit of the residual strength data. The stiffness (actually the longitudinal engineering modulus of elasticity) change during testing reached a maximum of about 10-11 percent in both laminates. However, 25 ksi did cause a stiffness change in the type II material. None was measured for the type I laminate at that level. At 40 ksi the change in stiffness was large in both cases, more in the type I than the type II laminate.

Figures 4-1 and 4-2 show the residual strength data as a function of the cyclic load level. Each symbol represents a single test point. The upper connecting line is drawn through the characteristic strength values (as determined from a Weibull fit) and the lower curve is drawn through the expected values for a reliability of 0.9. Figure 4-1 presents the data for type I laminates, and Fig. 4-2 shows data for type II laminates. Although only a small sample is involved here, it would appear that strength degradation is greater for the type I laminate than for the type II laminate which appears to loose no more strength for the 45 ksi stress level than for the 25 ksi one. In fact, the average static strength of the type II specimens tested earlier was 70.37 ± 2.97 ksi (485 ± 20.5 MPa) which is essentially identical to the residual strength values. The degradation of type I strength with increasing stress level is evident, however, in Fig. 4-1. The average static strength in earlier tests was 67.34 ± 4.19 ksi (464 ± 29 MPa), which is very close to the characteristic strength at the 25 ksi level. However, the residual strength is degraded by about four percent by one million cycles at 40 ksi, and by about fifteen percent by one million cycles at 45 ksi. Perhaps the most striking feature of Figs. 4-1 and 4-2 is the reduction in the spread of strength with increasing stress level. The trend is unmistakable in both cases. The shape factors in Table IV-I bear this out. The specimens appear to become "more similar" as the damage states develop, a point we will address more directly below.

TABLE IV-I

Laminate			Residual Strength		Stiffness Change	
Stress Level	Type	Characteristic Strength (ksi)	Predicted Strength for R=0.9 (ksi)	Shape Factor	Static (%)	Dynamic
25	I	66.51	53.0	9.07	--	--
40	I	63.66	53.0	12.31	9.5	8.37
45	I	57.29	54.3	38.02	10.93	8.3
25	II	68.68	55.5	10.37	2.6	5.0
40	II	70.54	65.0	27.72	8.69	6.47
45	II	69.52	63.0	23.06	10.8	12.16

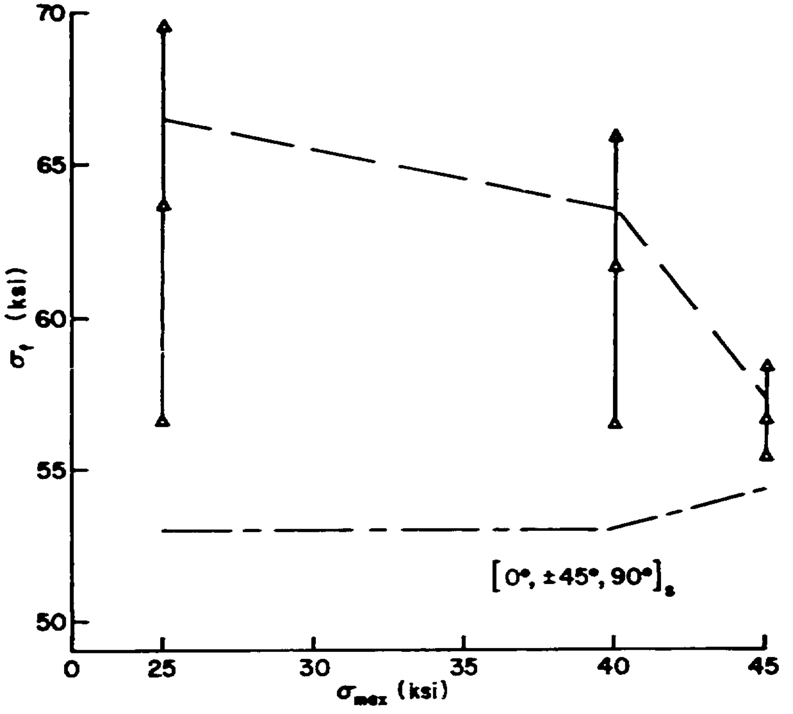

Fig. 4-1 Residual strength of type I specimens after one million cycles at the indicated stress levels

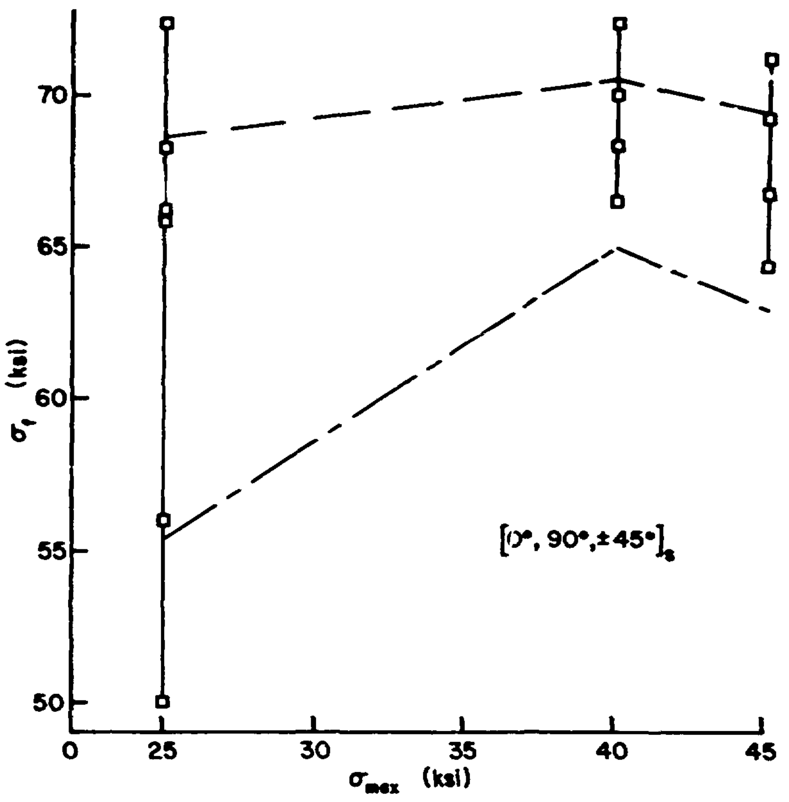

Fig. 4-2 Residual strength of type II specimens after one million cycles at the indicated stress levels

In the following paragraphs we will describe the nature of damage observed at each stress level by edge replication for several different numbers of cycles of loading. Then we will try to generalize our observations and define, as best we can, the damage sequence.

We will first discuss the type I laminate tests. At 25 ksi, a few transverse cracks were observed in the 90° plies before loading. We were unable to establish that these cracks had any affect on subsequent damage development or residual strength. We presently believe that initial cracks have no effect on subsequent service for the loadings considered. After ten thousand cycles of loading, many transverse cracks have formed in the 90° plies, which are on either side of the specimen midplane. These cracks are in a double ply and are, therefore, twice as long as those in other laminae, initially. A few cracks have formed in the -45° plies next to the 90° plies; almost without exception these cracks join, or are extensions of, cracks in the double 90° ply. In most instances some longitudinal cracking has occurred in the 90° layers due to the positive through-the-thickness normal stress. After one hundred thousand cycles of loading at 25 ksi, cracks have begun to couple together, and more cracks have formed in all off-axis layers. The coupling is frequently achieved with the assistance of delamination between the +45 and -45 laminae. By one million cycles most of the off-axis laminae have dense cracking and many cracks are coupled.

At 40 ksi, the type I laminates develop damage early. Even at ten thousand cycles all off-axis laminae are heavily cracked, many cracks have combined, and the 90° plies have developed longitudinal cracking along most of the specimen length. By the time one hundred thousand cycles have been reached, numerous cracks have coupled and a significant number of delaminations have developed between the +45° and -45° layers. Very little new damage forms between one hundred thousand and one million cycles of loading. Delamination at ±45° interfaces and longitudinal cracking in the 90° plies continues to increase, but virtually no new transverse cracks form.

The 45 ksi level causes very serious damage almost immediately. By ten thousand cycles of loading an essentially fixed number of transverse cracks have formed over the entire length of all off-axis laminae. Longitudinal cracking extends over the entire length and delamination between cracks along the ±45° interface is common. The patterns at one hundred thousand and one million cycles are nearly identical to those at ten thousand cycles, except for additional longitudinal cracking and delamination.

The 90° plies in the type II laminate are separated, and the -45° plies form a double ply about the centerline. After ten thousand cycles at 25 ksi there is relatively little damage of any kind. There are usually scattered cracks in the 90° plies, but even they are poorly developed and hard to find. At one hundred thousand cycles, transverse cracks have formed in all layers, with many cracks in the 90° laminae. Some cracks in the -45° pair have jogged along the ±45° interface by delamination and joined transverse cracks in the +45° and 90° plies. Most of the transverse cracks develop between one hundred thousand and one million cycles. While some cracks do couple up as noted earlier, there are relatively few coupled cracks.

At 40 ksi cracks form in the 90° plies in scattered regions by ten thousand cycles of loading. After one hundred thousand cycles at that stress a very regular spacing of cracks has formed in the 90° layers.

Transverse cracks have also formed in all of the other off-axis plies, relatively few in the -45° double ply. About half of the cracks in the + 45° plies are coupled to cracks in the 90° plies. About half of the cracks in the -45° pair have jogged along the ±45° interface and coupled with cracks in the +45° plies. After one million cycles severe transverse cracking has occurred in all off-axis layers. Longitudinal cracking has also occurred in the 90° plies over about one third of the specimen length. About half of all the cracks in a given lamina are coupled to cracks in other laminae, frequently by delamination of ply interfaces.

Cycled loading at 45 ksi produces cracks in all off-axis plies by ten thousand cycles. A regular spacing of cracks has usually formed in the 90° plies over much of the specimen length. Some longitudinal cracking takes place in the 90° plies. After one hundred thousand cycles the transverse crack formation is essentially complete. Some cracks in the -45° pair run along the ±45° interface to join cracks in the +45° and 90° plies. Between one hundred thousand and one million cycles this type of delamination, along ±45° interfaces, increases, as does delamination between the +45° and 90° layers, and longitudinal cracking, all of which become fairly extensive in various regions along the specimen length.

Figure 4-3 shows two typical damage patterns that form at large numbers of cycles at fairly high stress levels. From our observations of patterns such as those (which are typical), and our crack pattern observations, outlined above, we have identified what we believe to be a characteristic damage state. This state consists of the damage condition whereby a more or less regular spacing of cracks has formed in all off-axis plies. (We will discuss the philosophy of this spacing formation

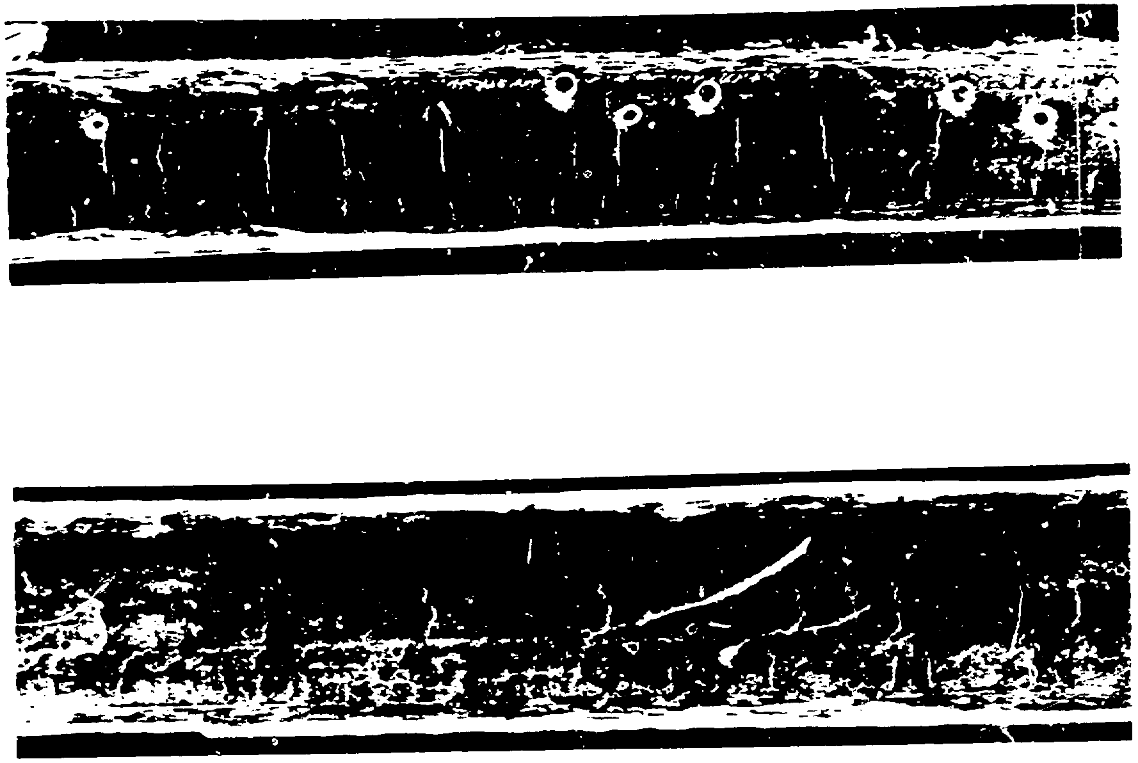

Fig. 4-3 Typical damage patterns in a type I (4-3a) and type II (4-3b) laminate

in the next section.) When this regular crack spacing has formed, the damage state is stable in the sense that virtually no new transverse cracks form until the final fracture. The spacing of the cracks is determined (as we will show) by the constraint of the plies on either side of the cracked ply and by the properties of all the plies, so that it is a characteristic of a given ply in a given laminate. Hence, it is sensitive to stacking sequence and interlaminar stresses. Moreover, in contrast to "first ply failure" it is a clearly defined, precise physical situation which can, therefore, be described and modeled by a well set mechanics analysis. Finally, this characteristic damage state determines the state of stress and the state of strength from which the final fracture develops. Hence, if we can develop an understanding of it and a proper analysis of it we may be able, at least, to construct a rational approach to the mechanics of failure of composite materials, one which is sensitive to all of the parameters known to affect strength, life, and stiffness change. It should also be noted that this characteristic damage state forms under different loading conditions, i.e., it is not load history dependent, but is a characteristic of the laminate alone. The state may form under very high static stress or after many cycles of a lower level of stress, as indicated in Section III. It is the same state each time, however, and only logitudinal cracking, delamination and crack coupling occur thereafter; no further transverse crack formation occurs.

As mentioned earlier, special attention was also paid to the region in which the final fracture event occurs in order to attempt to identify the nature of the final fracture sequence. In some cases some distinctive behavior could be identified. Figure 4-4 shows typical damage patterns in the region of fracture for a type I and type II laminate. The top pattern shows a very common type of pattern in the type I laminate, hereafter called a fork pattern. This pattern is formed by coupling cracks in the double 90° plies with those in the -45° plies by delamination of the 90°-45° interface, and coupling of those cracks with cracks in the +45 layers by rather extensive delamination of the ±45° interface. These fork patterns are nearly always in the region of fracture and in several cases are known to actually be the location of final separation. The lower pattern in Fig. 4-4 shows a typical pattern for the type II laminate. Again, cracks have coupled up by delamination.

Figure 4-5 shows two pre-fracture patterns for the type I and type II laminates. A more complete depictation of the fork pattern in the type I laminate is shown, with typical surrounding damage. The type II pattern is distinctive not only in the manner in which cracks are coupled, but also because of angular cracks that form during the coupling process in the 90° plies. These crack extensions represent crack formation in the presence of the local stress in a damaged laminate, reflected by their peculiar angle. (It should be mentioned that the regular spacing of cracks not involved in the final fracture has been largely omitted in these figures.)

Figure 4-6 shows two sketches of typical fracture patterns in the two laminates. The type I laminate has fractured at the fork pattern assisted by extensive delamination at the edge where the replicas were made. The delamination and crack coupling allows a through-crack to form through all of the off-axis plies prior to fracture. Extensive delamination of both the ±45° and the 45°/90° interfaces is involved in the final fracture of type I and type II laminates.

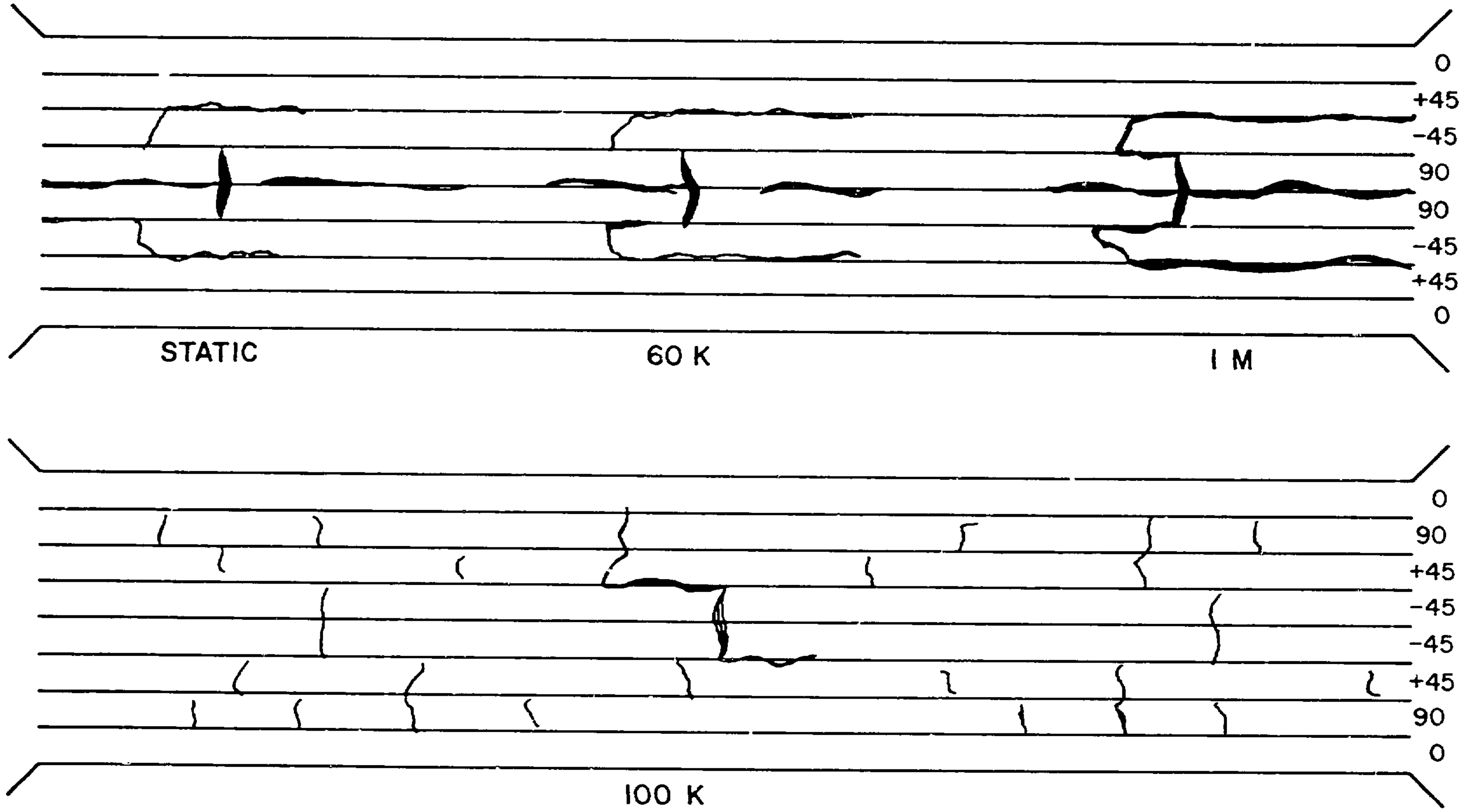

0
+45
-45
90
90
-45
+45
0
STATIC
60 K
I M
0
90
+45
-45
-45
+45
90
0
100 K

Fig. 4-4 Damage patterns in the region of fracture for a type I and type II laminate, at moderate cyclic stress levels

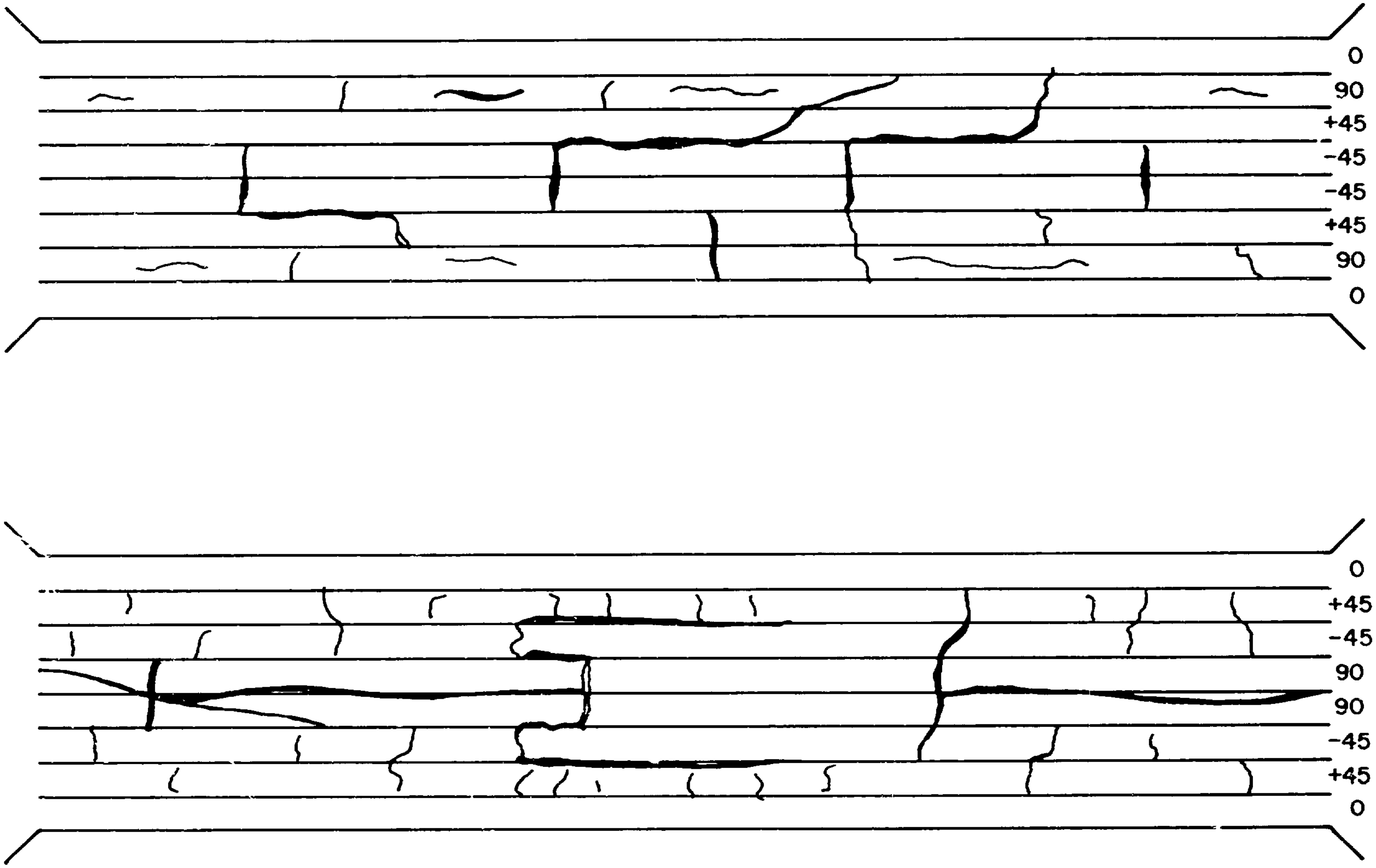
0
90
+45
-45
-45
+45
90
0
0
+45
-45
90
90
-45
+45
0

PRE-FRACTURE PATTERNS NEAR FRACTURE SITE

Fig. 4-5 Pre-fracture patterns near the fracture site in a type I and type II laminate

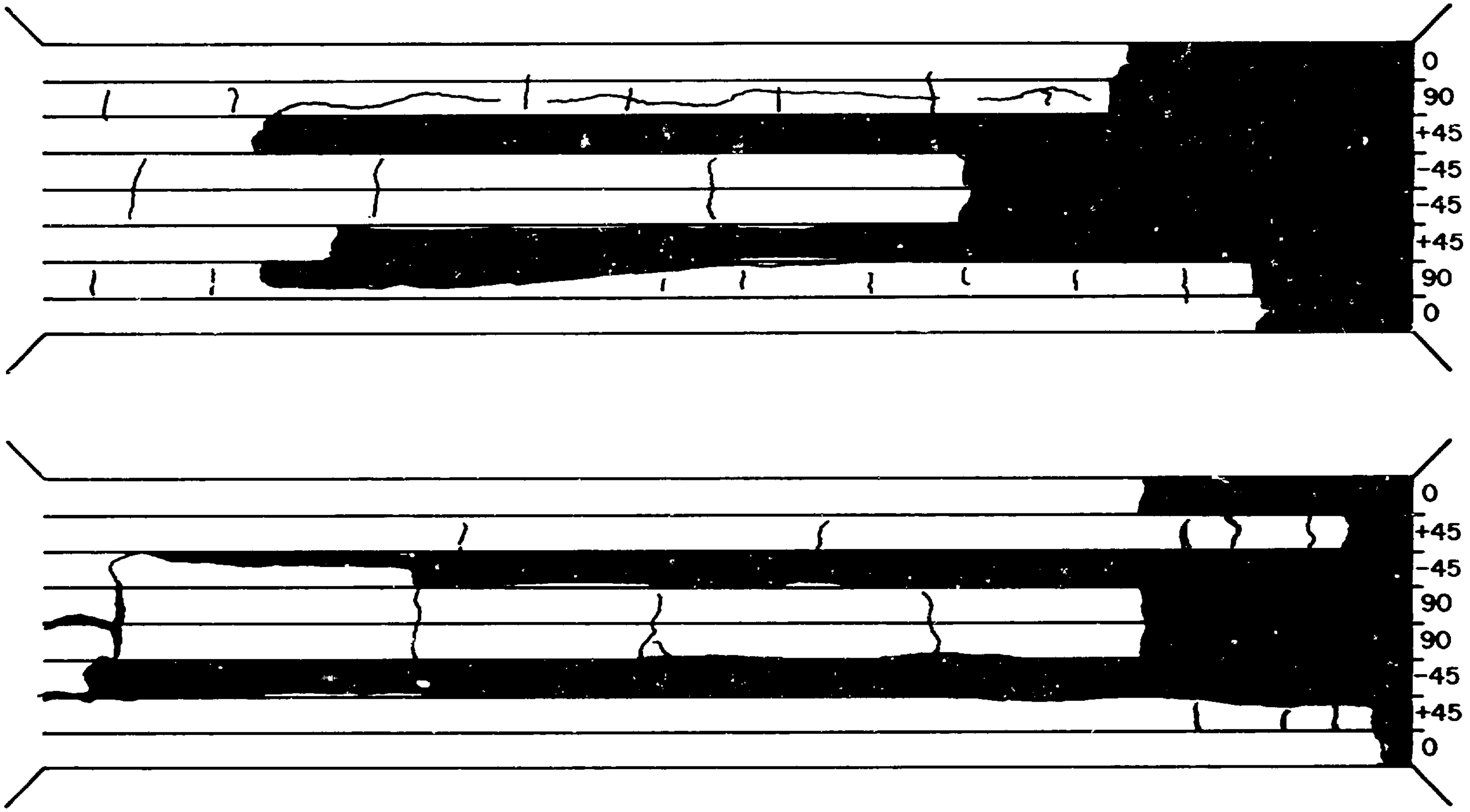
0
90
+45
-45
-45
+45
90
0
0
+45
-45
90
90
-45
+45
0

FRACTURE PATTERNS

Fig. 4-6 Typical fracture patterns for type I and type II laminates

Based on our observations the following final fracture sequence is suggested:

1. Transverse cracks form in off-angle plies. The types of cracks (the plies which crack) are controlled by the static or cyclic stress level. The degree of cracking (the number of cracks formed) is influenced by the service life or number of cycles of loading.
2. Cracks couple together. Transverse cracks in one lamina spread into the neighboring laminae. Transverse cracks couple with other (near-by) cracks in other laminae by interface debonding enhanced by tensile σ_{zz} stresses caused by transverse cracks which stop at those interfaces. Longitudinal cracking, caused by stacking-sequence-related σ_{zz} stresses, may also assist in crack coupling.
3. An intense damage region forms by the above processes.
4. A crack forms through all of the off-axis plies by jogging and crack coupling as described earlier.
5. Fracture of the 0° plies causes specimen rupture. The final fracture is influenced by the local stress elevation and constraint in the damage region which is a function of the stacking sequence and internal crack pattern.

In general, the pre-fracture characteristics of the "intense damage region" include high connectivity of cracks in all off-axis layers, a high density of transverse cracks, significant delamination and longitudinal cracking, and the most prominent and well developed transverse cracks in the specimen.

We add the following general observations based on this test series.

1. Cyclic loading increases the density of transverse cracks at a given stress level.
2. A stable crack density eventually forms creating a characteristic damage state for a given laminate which exists until final fracture. This state is a well defined physical situation.
3. Cyclic loading increases the amount of longitudinal cracking and interface delamination compared to static loading to a comparable stress level.
4. Regions of high crack connectivity and high crack density develop at large numbers of cycles of high or moderately high stress application. One of these regions is generally the final fracture site.
5. Cyclic loading may significantly change the stiffness and residual strength of the laminates tested. It also changes the nature of the residual strength distribution compared to the static strength distribution.

SECTION V

ANALYSIS OF DAMAGE STATES

In the absence of stress raisers, and in many cases when they are present, damage in composite materials produced by quasi-static or fatigue loading consists of an intricate orchestration of failure events which involves individual plies and, in some cases, individual fibers. There is growing evidence that the engineering fatigue and fracture response of these laminates can be successfully described by considering ply-level events such as the formation of cracks transverse to the load axis through the thickness of a given ply, and their subsequent growth [2-6].

The motivation for developing an analytical model or representation of such damage states is much the same as the motivation for using linear elastic fracture mechanics to describe the characteristic damage state (a single crack) in homogeneous, uniform materials. However, there is an additional motivation for composite materials, beyond the desire to quantitatively represent the damage condition and predict the seriousness of a given damage state, expected or observed. We have not, unfortunately, established the precise nature of a characteristic damage state in composite materials (although the present research has been a strong step in that direction). Hence, an analysis which describes and relates certain observations, and predicts things that we cannot or have not observed can be a very important assistance in our learning process.

Two approaches to the analysis of damage states will be outlined below. Both deal with transverse cracks which extend through the thickness of a given ply. The first such analysis is a strength-of-materials approach which is simple, versatile and useful, but has very limited accuracy. The second approach is a finite difference approach to the solution of the stress distribution problem for a laminate with various cracked ply arrangements. The latter provides three-dimensional stress information with improved accuracy.

1. Equilibrium Element Analysis

We imagine a schematic represenation of the situation shown in Fig. 1 wherein two 90° plies are cracked, but no further damage propagation has occurred. (See Fig. 2.) We assume that the constraint layers next to the crack have an orientation of σ degrees to the load axis. We further assume that the disturbance caused by the broken layer does not extend beyond the first constraining (unbroken) ply on either side of the broken ply. Finally, on the basis of experimental observations we estimate that any gradients in response from ply to ply occur over a distance, b, which extends for a distance of one twentieth of the ply width into each ply, or about the thickness of one tow or bundle on either side of the ply interface in the case of graphite epoxy for example.

To consumate the analysis, we envoke an equilibrium element approach, a method which is as old as the discipline of mechanics, and which has been applied to other problems in composite materials by other investigators [7-9]. Referring to Fig. 2, we consider the equilibrium of an element dx long, two ply thicknesses wide, and of unit thickness representing the region immediately above or below a crack in two 90° plies as seen in Fig. 1. A simple force balance can then be written including only stress components throught to be important, two shear stress components on either side of the element representing the action of the constraint layers and an axial normal stress component within the element in this case. The resulting equation is

$$aE_{x_{90}} \frac{d^2U_{90}}{dx^2} + 2G\left(\frac{U_{45}-U_{90}}{b}\right) = 0 \qquad (5\text{-}1)$$

where $E_{x_{90}}$ is the uniaxial engineering stiffness of the 90° ply in the x direction, G is the engineering shear stiffness of the matrix material, U_{90} is the average X displacement of the 90° ply at a given point, and the stress transfer region dimension b has been used to write the constraining forces in difference form. For the constraint layers, an equilibrium element can also be constructed having width c and axial displacement U_2 as shown in Fig. 5-2. The resulting equilibrium equation is

$$cE_{x\alpha} \frac{d^2U_\alpha}{dx^2} + \frac{G}{b}\left(U_{90} + U^\circ - 2U_\alpha\right) = 0 \qquad (5\text{-}2)$$

where $E_{x\alpha}$ is the uniaxial engineering stiffness of the constraint layer, U° is the unidisturbed laminate displacement and U_α is the average displacement in the constraint layer. We choose to normalize these equations by the definitions

$$U = \sigma_a\left(\frac{1}{E_xG}\right)^{1/2} au \qquad\qquad X = \left(\frac{E_x}{G}\right)^{1/2} ax \qquad (5\text{-}3)$$

where E_x is the laminate uniaxial stiffness and σ_a is the laminate applied stress. Equations (1) and (2) then take the form

$$A \frac{d^2u_{90}}{dx^2} + u_\alpha - u_{90} = 0 \quad \text{and} \quad B \frac{d^2u_\alpha}{dx^2} + u_{90} + x - 2u_\alpha = 0 \qquad (5\text{-}4)$$

where

$$A = \frac{b}{2a} \qquad \text{and} \qquad B = \frac{bc}{a^2}$$

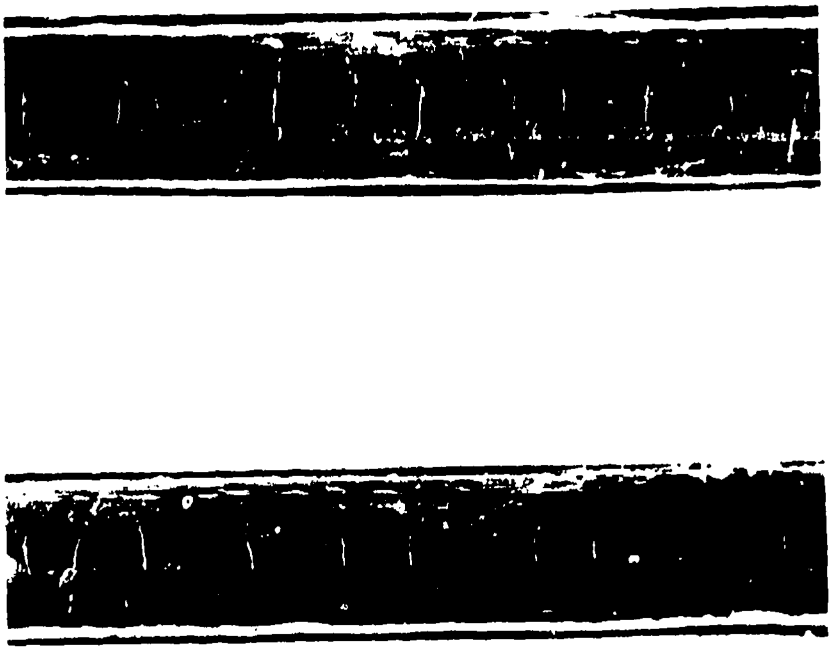

Fig. 5-1 Transverse cracks in a $[0,\pm45,90]_s$ laminate

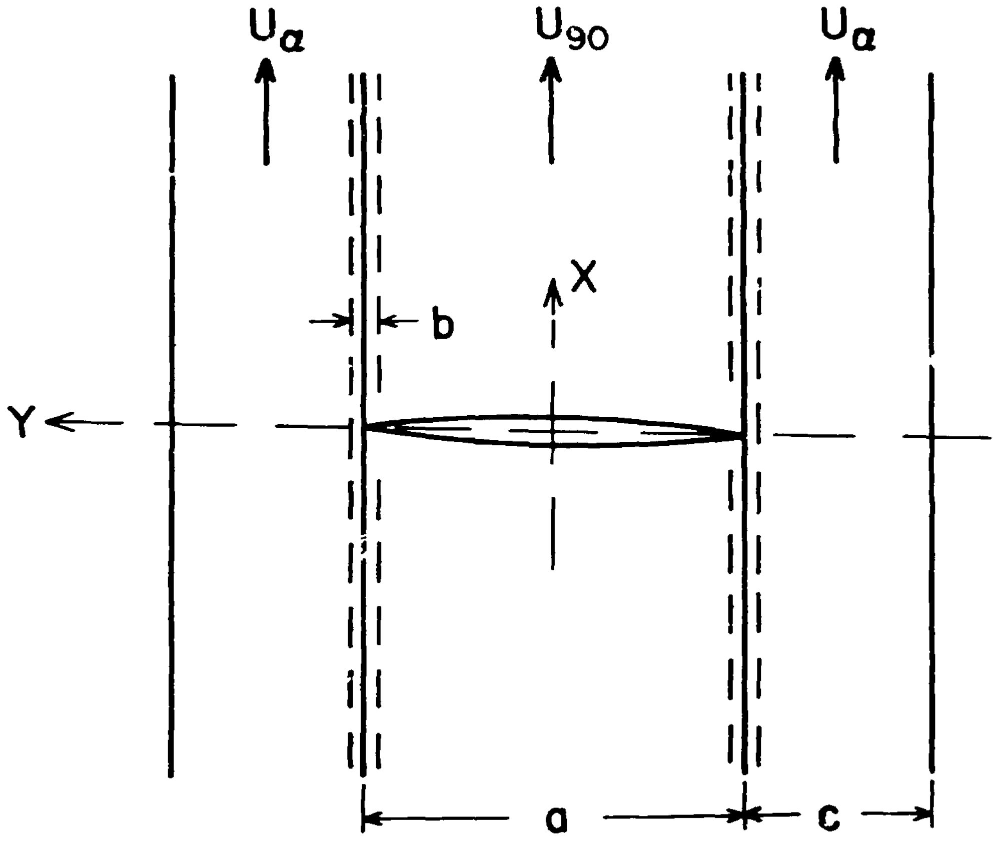
U_α
U_{90}
U_α
X
b
Y
a
c

Fig. 5-2 Schematic diagram of a cracked laminate (edge view)

for this case. The boundary conditions require that the disturbance die out at large distances from the crack and that all stresses with normal components vanish at the crack face. We also require that displacement components vanish along the Y axis in all unbroken plies. The analytical statement of those conditions follows.

$$\frac{du_{90}}{dx}(x \to \infty) = 1 \qquad \frac{du_{\alpha}}{dx}(x \to \infty) = 1 \tag{5-5}$$

$$\frac{du_{90}}{dx}(x = 0) = 0 \qquad u_{\alpha}(x = 0) = 0 \tag{5-6}$$

Solutions to equations (4), as well as a large class of similar equations are easily obtained and are available from such familiar situations as the coupled oscillator problem. For our purpose we choose solutions of the form

$$\begin{aligned} u_{90} &= x + C_1 e^{-\alpha x} + C_2 e^{-\beta x} \\ u_{\alpha} &= x + D_1 C_1 e^{-\alpha x} + D_2 C_2 e^{-\beta x} \end{aligned} \tag{5-7}$$

as found in reference [2]. These are solutions if the auxiliary conditions

$$\begin{aligned} D_1 &= 1 - A\alpha^2 \\ D_2 &= 1 - A\beta^2 \end{aligned} \qquad \alpha,\beta = \frac{B+2A}{2AB} \pm \frac{1}{2AB}[B^2+4A^2]^{1/2}\ ^{1/2} \tag{5-8}$$

are satisfied. Boundary conditions (6) also require that

$$C_1 = \frac{-D_2}{\beta D_1 - \alpha D_2} \qquad C_2 = \frac{D_1}{\beta D_1 - \alpha D_2} \tag{5-9}$$

It can be seen that boundary conditions (5) are automatically satisfied by equations (7). The system of equations (7-9) then provide the complete solution to the problem.

While the above formulation will be used to provide data for the present paper, and the details of the formulation are basic to the approach, a myraid of related variations are easily achieved to handle various special cases including flaw propagation and plasticity [7-9]. We will also apply it to a situation wherein the cracked ply is an exterior surface ply, requiring considerable changes in the equations themselves but no change in the philosophy or approach. Space does not permit a discussion of these details here.

Our objective is to demonstrate the nature of the problem of damage which extends only partly through the thickness of a laminate to the extent possible using a very simple equilibrium element approach. We begin by addressing the analysis to an eight ply laminate having stacking sequence $[0,\pm45,90]_s$ made from AS-3501 graphite epoxy material. Figure 5-1 shows an example of a typical physical situation which develops during loading of this type of laminate. Static loading to about two-thirds of the ultimate strength or cyclic (fatigue) loading at lower levels of the order of half the ultimate strength typically produces cracks which extend through the two 90° plies on either side of the center plane. Moreover, these cracks increase their density as static loading or the number of cycles of fatigue loading increases until a stable number are formed. This situation produces a more or less regular spacing of cracks as shown in Fig. 5-1. The spacing distance is characteristic of the laminate, and is affected by the constraint afforded by the stacking sequence, the material strength and the laminate elastic properties. Some additional details of the physical situation appear in references [-6], and elsewhere in this report.

Since the saturation spacing distance of part-through cracks is an obvious feature which is easily measured, it is a convenient quantity to test the accuracy and sensitivity of the analysis. To do so, we postulate that the cracks are spaced apart by the distance required for the stress in the broken layer to return to the value in the unbroken part of the layer away from the crack. The postulate is based on the idea that at the saturation spacing load level, there will be a crack each place the stress reaches the uncracked level in the ply being considered, so as one moves away from a crack surface the constraining adjacent plies transfer stress back into the cracked ply until at a distance equal to the saturation spacing the stress just reaches the undisturbed value which is sufficient to form another crack at that point. The implication is that the stress has reached a level which is sufficient to crack all material elements in the given ply or plies, but each time a crack forms it relaxes the (axial) stress for a characteristic distance on either side of the crack producing the equilibrium spacing observed.

To calculate this spacing we need only solve for the stress in the 90° plies, in the present case, and determine the distance required for our normalized stress to reach the value of approximately 1. For the material in Fig. 5-1 we use $a = 0.30$ mm, $b = 0.015$ mm, $c = 0.15$ mm, $E_{x_{90}} = 9.17$ GPA, $E_{x_0} = 142.7$ GPA in the analysis. A plot of normalized stress verses normalized distance from the crack face is shown in Fig. 5-3 for this case. In order to establish a value of x at which the stress reaches the undisturbed value one must either pick a discretionary value off of the plot or return to the equations and set a specific value of the normalized stress. In the interest of precision, the latter was done for the data below; a value of 0.999 was used as the normalized

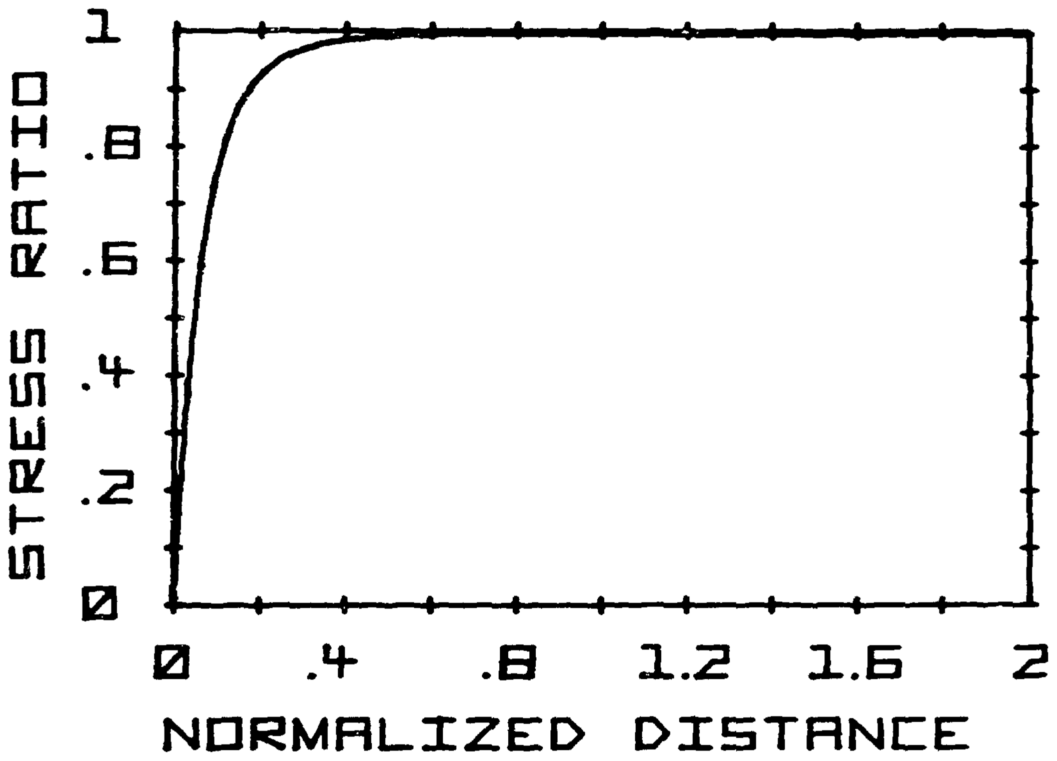

Fig. 5-3 Normalized stress in cracked ply above the crack face

value of stress at which a new crack would form. (Since the function is asymptotic it was reasoned that the material would not wait for the miniscule difference between, say, 0.999 and 1 before breaking. However, the choice is not of great consequence.)

The results of this calculation, and others, are shown in Table V-I, along with the spacing values measured experimentally. The experimentally determined values are expressed as the range of values included within one standard deviation above and below the average measured value. Both static and fatigue data are shown for the first entry in Table V-I which corresponds to the calculation described. It can be seen that the predicted value of 0.76 mm falls well within the range of experimental values for both cases. However, this regular spacing of cracks is observed in other situations. If the simple model postulated above is valid, it should describe those situations as well.

If the stacking sequence of the laminate is changed to $[0,90,\pm45]_s$ regular spacings of cracks form in the single 90° plies and in the pair of 45° plies in the center at stress levels of about two-thirds of the ultimate strength. At higher levels, as the failure strength is approached, cracks from adjacent layers combine with the regularly spaced cracks and spread into the layer destroying the conditions described by the model. Equations (1) and (2) can be used to describe the cracks in the 45° layers by adjusting constants, setting alpha equal to 45°, and changing U_{90} to U_{45}. The results of that calculation are listed as the second entry in Table V-I. The prediction again falls within the range of experimental values, but it appears to be on the high side of the average, possibly because shear stresses have been ignored but are known to occur in the 45° layers. To predict the crack spacing in the 90°

TABLE V-I

Specimen Type	Predicted Crack Spacing (mm)	Observed Crack Spacing (mm)
Cracks in center two 90° plies of $[0,\pm45,90]_s$ laminate	0.76 0.76	Static 1.51 - 0.62 Fatigue 1.44 - 0.47
Cracks in two center 45° plies of $[0,90,\pm45]_s$ laminate	1.21	1.25 - 0.995
Cracks in single 90° plies of $[0,90,\pm45]_s$ laminate	0.363	0.423 - 0.241
Cracks in two center 90° plies of $[0,90]_s$ laminate	0.882	1.087 - 0.532
Cracks in outside 90° plies of $[90,0]_s$ laminate	1.66	1.73 - 0.775
Cracks in the single 45° plies of $[0,90,\pm45]_s$ laminate	0.875	1.40 - 0.350

layers, one must solve a system of three equations of the form

$$A \frac{d^2 u_{90}}{dx^2} + u_{45} + u_0 - 2u_{90} = 0 \qquad (5\text{-}10)$$

$$B \frac{d^2 u_{90}}{dx^2} + u_{90} + x - 2u_{45} = 0 \qquad (5\text{-}11)$$

$$C \frac{d^2 u_0}{dx^2} + u_{90} - u_0 = 0 \qquad (5\text{-}12)$$

With a corresponding set of auxiliary equations. The third entry in Table V-I compares the results from the solution of equations (10) - (12) with experimental data. The agreement is good - extremely close to the average measured value. A completely different case was also analyzed, a four ply graphite epoxy laminate having stacking sequences of $[0,90]_s$ and $[90,0]_s$. The second of these two situations involved a 90° ply bounded by a free surface and an interior 0° ply, requiring another restatement of the problem and new solutions. The preditions and observations are the fourth and fifth entries in Table V-I. The agreement is seen to be quite good. Moreover, the effect of constraint is highlighted by this situation, as evidenced by the nearly doubling of the crack spacing.

The last entry in Table V-I shows the calculated and measured crack spacings for the first 45° ply under the outside 0° ply in a $[0,90,\pm45]_s$ laminate. Again, the agreement is excellent.

Based on the apparent ability of the analytical model to represent the effect of constraining layers on flaw development over a wide range of situations including different laminates, different stacking sequences, and different materials, it is reasonable to attempt to use the model to predict other effects. The axial stress in the constraining plies can also be determined from the analysis as, described above. Hence, the stress increase in those plies can be calculated. The maximum value of that increased stress will be a function of the orientation of the constraining ply. A plot of the increased stress adjacent to a crack in two 90° plies for the AS-3501 properties listed earlier, normalized by the applied stress on the laminate is shown in Fig. 5-4. The laminate engineering stiffness in the loading direction was held constant. The plot represents an average stress concentration across the thickness of the constraining ply (since the displacement is taken to be uniform across each ply thickness in the model) as a function of constraint ply orientation.

The information in Fig. 5-4 can be used to estimate the relative tendency for the crack to spread across the constraining layer by incorporating the data into a failure criterion applied in the constraint layer. For simplicity, and with some motivation from past experience, a polynomial form of the maximum strain criterion having the form

$$\frac{\varepsilon_1}{\varepsilon_1} + \frac{\varepsilon_2}{\varepsilon_2} + \frac{\gamma}{\varepsilon_s} - \frac{\gamma\varepsilon_1}{\varepsilon_1\varepsilon_s} - \frac{\gamma\varepsilon_2}{\varepsilon_2\varepsilon_s} - \frac{\varepsilon_1\varepsilon_2}{\varepsilon_1\varepsilon_2} - \frac{\gamma\varepsilon_1\varepsilon_2}{\varepsilon_1\varepsilon_2\varepsilon_s} = FF \qquad (5\text{-}13)$$

where ε_1, ε_2, γ are the strains in the fiber system and ε_1, ε_2, ε_s are the corresponding maximum values, was used to produce the data shown in Fig. 5-5. The nonlinearity of the plot is of special interest. It suggests, for example, that while a crack is more likely to spread into an adjacent 90° ply than any other orientation, it is only eleven percent less likely to spread into a 45° ply, i.e., 45° plies are relatively poor crack stoppers. We have experimental evidence in support of this

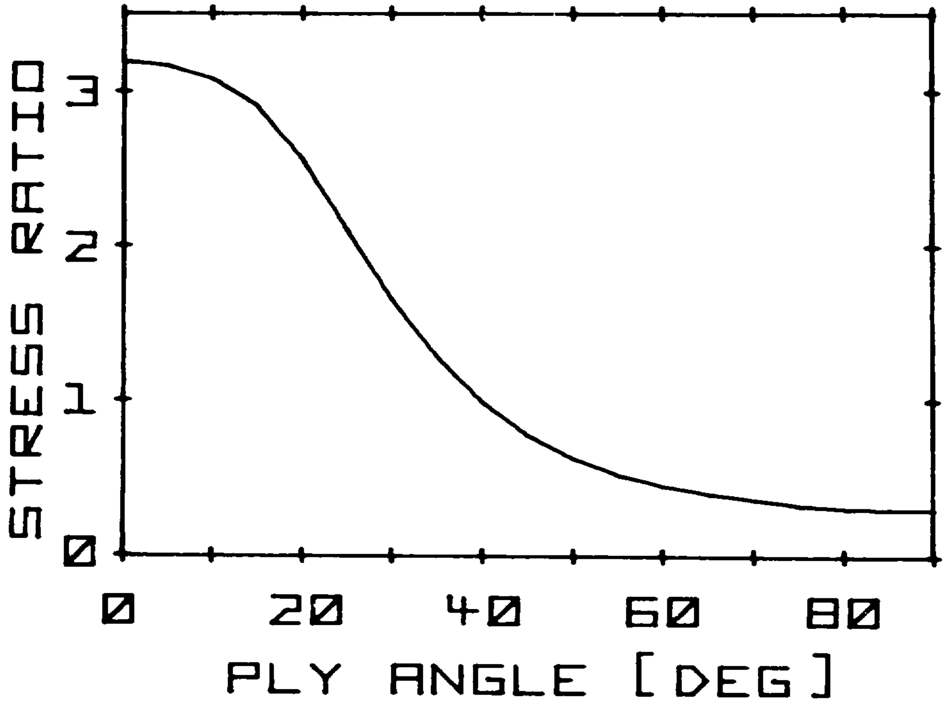

Fig. 5-4 Stress concentration in the constraint ply

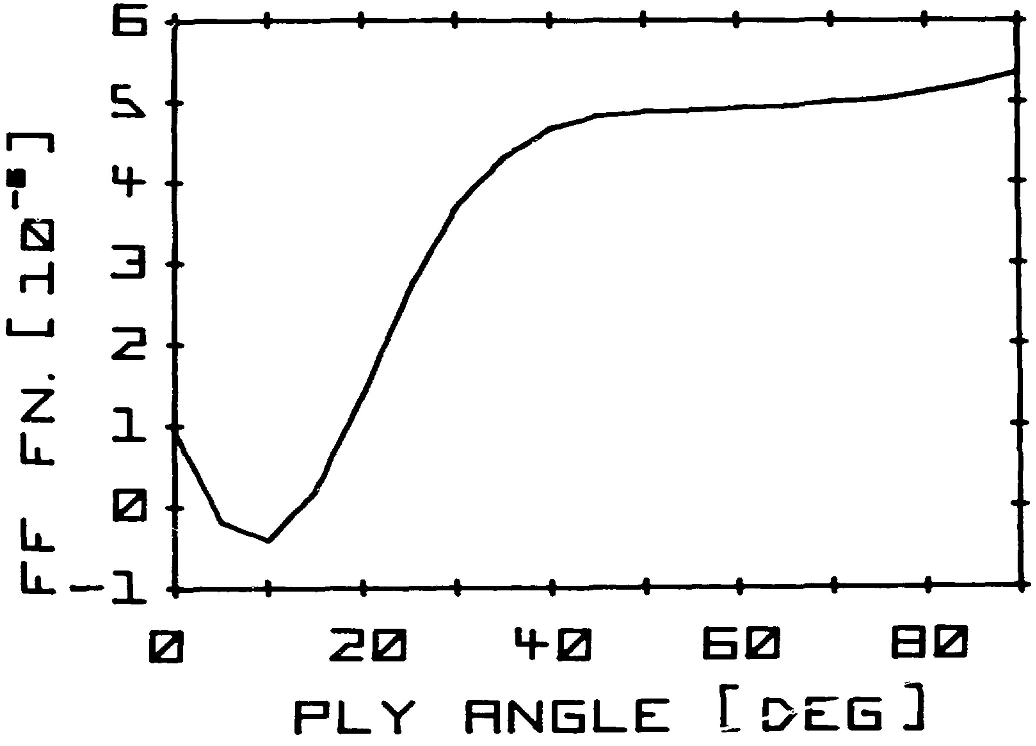

Fig. 5-5 Normalized failure function in the constraint ply

prediction. (The negative values in Fig. 5-5 are a departure from reality caused by the small normalized numerical values and other minor discrepancies.)

This analytical model, which uses an equilibrium element approach in the present case, is sensitive to lamina and laminate elastic properties, flaw size, stacking sequence and an interlaminar stress transfer distance b which is estimated from experimental observations. (A value of $b = 0.015$ mm was used for all calculations above.) The analysis is easily extended to handle flaw growth and plastic region formation. By varying other parameters in the model one can anticipate various other responses. Perhaps the most important aspect of this simple approach is its ability to predict a characteristic state of damage consisting of regularly spaced cracks, fixed in number, having a specific, well defined internal state of stress. This may be an important step in the direction of establishing an analytical philosophy for damage in composite laminates.

This one-dimensional treatment is not able to answer questions regarding the details of the complex three-dimensional stress field in the vicinity of an internal crack, however. In order to address such questions, and the issues that depend on them (such as the likelyhood that a crack will extend or spread along a boundary), a finite difference solution of the three-dimensional problem was attempted. The formulation of that theory and some early results follow in the next section.

2. Finite Difference Formulation

The analytical formulation of the problem is based on the classical elasticity approach where the governing equations are chosen to be the equilibrium conditions:

$$\frac{\partial \sigma_x}{\partial x} + \frac{\partial \tau_{xy}}{\partial y} + \frac{\partial \tau_{xz}}{\partial z} = 0$$

$$\frac{\partial \tau_{xy}}{\partial x} + \frac{\partial \sigma_y}{\partial y} + \frac{\partial \tau_{yz}}{\partial z} = 0$$

$$\frac{\partial \tau_{xz}}{\partial x} + \frac{\partial \tau_{yz}}{\partial y} + \frac{\partial \sigma_z}{\partial z} = 0$$

To obtain an "interior" solution for regions remote from the edges of the finite plate, it is assumed that the plate is infinitely wide. In view of this it can be assumed that the six independent components of the stress tensor are functions of x and z alone. Hence the governing equations reduce to

$$\frac{\partial \sigma_x}{\partial x} + \frac{\partial \tau_{xz}}{\partial z} = 0$$

$$\frac{\partial \tau_{xy}}{\partial x} + \frac{\partial \tau_{yz}}{\partial z} = 0$$

$$\frac{\partial \tau_{xz}}{\partial x} + \frac{\partial \sigma_z}{\partial z} = 0$$

The constitutive relations for the material system under consideration can be written in terms of the compliance matrix S as

$$\begin{Bmatrix} \epsilon_x \\ \epsilon_y \\ \epsilon_z \\ \gamma_{yz} \\ \gamma_{xz} \\ \gamma_{xy} \end{Bmatrix} = \begin{pmatrix} S_{11} & S_{12} & S_{13} & 0 & 0 & S_{16} \\ S_{12} & S_{22} & S_{23} & 0 & 0 & S_{26} \\ S_{13} & S_{23} & S_{33} & 0 & 0 & S_{36} \\ 0 & 0 & 0 & S_{44} & S_{45} & 0 \\ 0 & 0 & 0 & S_{45} & S_{55} & 0 \\ S_{16} & S_{26} & S_{36} & 0 & 0 & S_{66} \end{pmatrix} \begin{Bmatrix} \sigma_x \\ \sigma_y \\ \sigma_z \\ \tau_{yz} \\ \tau_{xz} \\ \tau_{xy} \end{Bmatrix}$$

Substituting the strain-displacement relations

$$\varepsilon_x = \frac{\partial u}{\partial x}, \quad \varepsilon_y = \frac{\partial v}{\partial y}, \quad \varepsilon_z = \frac{\partial w}{\partial z}$$

$$\gamma_{yz} = \frac{\partial v}{\partial z} + \frac{\partial w}{\partial y}, \quad \gamma_{xz} = \frac{\partial u}{\partial z} + \frac{\partial w}{\partial x}, \quad \gamma_{xy} = \frac{\partial u}{\partial y} + \frac{\partial v}{\partial x}$$

into the LHS of the constitutive relations and integrating the first three equations with respect to x, y and z respectively, one has:

$$u(x,y,z) = (S_{11}\sigma_x + S_{12}\sigma_y + S_{13}\sigma_z + S_{16}\tau_{xy})dx + f_1(y,z)$$

$$v(x,y,z) = (S_{12}\sigma_x + S_{22}\sigma_y + S_{23}\sigma_z + S_{26}\tau_{xy})dy + f_2(x,z)$$

$$w(x,y,z) = (S_{13}\sigma_x + S_{23}\sigma_y + S_{33}\sigma_z + S_{36}\tau_{xy})dz + f_3(x,y)$$

Substituting these expressions for u, v and w through the strain-displacement relations into the LHS of the last three constitutive relations and noting that the RHS of these equations are independent of y, one can (after a considerable amount of algebraic manipulation) integrate to obtain the functional forms of u, v and w as:

$$u(x,y,z) = (C_1 + C_2 z)y - C_3 y^2 + U(x,z)$$

$$v(x,y,z) = (C_4 + 2C_3 x + 2C_5 z)y - (C_1 + C_2 z)x + V(x,z)$$

$$w(x,y,z) = -C_2 xy + C_6 y - C_5 y^2 + C_7 + W(x,z)\ .$$

Considering the symmetry conditions:

with respect to the x-y plane

$$u(x,y,z) = u(x,y,-z) \Rightarrow C_2 = 0$$

$$v(x,y,z) = v(x,y,-z) \Rightarrow C_5 = 0$$

$$w(x,y,z) = -w(x,y,-z) \Rightarrow C_6 = C_7 = 0$$

with respect to the y-z plane:

$$u(x,y,z) = -u(-x,y,z) \Rightarrow \text{(trivial)}$$

$$v(x,y,z) = v(-x,y,z) \Rightarrow C_1 = C_3 = 0$$

$$w(x,y,z) = w(-x,y,z) \Rightarrow \text{(trivial)}$$

Therefore the displacements are given by:

$$u(x,y,z) = U(x,z)$$

$$v(x,y,z) = C_4 y + V(x,z)$$

$$w(x,y,z) = W(x,z)$$

Then the strains become:

$$\varepsilon_x = \frac{\partial U}{\partial x}, \quad \varepsilon_y = C_4, \quad \varepsilon_z = \frac{\partial W}{\partial z}$$

$$\gamma_{yz} = \frac{\partial V}{\partial z}, \quad \gamma_{xz} = \frac{\partial U}{\partial z} + \frac{\partial W}{\partial x}, \quad \gamma_{xy} = \frac{\partial V}{\partial x}$$

Rewriting the constitutive relationships in terms of the stiffness matrix C:

$$\begin{Bmatrix} \sigma_x \\ \sigma_y \\ \sigma_z \\ \tau_{yz} \\ \tau_{xz} \\ \tau_{xy} \end{Bmatrix} = \begin{pmatrix} C_{11} & C_{12} & C_{13} & 0 & 0 & C_{16} \\ C_{12} & C_{22} & C_{23} & 0 & 0 & C_{26} \\ C_{13} & C_{23} & C_{33} & 0 & 0 & C_{36} \\ 0 & 0 & 0 & C_{44} & C_{45} & 0 \\ 0 & 0 & 0 & C_{45} & C_{55} & 0 \\ C_{16} & C_{26} & C_{36} & 0 & 0 & C_{66} \end{pmatrix} \begin{Bmatrix} \varepsilon_x \\ \varepsilon_y \\ \varepsilon_z \\ \gamma_{yz} \\ \gamma_{xz} \\ \gamma_{xy} \end{Bmatrix}$$

and using the strain displacement relations, one has upon substitution into the equilibrium conditions the three governing equations:

$$C_{11} \frac{\partial^2 U}{\partial x^2} + C_{55} \frac{\partial^2 U}{\partial z^2} + \frac{\partial C_{55}}{\partial z} \frac{\partial U}{\partial z} + C_{16} \frac{\partial^2 V}{\partial x^2} + C_{45} \frac{\partial^2 V}{\partial z^2} + \frac{\partial C_{45}}{\partial z} \frac{\partial V}{\partial z}$$

$$+ (C_{13} + C_{55}) \frac{\partial^2 W}{\partial x \partial z} + \frac{\partial C_{55}}{\partial z} \frac{\partial W}{\partial x} = 0$$

$$C_{16} \frac{\partial^2 U}{\partial x^2} + C_{45} \frac{\partial^2 U}{\partial z^2} + \frac{\partial C_{45}}{\partial z} \frac{\partial U}{\partial z} + C_{66} \frac{\partial^2 V}{\partial x^2} + C_{44} \frac{\partial^2 V}{\partial z^2} + \frac{\partial C_{45}}{\partial z} \frac{\partial V}{\partial z}$$

$$+ (C_{36} + C_{45}) \frac{\partial^2 W}{\partial x \partial z} + \frac{\partial C_{45}}{\partial z} \frac{\partial W}{\partial x} = 0$$

$$(C_{55} + C_{13}) \frac{\partial^2 U}{\partial x \partial z} + \frac{\partial C_{13}}{\partial z} \frac{\partial U}{\partial x} + (C_{45} + C_{36}) \frac{\partial^2 V}{\partial x \partial z} + \frac{\partial C_{36}}{\partial z} \frac{\partial V}{\partial x}$$

$$+ C_{55} \frac{\partial^2 W}{\partial x^2} + C_{33} \frac{\partial^2 W}{\partial z^2} + \frac{\partial C_{33}}{\partial z} \frac{\partial W}{\partial z} + \frac{\partial C_{23}}{\partial z} C_4 = 0$$

As seen above, the stiffness coefficients C_{ij} are assumed to be functions of z only. Each lamina is assumed to be homogeneous while the through-the-thickness inhomogeneity of the laminate is accounted for in the formulation. Due to the symmetric nature of the problem, these three elliptical equations for $U(x,z)$, $V(x,z)$ and $W(x,z)$ need only be solved in the first quadrant subject to the following boundary conditions:

$$U(L,z) = U_0 , \quad V(L,z) = W(L,z) = 0$$

$$\left.\frac{\partial U}{\partial z}\right|_{z=0} = \left.\frac{\partial V}{\partial z}\right|_{z=0} = \left.\frac{\partial^2 W}{\partial z^2}\right|_{z=0} = 0$$

$$\left.\frac{\partial^2 U}{\partial x^2}\right|_{x=0} = \left.\frac{\partial V}{\partial x}\right|_{x=0} = \left.\frac{\partial W}{\partial x}\right|_{x=0} = 0 \qquad (5.14)$$

$$\sigma_z(x,t) = \tau_{zy}(x,t) = \tau_{zx}(x,t) = 0 \qquad (5.15)$$

When transverse cracks are placed on the y-z plane as shown in Figure 5-6, boundary conditions (5.14) are replaced only over part of that boundary by the traction-free crack surface conditions. Hence, for the example presented in Figure 5-6, the corresponding modification to (5.14) would be

$$\sigma_x(0,z) = \tau_{xy}(0,z) = \tau_{xz}(0,z) = 0 \quad \text{when} \quad z \in (S_1 \text{ or } S_2)$$

In this formulation C_4 remains as a parameter to be specified just as U_0 so that solutions for U, V and W can be obtained. C_4 represents the constant out of plane strain ε_y, and in this particular case its physical significance is to reflect the constraining effect of the plate extending to $\mp \infty$ in the y direction.

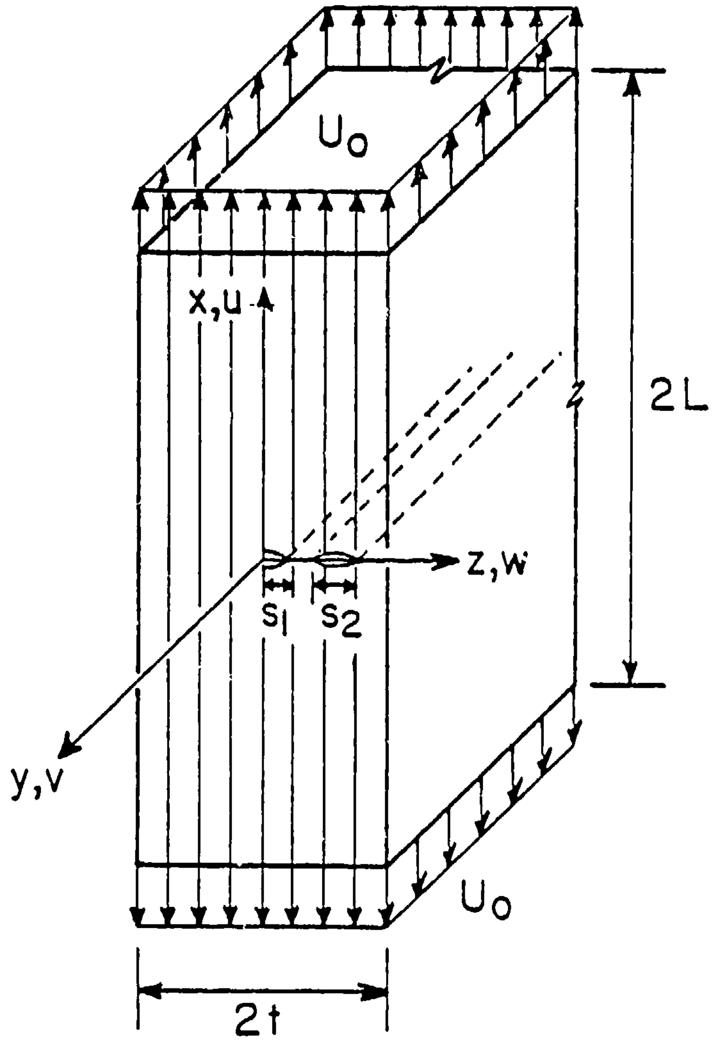

U0
x,u
2L
z,w
s1
s2
y,v
U0
2t

Fig. 5-6 Schematic diagram of geometry of cracked laminate analyzed

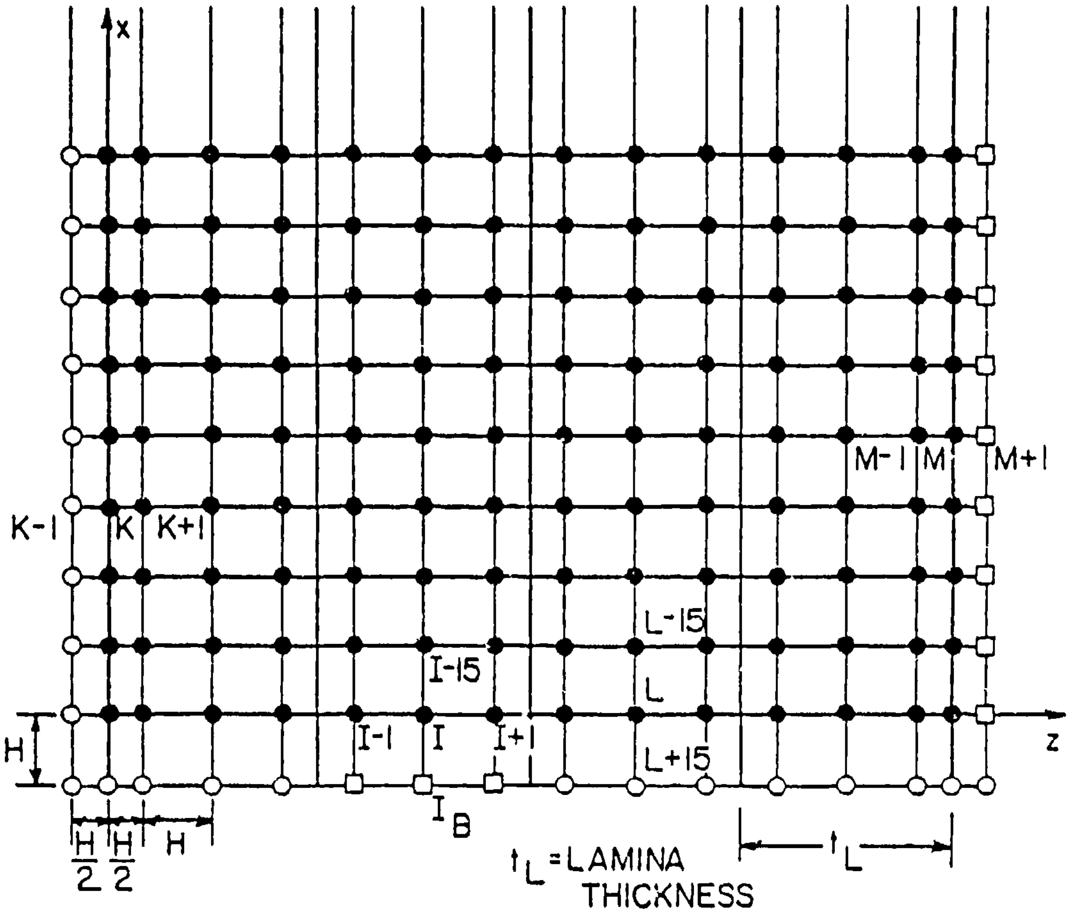

x
z
K-1
K
K+1
M-1
M
M+1
L-15
L
L+15
I-15
I-1
I
I+1
I_B
H
H/2
H/2
H
t_L = LAMINA THICKNESS
t_L

Fig. 5-7 Finite difference grid and node numbering

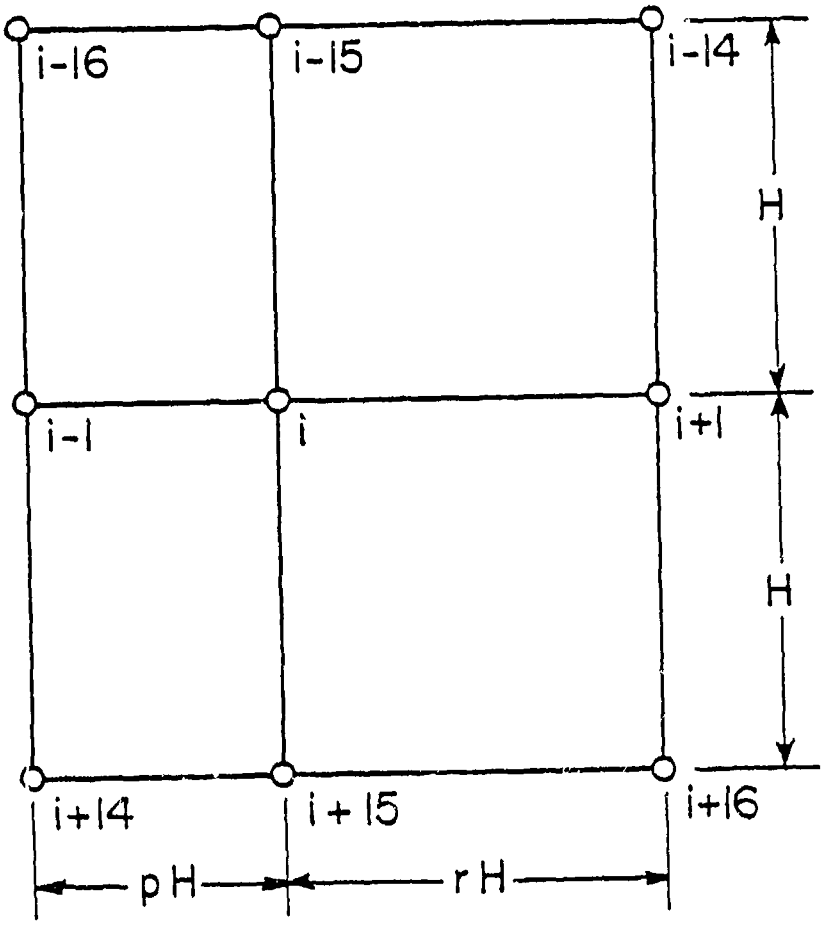
i-16
i-15
i-14
H
i-1
i
i+1
H
i+14
i + 15
i+16
pH
rH

Fig. 5-8 A representative "molecule" of the finite difference grid

In order to obtain a numerical solution for the governing equations by the finite difference method, a grid network must be adapted and the partial differential equations be discretized by expressing the differential operators in terms of finite differences. The finite difference grid, and the node numbering are shown on Figure 5-7. In general, to express the partial derivatives at node i in terms of finite differences, the independent variable is expanded in a Taylor series at nodes neighboring i; these series are truncated and the necessary derivatives are solved for from the linear algebraic equations resulting form the expansions after they are truncated. Since the grid geometry chosen involves variations in node spacing in the z direction, a representative "molecule" is chosen, as shown in Figure 5-8, where

$$0 < p \leq 1$$

$$\text{and} \quad 0 < r \leq 1 \ .$$

Then, the finite difference operators become:

$$\frac{\partial \Phi}{\partial z} = \frac{1}{H}\left[\frac{-r}{p(r+p)}\Phi_{i-1} + \frac{(r-p)}{rp}\Phi_i + \frac{p}{r(p+r)}\Phi_{i+1}\right]$$

$$\frac{\partial \Phi}{\partial x} = \frac{1}{2H}\left[-\Phi_{i+15} + \Phi_{i-15}\right]$$

$$\frac{\partial^2 \Phi}{\partial z^2} = \frac{2}{H^2}\left[\frac{1}{p(p+r)}\Phi_{i-1} - \frac{1}{pr}\Phi_i + \frac{1}{r(p+r)}\Phi_{i+1}\right]$$

$$\frac{\partial^2 \Phi}{\partial x^2} = \frac{1}{H^2}\left[\Phi_{i-15} - 2\Phi_i + \Phi_{i+15}\right]$$

$$\frac{\partial^2 \Phi}{\partial x \partial z} = \frac{1}{2pr(p+r)H^2}\Big[-r^2\Phi_{i-16} - (p^2-r^2)\Phi_{i-15} + p^2\Phi_{i-14} + r^2\Phi_{i+14}$$

$$+ (p^2-r^2)\Phi_{i+15} - p^2\Phi_{i+16}\Big]$$

The truncation error for all of these operators is $O(h^2)$ except for $\frac{\partial^2 \phi}{\partial z^2}$ which is $O(h)$ when $p \neq r$ and $O(h^2)$ if $p=r$.

Substituting these differences into the governing equation, the three partial differential equations are reduced to the following set of three linear algebraic equations to be satisfied at all nodes within the interior of the solution domain.

$$\left[\frac{-r(C^i_{13} + C^i_{55})}{2p(p+r)}\right] W_{i-16} + C^i_{11}\, U_{i-15} + C^i_{16} V_{i-15} + \left[\frac{(r-p)(C^i_{13} + C^i_{55})}{2pr}\right.$$
$$\left. + \frac{1}{4}\,(C^{i+1}_{55} - C^{i-1}_{55})\right] W_{i-15} + \left[\frac{p(C^i_{13} + C^i_{55})}{2r(p+r)}\right] W_{i-14}$$
$$+ \left[\frac{2C^i_{55}}{p(p+r)} + \frac{1}{4}\,(C^{i-1}_{55} - C^{i+1}_{55})\right] U_{i-1} + \left[\frac{2C^i_{45}}{p(p+r)} + \frac{1}{4}\,(C^{i-1}_{45} - C^{i+1}_{45})\right] V_{i-1}$$
$$+ \left[-\,2C^i_{11} - \frac{2}{pr}\, C^i_{55}\right] U_i + \left[-\,2C^i_{16} - \frac{2C^i_{45}}{pr}\right] V_i + \left[\frac{2C^i_{55}}{r(p+r)} + \frac{1}{4}\,(C^{i+1}_{55} - C^{i-1}_{55})\right] U_{i+1}$$
$$+ \left[\frac{2C^i_{45}}{r(r+p)} + \frac{1}{4}\,(C^{i+1}_{45} - C^{i-1}_{45})\right] V_{i+1} + \left[\frac{r(C^i_{13} + C^i_{55})}{2p(p+r)}\right] W_{i+14} + C^i_{11}\, U_{i+15}$$
$$+ \; C^i_{16}\, V_{i+15} + \left[\frac{(C^i_{13} + C^i_{55})(p-r)}{2pr} - \frac{1}{4}\,(C^{i+1}_{55} - C^{i-1}_{55})\right] W_{i+15}$$
$$+ \left[\frac{-p(C^i_{13} + C^i_{55})}{2r(p+r)}\right] W_{i+16} = 0$$

$$\left[\frac{-r(C^i_{36} + C^i_{45})}{2p(p+r)}\right] W_{i-16} + C^i_{16}\, U_{i-15} + C^i_{66}\, V_{i-15}$$
$$+ \left[\frac{(r-p)(C^i_{36} + C^i_{45})}{2pr} + \frac{1}{4}\,(C^{i+1}_{45} - C^{i-1}_{45})\right] W_{i-15} + \left[\frac{p(C^i_{36} + C^i_{45})}{2r(p+r)}\right] W_{i-14}$$

continued

$$
\begin{aligned}
&+ \left[\frac{2C_{45}^{i}}{p(p+r)} - \frac{1}{4}\left(C_{45}^{i+1} - C_{45}^{i-1}\right)\right] U_{i-1} + \left[\frac{2C_{44}^{i}}{p(p+r)} - \frac{1}{4}\left(C_{44}^{i+1} - C_{44}^{i-1}\right)\right] V_{i-1} \\
&+ \left[- 2C_{16}^{i} - \frac{2C_{45}^{i}}{rp}\right] U_{i} + \left[- 2C_{66}^{i} - \frac{2C_{44}^{i}}{pr}\right] V_{i} + \left[\frac{2C_{45}^{i}}{r(p+r)} + \frac{1}{4}\left(C_{45}^{i+1} - C_{45}^{i-1}\right)\right] U_{i+1} \\
&+ \left[\frac{2C_{44}^{i}}{r(p+r)} + \frac{1}{4}\left(C_{44}^{i+1} - C_{44}^{i-1}\right)\right] V_{i+1} + \left[\frac{r(C_{36}^{i} + C_{45}^{i})}{2p(p+r)}\right] W_{i+14} + C_{16}^{i}\, U_{i+15} \\
&+ C_{66}^{i}\, V_{i+15} + \left[\frac{(p-r)(C_{36}^{i} + C_{45}^{i})}{2pr} - \frac{1}{4}\left(C_{45}^{i+1} - C_{45}^{i-1}\right)\right] W_{i+15} \\
&+ \left[\frac{-p(C_{36}^{i} + C_{45}^{i})}{2r(p+r)}\right] W_{i+16} = 0
\end{aligned}
$$

$$
\begin{aligned}
&\left[\frac{-r(C_{55}^{i} + C_{13}^{i})}{2p(p+r)}\right] U_{i-16} + \left[\frac{-r(C_{45}^{i} + C_{36}^{i})}{2p(p+r)}\right] V_{i-16} + \left[\frac{(r-p)(C_{55}^{i} + C_{13}^{i})}{2pr}\right. \\
&\left. + \frac{1}{4}\left(C_{13}^{i+1} - C_{13}^{i-1}\right)\right] U_{i-15} + \left[\frac{(r-p)(C_{45}^{i} + C_{36}^{i})}{2pr} + \frac{1}{4}\left(C_{36}^{i+1} - C_{36}^{i-1}\right)\right] V_{i-15} \\
&+ C_{55}^{i}\, W_{i-15} + \left[\frac{p(C_{55}^{i} + C_{13}^{i})}{2r(p+r)}\right] U_{i-14} + \left[\frac{p(C_{45}^{i} + C_{36}^{i})}{2r(p+r)}\right] V_{i-14} + \left[\frac{2C_{33}^{i}}{p(r+p)}\right. \\
&\left. - \frac{1}{4}\left(C_{33}^{i+1} - C_{33}^{i-1}\right)\right] W_{i-1} + \left[-2C_{55}^{i} - \frac{2C_{33}^{i}}{pr}\right] W_{i} + \left[\frac{2C_{33}^{i}}{r(p+r)} + \frac{1}{4}\left(C_{33}^{i+1} - C_{33}^{i-1}\right)\right] W_{i+1} \\
&+ \left[\frac{r(C_{55}^{i} + C_{13}^{i})}{2p(p+r)}\right] U_{i+14} + \left[\frac{r(C_{45}^{i} + C_{36}^{i}}{2p(p+r)}\right] V_{i+14} + \left[\frac{(p-r)(C_{55}^{i} + C_{13}^{i})}{2pr}\right. \\
&\left. - \frac{1}{4}\left(C_{13}^{i+1} - C_{13}^{i-1}\right)\right] U_{i+15} + \left[\frac{(p-r)(C_{45}^{i} + C_{36}^{i})}{2pr} - \frac{1}{4}\left(C_{36}^{i+1} - C_{36}^{i-1}\right)\right] V_{i+1} \\
&+ C_{55}^{i}\, W_{i+15} + \left[\frac{-p(C_{55}^{i} + C_{13}^{i})}{2r(p+r)}\right] U_{i+16} + \left[\frac{-p(C_{45}^{i} + C_{36}^{i})}{2r(p+r)}\right] V_{i+16} \\
&= \frac{-HC_{4}}{2}\left(C_{23}^{i+1} - C_{23}^{i-1}\right)
\end{aligned}
$$

By applying these discretized equilibrium conditions at N nodes in the grid, a set of $3N$ linear algebraic equations for the $3N$ unknown nodal displacement values is obtained.

The governing equations are satisfied at all nodes including those that are on the boundaries. This inevitably results in extrapolated nodes outside the physical boundaries, the nodal values for which become additional unknowns. The nodal values for the extrapolated nodes shown with open circles in Figure 2 can be expressed in terms of the nodal values at nodes symmetrically located with respect to the x or z axes depending on the location of the node along the boundary.

Therefore, along $z = 0$:

$$U(K-1) = U(K+1)$$

$$V(K-1) = V(K+1)$$

$$W(K-1) = -W(K+1)$$

and along $x = 0$

$$U(L-15) = -U(L+15)$$

$$V(L-15) = V(L+15)$$

$$W(L-15) = W(L+15)$$

The nodal variables for the extrapolated nodes shown by squares are independent values, and the additional equations required to determine them are obtained from the traction-free surface boundary conditions. For example, I is a node on the crack surface. Therefore, at I, in addition to the three equilibrium conditions, the boundary conditions

$$\sigma_x = C_{11}^I \frac{\partial U}{\partial x} + C_{12}^I C_4 + C_{13}^I \frac{\partial W}{\partial z} + C_{16}^I \frac{\partial V}{\partial x} = 0$$

$$\tau_{zx} = C_{45}^I \frac{\partial V}{\partial z} + C_{55}^I \left(\frac{\partial W}{\partial x} + \frac{\partial U}{\partial z}\right) = 0$$

$$\tau_{xy} = C_{16}^I \frac{\partial U}{\partial x} + C_{26}^I C_4 + C_{36}^I \frac{\partial W}{\partial z} + C_{66}^I \frac{\partial V}{\partial x} = 0$$

must be satisfied.

Discretizing these three conditions with central differences for $O(h^2)$ accuracy:

$$C_{11}^{I}\,U_{I-15} + C_{16}^{I}\,V_{I-15} - \frac{2r}{p(r+p)}\,C_{13}^{I}\,W_{I-15} + \frac{2(r-p)}{rp}\,C_{13}^{I}\,W_{I} + \frac{2p}{r(p+r)}\,C_{13}^{I}\,W_{I+1} - C_{11}^{I}\,U_{IB} - C_{16}^{I}\,V_{IB} = -2H\,C_{12}^{I}\,C_{4}$$

$$C_{55}^{I}\,W_{I-15} - \frac{2r}{p(r+p)}\,C_{55}^{I}\,U_{I-1} - \frac{2r}{p(r+p)}\,C_{45}^{I}\,V_{I-1} + \frac{2(r-p)}{rp}\,C_{55}^{I}\,U_{I} + \frac{2(r-p)}{rp}\,C_{45}^{I}\,V_{I} + \frac{2p}{r(p+r)}\,C_{55}^{I}\,U_{I+1} + \frac{2p}{r(p+r)}\,C_{45}^{I}\,V_{I+1} - C_{55}^{I}\,W_{IB} = 0$$

$$C_{16}^{I}\,U_{I-15} + C_{66}^{I}\,V_{I-15} - \frac{2r}{p(r+p)}\,C_{36}^{I}\,W_{I-1} + \frac{2(r-p)}{rp}\,C_{36}^{I}\,W_{I} + \frac{2p}{r(p+r)}\,C_{36}^{I}\,W_{I+1} - C_{16}^{I}\,U_{IB} - C_{66}^{I}\,V_{IB} = -\,2H\,C_{26}^{I}\,C_{4}$$

Similarly, for node M on the surface of the plate the boundary conditions (5.15) are discretized and applied.

$$C_{13}^{M}\,U_{M-15} + C_{36}^{M}\,V_{M-15} - 2\,C_{33}^{M}\,W_{M-1} + 2\,C_{33}^{M}\,W_{M+1} - C_{13}^{M}\,U_{M+15} - C_{36}^{M}\,V_{M+15} = -\,2H\,C_{23}^{M}\,C_{4}$$

$$C_{55}^{M}\,W_{M-15} - 2\,C_{55}^{M}\,U_{M-1} - 2\,C_{45}^{M}\,V_{M-1} + 2\,C_{55}^{M}\,U_{M+1} + 2\,C_{45}\,V_{M+1} - C_{55}^{M}\,W_{M+15} = 0$$

$$C_{45}^{M}\,W_{M-15} - 2\,C_{44}^{M}\,V_{M-1} - 2\,C_{45}^{M}\,U_{M-1} + 2\,C_{44}^{M}\,V_{M+1} + 2\,C_{45}^{M}\,U_{M+1} - C_{45}^{M}\,W_{M+15} = 0$$

With the inclusion of these boundary conditions the number of algebraic equations is increased to equal the number of independent nodal variables. To eliminate the possibility of a rigid body translation in the x direction an additional condition is provided by constraining one node at $x = 0$ by invoking

$U(0,0) = 0$ if no crack exists at the origin.

$u(0,a/2) = 0$ with a crack at the origin extending over the interval $-\frac{a}{2} \le z \le \frac{a}{2}$

The resulting system of algebraic equations can be expressed in matrix form as

$$\left[\begin{array}{c|c} p_{\alpha\alpha} & p_{\alpha\beta} \\ \hline p_{\beta\alpha} & p_{\beta\beta} \end{array}\right] \left\{\begin{array}{c} \Phi_\alpha \\ \hline \Phi_\beta \end{array}\right\} = \left\{\begin{array}{c} Q_\alpha \\ \hline Q_\beta \end{array}\right\}$$

where $[p]$ is the matrix of coefficients, $\{\Phi_\alpha\}$ and $\{\Phi_\beta\}$ represent the prescribed nodal variables at $x = L$ and independent nodal variables respectively. The solution for $\{\Phi_\beta\}$ will then be obtained from

$$[P_{\beta\beta}]\{\Phi_\beta\} = \{ R \} \qquad (5.16)$$

where $\{ R \} = \{Q_\beta\} - [p_{\beta\alpha}]\{\Phi_\alpha\}$

The resulting matrix of coefficients $[p_{\beta\beta}]$ is of a non-symmetric banded type. When the actual size of the system of equations for a sample solution is considered, it is easily seen that an in-core storage of the elements within the band quickly becomes undesirable (if not impossible) for increasing aspect ratios ($AR = L/t$). For example, an aspect ratio of 10 would result in a 6750 x 6750 matrix requiring over 5,400 k-bytes of storage space in double precision for the elements within the band. This necessitates a solution scheme in which only a part of the non-zero matrix elements are stored in the main core. To achieve this, a solution scheme was constructed by partitioning the matrix such that it is of block tridiagonal form:

$$[p_{\beta\beta}] = \begin{bmatrix} Q_1 & R_1 & & & \\ S_2 & Q_2 & R_2 & & 0 \\ & S_3 & Q_3 & R_3 & \\ & 0 & & & \\ & & & S_N & Q_N \end{bmatrix}$$

where Q_k is $M_k \times M_k$

S_k is $M_k \times M_{k-1}$

and R_k is $M_k \times M_{k+1}$

Then, the tridiagonal algorithm is applied in such a way that at any given step $[S_k]$, $[Q_k]$ and $[R_k]$ are constructed, processed, and the intermediate solution is transferred to an external storage device. Once all the blocks ($k=1,2,\ldots,N$) are processed, the intermediate solutions are transferred back into the memory again in blocks to be processed to yield the final solution for the linear system (5.16). In this particular example each partition has a maximum size of 45 x 45 eliminating all practical difficulties in storage. Processing of these blocks requires the solution of linear systems of 45 x 45 size which is accomplished by a Gaussian Elimination scheme with both row-wise and column-wise pivoting.

Once the nodal values of U, V and W are determined, the strains are obtained by numerical differentiation, and the stresses are evaluated through the constitutive relations.

TABLE V-II

IN-PLANE STRESSES*

	FINITE DIFFERENCE			LAMINATE THEORY		
	0°	90°	∓ 45°	0°	90°	∓ 45°
σ_x	19.6	1.35	5.15	19.5	1.33	5.13
σ_y	0.09	-3.55	3.58	0.09	-3.55	3.57
τ_{xy}	0	0	∓ 3.65	0	0	∓ 3.64

*Fixed strains:

$\varepsilon_x^\circ = 10^{-3}$

$\varepsilon_y^\circ = -2 \times 10^{-4}$

As a check on the validity of the solution scheme the calculated stresses for an uncracked laminate were compared with laminate values, as shown in Table V-II. The agreement is seen to be complete. Of course the finite difference analysis yields all six stress or strain components, not just the in-plane values.

Some early results for a cracked laminate are shown in Figs. 5-9 and 5-10. These figures show the through-the-thickness distribution of the axial normal stress when a crack has formed in the center two plies (on either side of the centerline) in a type I and type II laminate, respectively. In the type I laminate the stress in the (-45°) ply next to the crack is increased by sixty percent at the first nodal point in that layer. The influence of the crack is seen to die out quickly with very little disturbance observed beyond the first ply beside the crack. The normal stress in the 0° ply is essentially undisturbed.

The stress distribution in the type II laminate is very different. Of course, a different set of plies were broken, a stiffer set in this case, so that the stress released was larger. The nearest constraining ply (a -45° ply in both cases) undergoes about a hundred percent increase in stress, compared to sixty percent for type I. The stress in the next nearest ply is barely noticeable in both cases. However, the normal stress in the 0° ply increases by five percent or so. These details are impossible to obtain without an analysis of this type. The possibility of experimentally measuring, or intuitively guessing these details is regarded as remote by the authors.

Of course, numerous other details are needed in order to draw conclusions from the analysis. They are being generated presently.

These analyses have been, and will be, a valuable aid in our

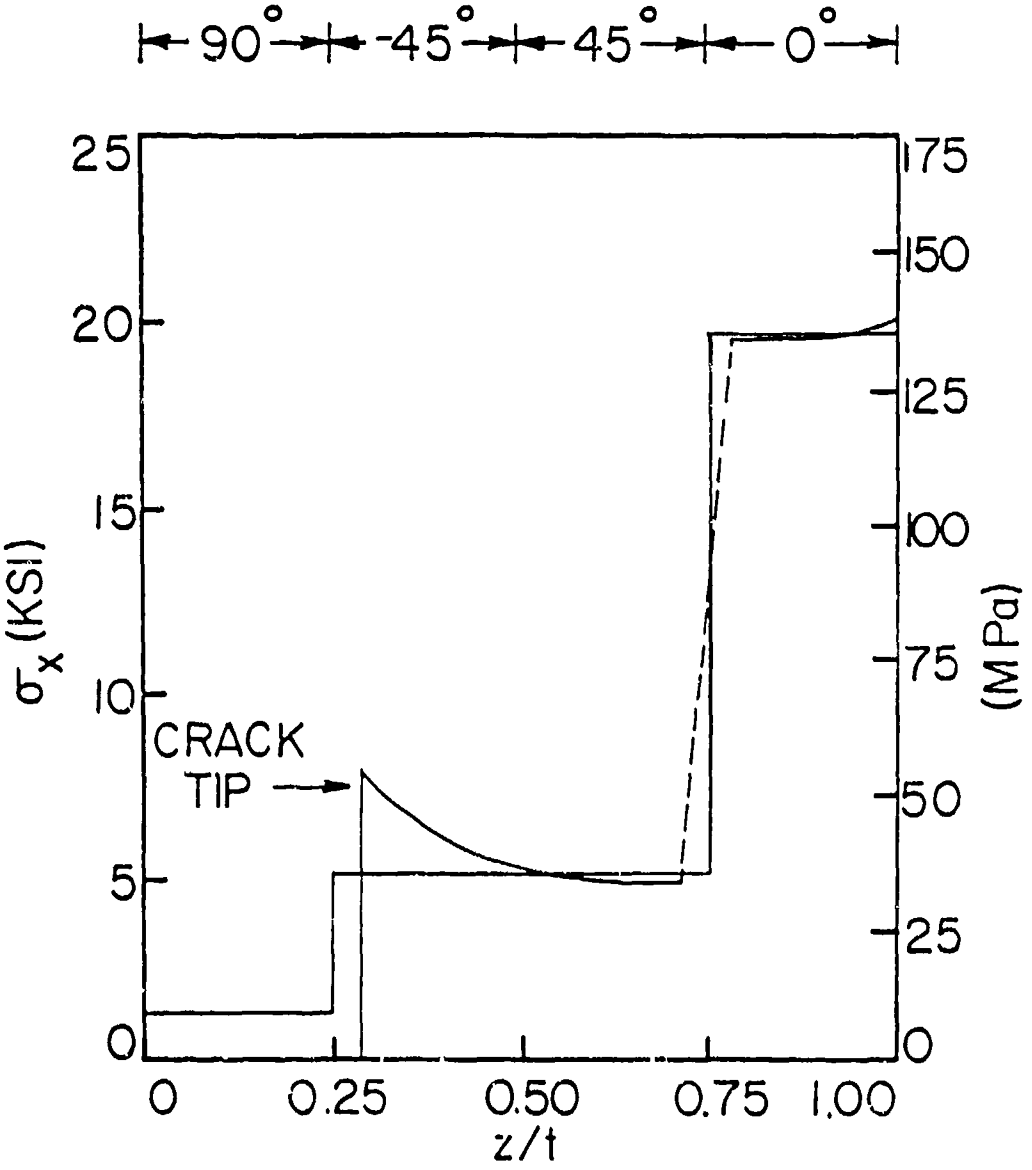

Fig. 5-9 Distribution of axial normal stress as a function of the thickness position for a type I laminate

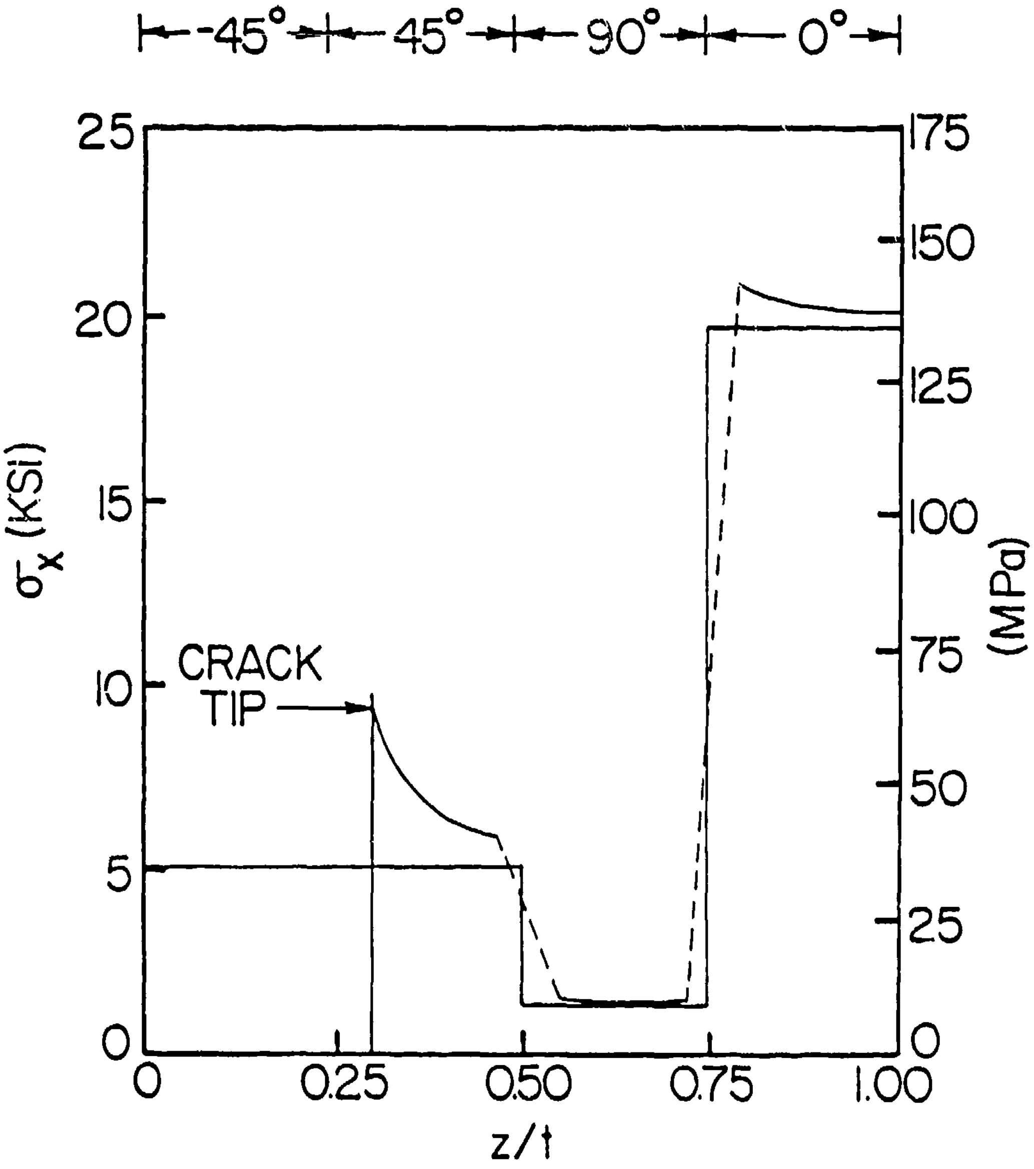

Fig. 5-10 Distribution of axial normal stress as a function of the thickness position for a type II laminate

interpretation of experimental data and in the development of our understanding of the behavior under study. They also serve to predict behavior not yet observed.

SECTION VI

OBSERVATIONS WITH THERMOGRAPHY

The vibrothermography technique, originally developed under a previous contract with AFML as reported in reference [2], has continued to be investigated. Emphasis has been placed upon the experimental determination of the kinds and sizes of flaws that can be delineated and the analytical investigation of the heat conduction problem in a material composed of orthotropic layers. The latter investigation was undertaken to determine the influence of anisotropic heat conduction effects upon the observed surface heat patterns resulting from subsurface heat sources. This section gives details of the analytical model for the heat conduction problem, the experimental techniques, and the resulting observations.

The analytical model used here is very similar to one reported by Trezek and Balk [10]. These investigators considered the use of thermal imaging techniques for the nondestructive testing of metals. In their case, provocative techniques were used to obtain thermal radiation patterns for various materials and flaws. Stressing the importance of the use of an analytical model to aid in the interpretation of these patterns, the authors used a three-dimensional finite difference heat conduction analysis. They were able to input various flaw types to obtain a first order approximation of the expected thermal pattern that could then be compared with experiment.

The literature also contains several schemes for defining the diffusion of heat through a composite material. Maewal, Bache, and Hegemier [11] showed good results using a continuum model for this process. An approximation was obtained by using a truncated power series solution. In general, the zeroth or the first order solution is sufficient for most problems. Estes and Mulholland [12] have developed a rather complex mathematical method for describing the diffusion of heat through a multi-layered composite material. The scheme developed in this paper is quite complex and does not allow for internal heat generation. It does, however, allow for rather complex boundary conditions.

The model used in the present work begins with the partial differential heat conduction equation for an anisotropic material written as (see any standard text such as reference [13]):

$$\rho c_p \frac{\partial^2 t}{\partial \tau} = K_{ij} \frac{\partial^2 t}{\partial x_i \partial x_j} \tag{6-1}$$

where ρ is the mass density; c_p, the specific heat at constant pressure; t, the temperature; and τ, the time. Any material that has orthotropic symmetry will possess only three independent thermal conductivities, K_{11}, K_{22} and K_{33} when the x,y,z coordinate axes are taken to be parallel to the symmetry axes of the material. For a composite laminate composed of several layers of material oriented in different directions, it is often convenient to choose one fixed set of coordinate axes and refer each ply to it. In this case since the chosen coordinate system is not in general parallel to the material coordinate system, it is necessary to rotate the thermal conductivity tensor into the chosen system. Since composite laminates are composed of parallel planes of fibers, the only rotations that need to be considered are in the 1,2 plane, that is, the plane of the fibers. With this rotation, the thermal conductivity tensor becomes

$$K'_{ik} = \begin{bmatrix} K_{xx} & K_{xy} & 0 \\ K_{xy} & K_{yy} & 0 \\ 0 & 0 & K_{zz} \end{bmatrix} . \tag{6-2}$$

where

$$
\begin{aligned}
K_{xx} &= \cos^2\theta\ K_{11} + \sin^2\theta\ K_{22} \\
K_{xy} &= \cos\theta \sin\theta\ K_{11} - \cos\theta \sin\theta\ K_{22} \\
K_{yx} &= K_{xy} \\
K_{yy} &= \sin^2\theta\ K_{11} + \cos^2\theta\ K_{22} \\
K_{zz} &= K_{33} \\
K_{xz} &= K_{zx} = K_{yz} = K_{zy} = 0 \quad ,
\end{aligned}
\tag{6-3}
$$

The heat conduction equation for each laminate can now be written as

$$
\rho c_p \frac{\partial t}{\partial \tau} = K_{xx} \frac{\partial^2 t}{\partial x^2} + K_{yy} \frac{\partial^2 t}{\partial y^2} + K_{zz} \frac{\partial^2 t}{\partial z^2} + 2K_{xy} \frac{\partial^2 t}{\partial x \partial y} \tag{6-4}
$$

To solve equation (6-4), a finite difference method demonstrated by Chapman [14] was used. The spacial and time derivatives in eqn. (6-4) were replaced by finite difference approximations based upon Taylor expansions. A change in the system of notation as shown in Fig. 6-1, was employed so that the updated temperature at an arbitrary mode, t'_a , can be written from equ. (6-4) as

$$
\begin{aligned}
t'_a = t_a\left[1 - \frac{\Delta\tau}{\rho c_p\ \Delta V}\left[\frac{2}{R_{xx}} + \frac{2}{R_{yy}} + \frac{2}{R_{zz}}\right]\right] + \frac{\Delta\tau}{\rho c_p\ \Delta V}\left[\frac{t_d + t_e}{R_{xx}}\right. \\
\left. + \frac{t_b + t_c}{R_{yy}} + \frac{t_f + t_g}{R_{zz}} \quad \frac{t_{ce} + t_{bd} - t_{cd} - t_{be}}{R_{xy}}\right]
\end{aligned}
\tag{6-5}
$$

where

$$
R_{xx} = \frac{\Delta x}{K_{xx}\Delta y \Delta z} \quad , \quad R_{yy} = \frac{\Delta y}{K_{yy}\Delta x \Delta z}
$$

$$
R_{zz} = \frac{\Delta z}{K_{zz}\Delta x \Delta y} \quad , \quad R_{xy} = \frac{2}{K_{xy}\Delta z}
$$

Equation (6-5) was applied to the analysis of a symmetric, positive laminate of the form $[\theta_1,\theta_2,\theta_3,\theta_4]_s$. For ease in computer coding, the

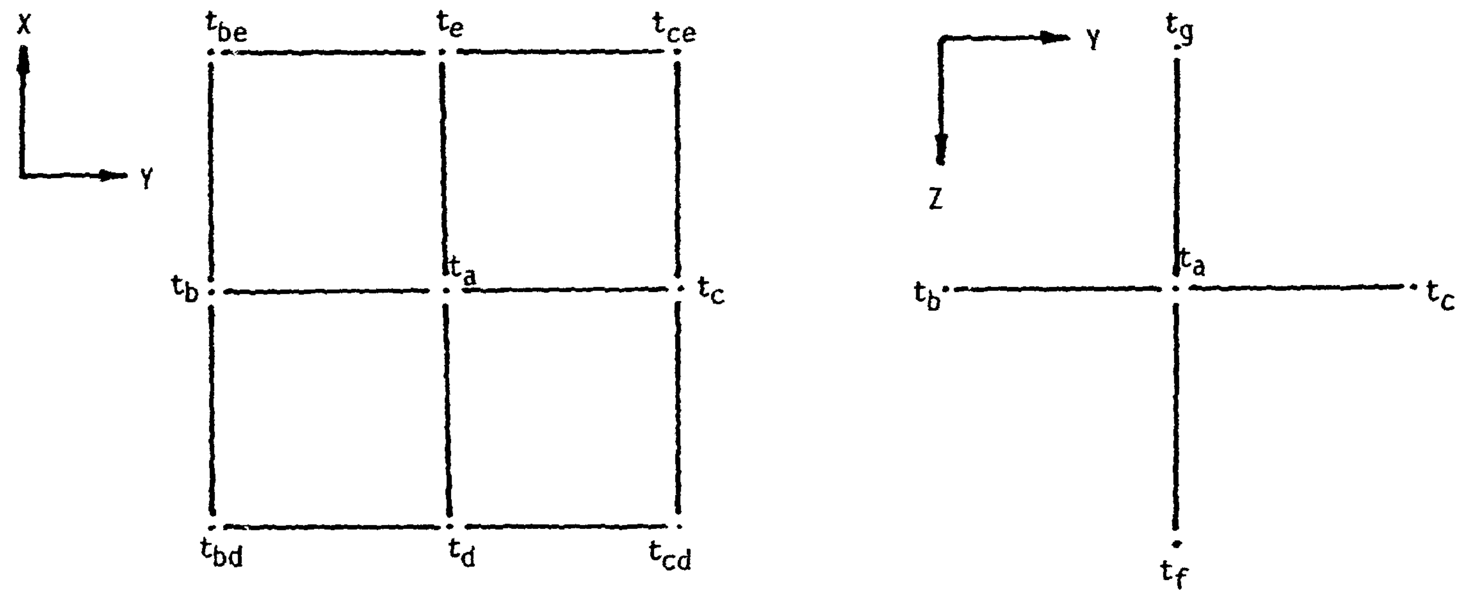
X
Y
t_{be}
t_e
t_{ce}
t_b
t_a
t_c
t_{bd}
t_d
t_{cd}
Y
Z
t_g
t_b
t_a
t_c
t_f

Fig. 6-1 Notation system used to denote temperatures of an arbitrary nodal element and its nearest neighbors

numerical numbering scheme shown in Fig 6-2 was used so that, if $t_a = T(N)$, then

$$\begin{array}{lll} t_b = T(N-1) & t_f = TD(N) & t_{bd} = T(N+9) \\ t_c = T(N+1) & t_g = TU(N) & t_{be} = T(N-11) \\ t_d = T(N+10) & t_{ce} = T(N-9) & t_{cd} = T(N+11) \\ t_e = T(N-10) & & \end{array} \qquad (6\text{-}6)$$

Now the boundary conditions which must be satisfied for the outer nodes alter the essential form of eqn (6-5). In fact, for any arbitrary layer it was necessary to write nine different equations, one equation for each corner node of the layer, one equation for the nodes along each of the four edges, and one equation for the interior nodes. The boundary conditions that were used were (i) an adiabatic midplane due to the symmetry conditions, (ii) adiabatic surfaces along the short edges, that is, along the edges in the y-z plane, and (iii) convective surfaces along the top surface and long edges, that is, the free edges in the x-z plane. Also, it was necessary to separate R_{zz} into R_u for conduction or convection from above and R_d for conduction from below. In addition, R_c was defined as the convective resistance and T_r as room temperature. Thus, R_c was written as

$$R_c = \frac{1}{h\Delta x\Delta z}$$

and, for the surface ply only,

$$R_u = \frac{1}{h\Delta x\Delta y}$$

where h is the film coefficient. With these boundary conditions and values of R, equation (6-5) was written specifically for each node type. For example, referring again to the numbering system in Fig 6-2, a typical equation for a corner node can be written as,

$$\delta x = \frac{1}{2}\Delta X \qquad \delta y = \frac{1}{2}\Delta Y \qquad \delta z = \Delta Z$$

$$T_1' = T_1\left[1 - \frac{2\Delta\tau}{\rho c_p\ \Delta V}\left[\frac{1}{R_{xx}} + \frac{1}{R_{yy}} + \frac{1}{R_c} + \frac{1}{2R_u} + \frac{1}{2R_d}\right]\right] + \frac{2\Delta\tau}{\rho c_p\ \Delta V}\left[\frac{T_{11}}{R_{xx}} + \frac{T_2}{R_{yy}} + \frac{T_R}{R_c} + \frac{TU_1}{2R_u} + \frac{TD_1}{2R_d}\right] \qquad (6\text{-}7)$$

The respective equations for the other three corner nodes are similar, only the nodal designations of T changing according to the adjacent node numbers. The remaining five equations were written in a like fashion for the nodes along each of the four edges and for the interior nodes.

By examining eqn (6-7) (and the other eight nodal equations) it can be seen that there is a stability requirement on the value of $\Delta\tau$. If $\Delta\tau$ is chosen large enough, the coefficient of T_1 in eqn (6-7) will become negative. If this is allowed to happen, it would imply that the hotter the temperature T_1 at time τ, the cooler the temperature T_1' at time $\tau + \Delta\tau$. Since this is obviously physically impossible, it is necessary to choose $\Delta\tau$ so that the coefficient of T_1 in eqn (6-7) (and the respective coefficient of each T(N) in the remaining eight equations) remains positive. The requirement on $\Delta\tau$ can be written as

$$\Delta\tau < \frac{\rho c_p \Delta V}{2}\left\{\frac{1}{R_c} + \frac{1}{R_{xx}} + \frac{1}{R_{yy}} + \frac{1}{2R_u} + \frac{1}{2R_d}\right\}^{-1} \qquad (6\text{-}8)$$

Heat sources in the laminate were modeled as having a linear temperature increase with time. An increasing temperature source was chosen instead of a steady state one to better model the vibrothermography

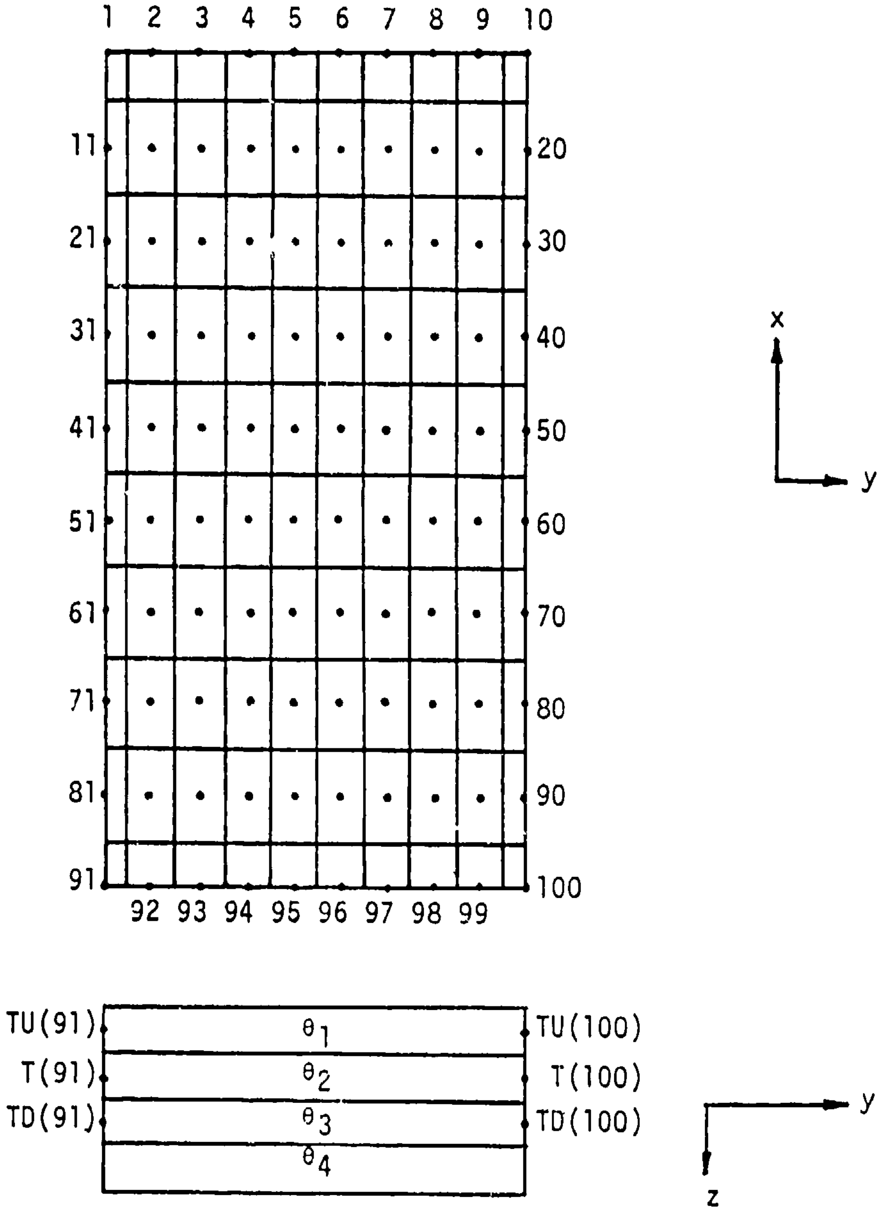
1 2 3 4 5 6 7 8 9 10
11
20
21
30
31
40
41
50
51
60
61
70
71
80
81
90
91
100
92 93 94 95 96 97 98 99
x
y
TU(91)
T(91)
TD(91)
TU(100)
T(100)
TD(100)
θ_1
θ_2
θ_3
θ_4
y
z

Fig. 6-2 Numbering system used to denote nodal elements for computer code

experiment. Thus when the shaker is turned on at initial time, every point in the laminate is at the same room temperature. As the specimen begins to vibrate, those regions that serve as local hot spots begin to have a temperature rise. Of course they would reach a steady state and would not continue to heat indefinitely, but the numberical iteration procedure is run for a very short time so that one need not worry about developing unrealistically high temperatures. In the future, different temperature-time functions could easily be incorporated into the program. The heat sources, for the purposes of the computer program, can be located anywhere in the half thickness of the laminate with up to thirty nodes per layer designated as heat sources.

A program based upon the previous discussion was written and used to calculate the temperature patterns resulting from a number of heat sources having different geometries. The heat source geometries were chosen by making reasonable estimations as to the shape and size of real damaged regions observed in composite laminates. In several cases, the geometry of the heat source was chosen to match the geometry of known flaws manufactured in the laminates during the fabrication process. The material properties used in the numerical analysis are given in Table VI-I. The resulting temperature pattern at the specimen surface was calculated at the end of a given number of iterations corresponding to approximately 1.5 seconds of real time. It was found from calculations using a steady heat source that the subsurface heat pattern is conducted very rapidly to the surface. Hence the time interval chosen to end the iteration process for the linear increasing temperature source was more than sufficient to obtain a good surface heat pattern due to the internal heat source. Increasing the final time would have served to only increase the surface temperatures, and not their distribution. The results of the

Table VI-I. Material properties used.

Property	Graphite-epoxy	Boron-epoxy
Conductivity 1-dir. (cal/C-cm-sec)	0.01033 [15]	0.00551 [16]
Conductivity 2-dir. (cal/C-cm-sec)	0.00155 [15]	0.00248 [16]
Conductivity 3-dir. (cal/C-cm-sec)	0.00125 *	0.00200 *
Film Coefficient (cal/C-cm^2-sec)	0.0007 * [14]	0.0007 *
Density (g/cm^3)	1.61 [15]	1.61 *
Specific heat (cal/C-g)	0.22 [17]	0.28 [17]

*Estimated value based on best information in Refs. [14-17].

numerical calculations are presented here in the form of isothermal plots. A temperature of 20 degrees Celsius was used as ambient and two isotherms were drawn in each figure presented below, one for 20.3°C (fine line) and one for 22.0°C (thick line).

In order to form the shape patterns required to simulate the damage in specimens, a certain number of elements must be declared as damaged elements, as mentioned earlier. Since the number of elements is limited to one hundred per ply, a certain size distortion occurs in several of the computer generated temperature patterns. In order to reduce this distortion, in some cases the dimensions of the interior elements were changed from rectangular, which naturally fitted the specimen's overall geometry, to square. For these cases, the area actually analyzed is represented in the figures as being that between the dashed lines.

The first heat sources chosen for study were selected to represent the damage observed in a graphite-epoxy, $[0,\pm45,90]_s$, laminate that had been quasi-statically loaded to 12 KN (2700 lb.). Edge delaminations, as well as transverse cracks, were apparent in this specimen. The vibrothermography pattern, experimentally obtained at a frequency of approximately 18,000 Hz, is shown in Figure 6-3. Here it can be seen that at this frequency there is an obvious heat source only along one edge of the specimen, the extent and depth of which closely corresponds to the edge delamination. Thus, again referring to Fig 6-2, elements 30, 40, 50, 70 and 80 in the innermost layer of the laminate were chosen for the heat source. The resulting calculated thermograph is shown in Fig 6-4. As can be seen, the patterns in Figs 6-3 and 6-4 are very similar. In the computer generated temperature pattern, the indentation between the two generating areas is larger than the actual thermograph.

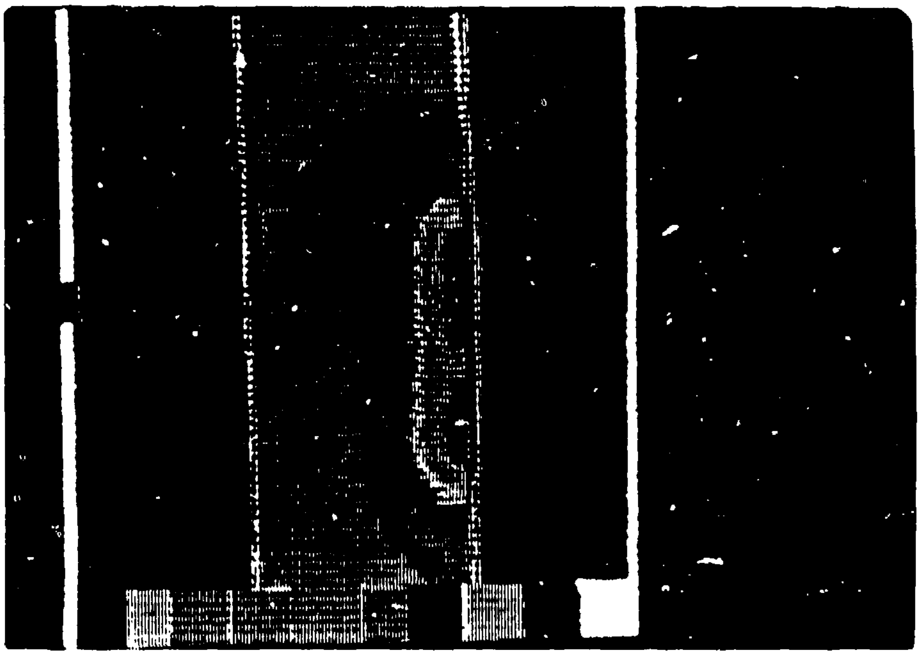

Fig. 6-3 Thermograph of type I specimen after quasi-static tensile loading to 12 KN (2700 lb.)

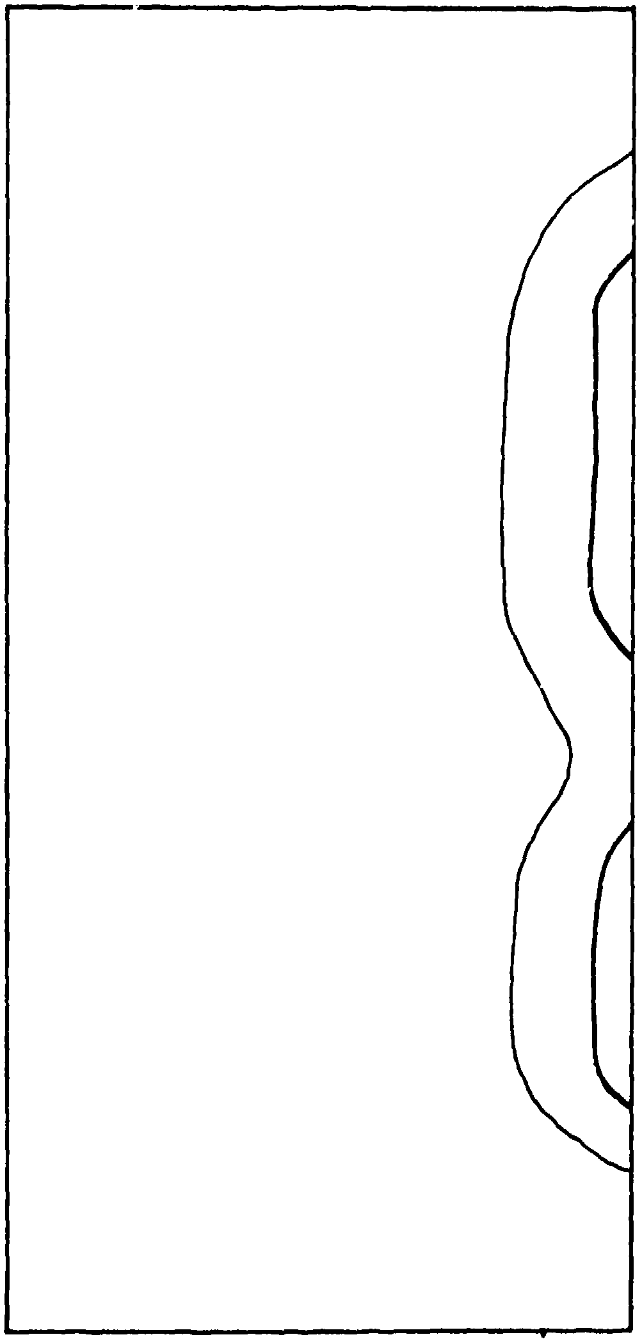

Fig. 6-4 Computer generated thermograph modeling edge delamination in type I specimen

This discrepancy could perhaps be remedied if more elements per ply were used, which would allow the size of each node to be smaller. Given smaller nodes, the gap between the two generating patterns could be reduced and the indentation seen in the computer generated temperature pattern would also be reduced. Also, it is possible that the region between the two intense areas on the thermograph is generating at a lower rate than the two intense areas. The computer program, as written, does not allow for varying degrees of heat generation. The computer program did, however, reasonably well reproduce the experimental temperature pattern with the given input data.

When the frequency of the shaker to which the specimen was attached was slightly increased (by less than 2%), a second heat source on the other edge appeared, Fig 6-5, again corresponding to an edge delamination there. The two Figs 6-3 and 6-5 are interesting evidence of the strong dependence of the heat patterns on vibration frequency. In addition to the new heat source, the two sources on the right edge appear at a higher intensity than before; and the lower source on the right edge appears larger with respect to the upper source on the right edge. The increased size of the lower source could be either because of a higher rate of heat generation or because a new area of the delamination has been activated at this new frequency. For use in the computer program, the increased size of this high temperature pattern is modeled as an increased size of the generating region. The heat generators input into the computer program to model the damage responsible for the thermograph in Fig 6-5 were elements 30, 32, 40, 50, 69, 70, 79 and 80 in the innermost layer. The thermograph resulting from the computer generated temperature pattern for this input data is seen in Fig 6-6. The pattern on the right is a reasonable match for the experimental

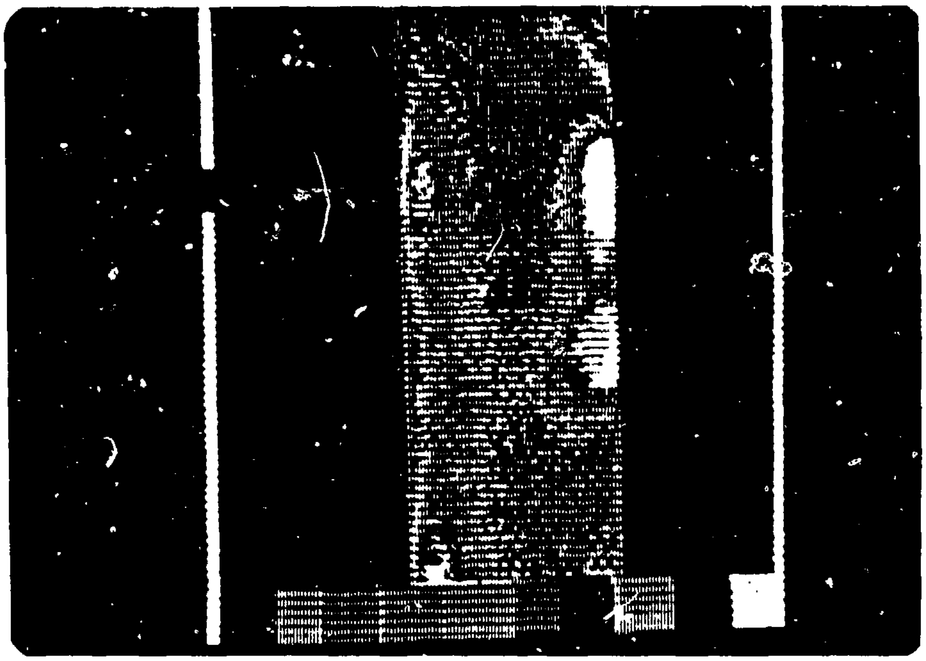

Fig. 6-5 Thermograph of type I specimen after quasi-static tensile loading to 12 KN (2700 lb.). Same specimen as Fig. 6-3, vibrated at a slightly different frequency

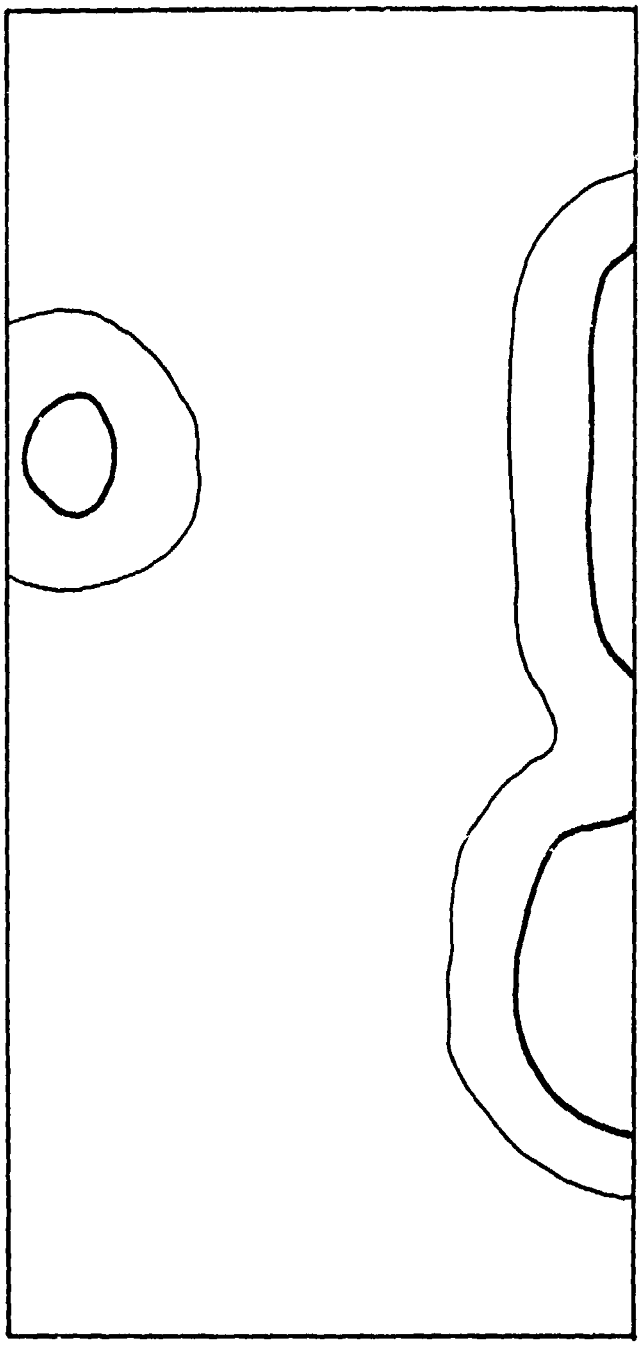

Fig. 6-6 Computer generated thermograph of type I specimen with edge delaminations modeled along both edges

thermograph. The restriction of the size and shape of the elements causes some discrepancy again in the gap between the two intense sources on the right. The computer generated pattern on the left is not an especially good match with regard to the lower temperature isotherm. This is obviously due to the failure to put in the lower heat source on the left hand edge and also the inadequacies of the program due to the large element sizes.

A second type I graphite-epoxy laminate was loaded quasi-statically to 8.9 KN (2000 lb.), unloaded and mounted in the shaker. The resulting vibrothermograph is shown in Fig 6-7. Only one very minor heat source can be seen along the right edge. The high intensity heat pattern at the bottom of the specimen was caused by heat being conducted into the specimen from the shaker, which runs quite hot after several minutes of operation. This specimen was subsequently subjected to 10,000 cycles of fatigue loading at 1 Hz , with a load ratio of 0.1 and a maximum load of 8.9 KN (2000 lb.). A second vibrothermograph, Fig 6-8, taken after fatigue shows that the area of the damaged region giving rise to the low intensity temperature pattern of Fig 6-7 has grown and intensified. For analysis in the finite difference program, the damage responsible for heat generation was modeled as being at the midplane in elements 1, 10, 21, 30, 40, 50, 60, 69, 70 and 80. The temperature pattern resulting from this analysis is shown in Fig 6-9. Agreement between the experimental thermograph and the analytically obtained thermograph is very good. No significant differences can be seen in the two patterns.

An eight-ply boron-epoxy, $[0,\pm45,0]_s$, laminate, 1" x 7" with a 0.25" hole in the center was loaded in three point bending until a "greenstick" type fracture occurred across the width of the laminate at the hole. Observation of the specimen indicated that the outer laminae

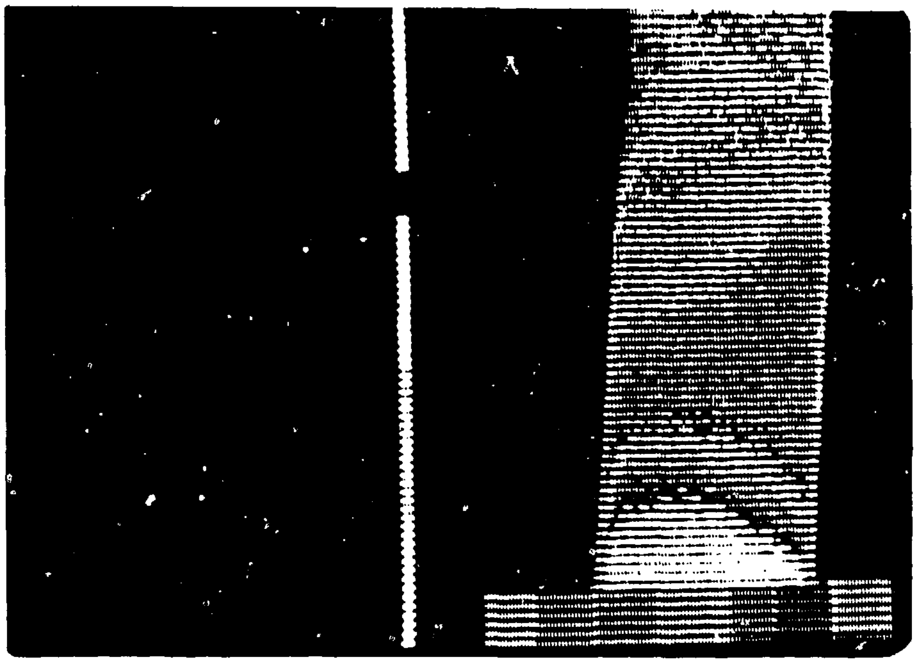

Fig. 6-7 Thermograph of type I specimen after quasi-static tensile loading to 8.9 KN (2000 lb.)

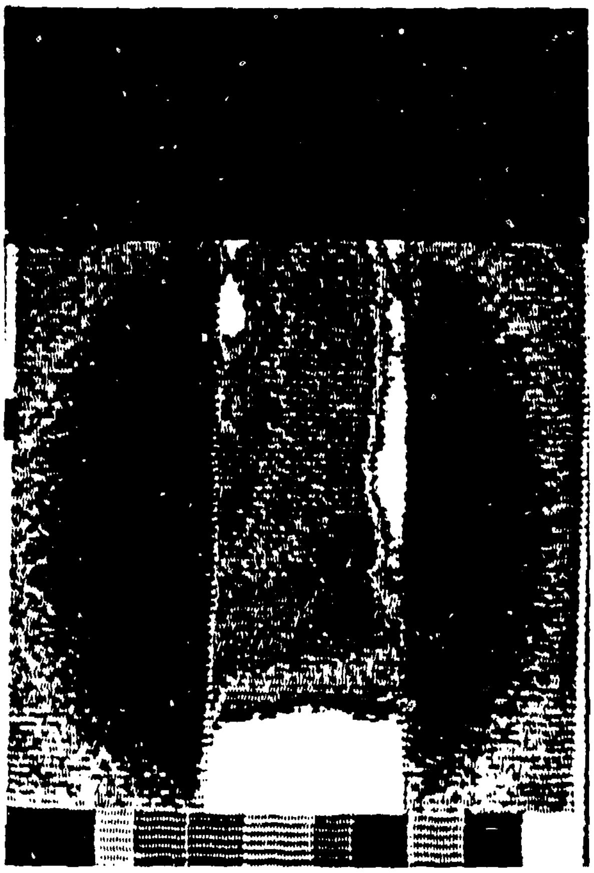

Fig. 6-8 Thermograph of same type I specimen as Fig. 6-7, after subsequent 10,000 cycles of tension-tension fatigue loading

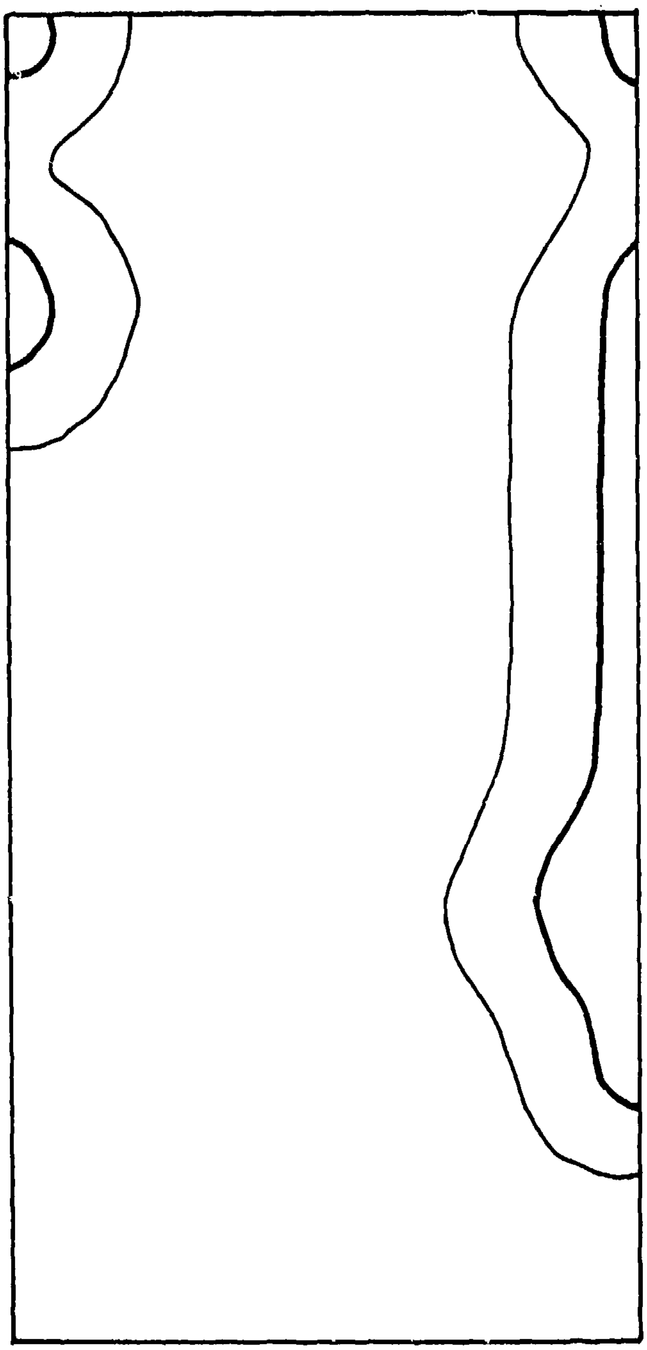

Fig. 6-9 Computer generated thermograph for type I specimen, modeling damage observed in Fig. 6-8

fractured at the hole and a delamination then ran up from one side of the crack into the specimen. The three intense heat sources in line with the hole, as seen in Fig 6-10, show the location of the crack. The remaining two heat sources away from the crack apparently show the limits of the delamination. The shape of these hot spots would indicate that the delamination lies between the off-angle plies. The obvious "V" formed in the temperature pattern between these two intense heat sources seems to show the ±45 degree lines of the fibers in these plies. This strong influence of the ±45 degree plies could be a result of the actual sources of heat being located between these plies. After appropriate changes were made in the program to model the new stacking sequence and the material properties of boron-epoxy, the damage indicated in Fig 6-10 was modeled as being in the second layer down from the surface, elements 20, 22, 29, 30, 41, 44, 49 and 50. The resulting temperature pattern, Fig 6-11, shows a good resemblance to the experimental vibrothermograph.

Two graphite epoxy plates, $[(0,90)_2]_s$, three inches by eight inches (7.62 by 20.32 cm) were manufactured with several flaws deliberately included. These specimens were cured at a pressure of 100 psi (0.7 MPa) for a period of four hours, the first two hours at a temperature of 250°F (121°C), and the second two hours at 350°F (177°C). Both the temperature and the pressure were then allowed to gradually return to ambient levels.

In the first of these plates, two pieces of waxed paper were included at the midplane of the specimen. A one inch square of the paper was placed near one end of the plate and a one inch "T" was placed near the other end. One layer away from the midplane and in the center of the specimen, a diamond shaped piece of plastic sheet was inserted. Two layers away from the midplane and near the base of the "T", two small,

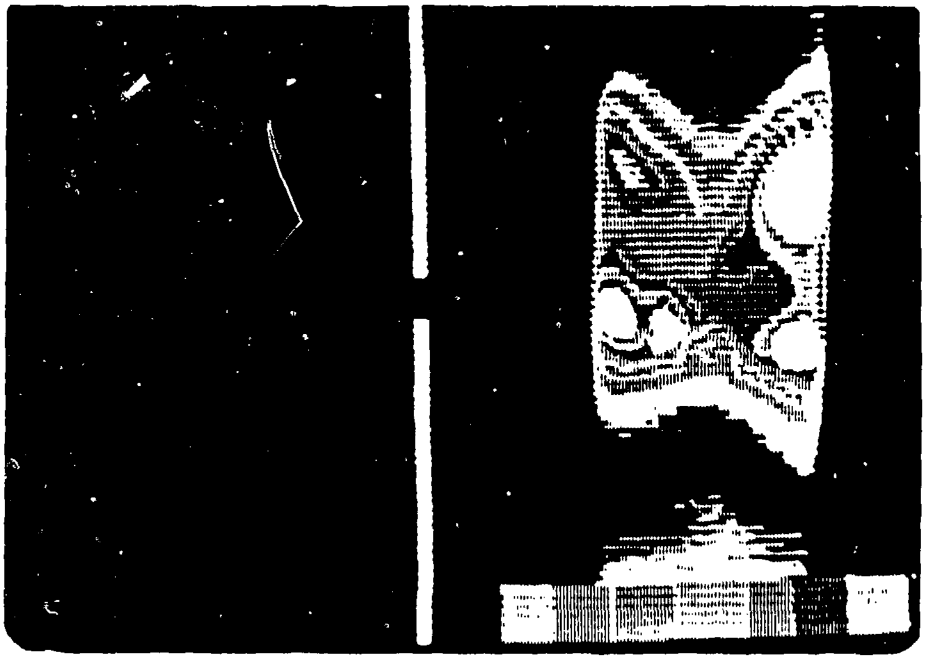

Fig. 6-10 Thermograph of boron-epoxy $[0,\pm45,0]_s$ after loading in three-point bending

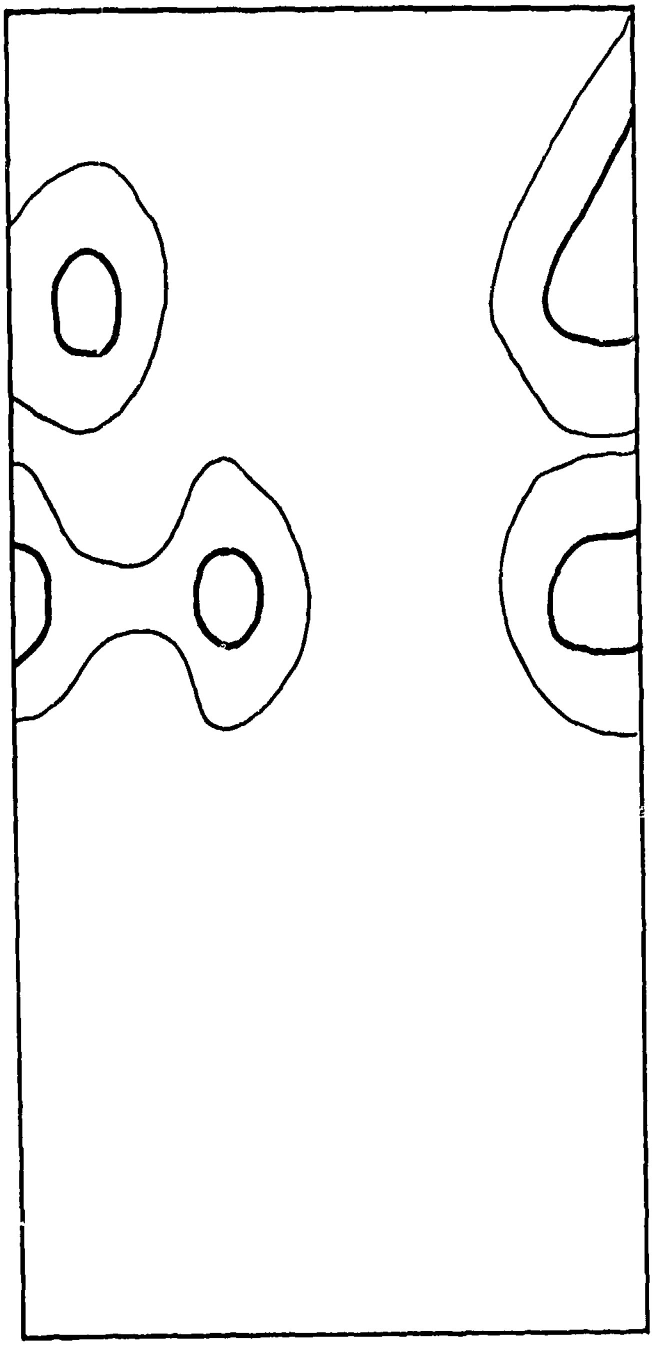

Fig. 6-11 Computer generated thermograph modeling damage observed in Fig. 6-10

thin smears of graphite grease were included. The relative locations of all of these inclusions can be seen in Fig 6-12. All of these inclusions were intended as synthetic delaminations in the cured specimen. With the use of vibrothermography, each of the synthetic flaws, with the exception of the graphite grease smears, were successfully located. Figures 6-13 and 6-14 show the temperature patterns produced by the square and the "T" inclusions, respectively. Figure 6-15 shows the vibrothermograph produced by the plastic, diamond shaped inclusion. A close-up of this picture is seen in Fig 6-16. Here, the top half of the diamond shaped temperature pattern produced by the plastic inclusion can be seen at the bottom of the thermograph. The temperature pattern produced by the waxed paper "T" can be seen at the top of this figure. The relative intensity of the temperature patterns produced by these two different types of inclusions can be noted. While the grease smears could not be located, it is believed that the sparing amount of grease used and its proximity to the edge of the specimen allowed enough of the grease to be removed from the specimen during curing to allow an adequate bond to form in this area.

Since the defect in this specimen was intentionally created during fabrication, the approximate defect shape was known. For the case of the square inclusion, the defect shape was modeled as middle ply, elements 24, 25, 26, 34, 35, 36, 44, 45 and 46. The temperature pattern resulting from the simulation of this problem is seen in Fig 6-17. A comparison of Fig 6-17 with Fig 6-13 shows a good resemblance of the temperature patterns. The experimental temperature pattern shows an extension of the high temperature area upward from the square. Since the computer simulation does not show this extension and since it does not extend downward as well, it can be assumed that this extension is not due to

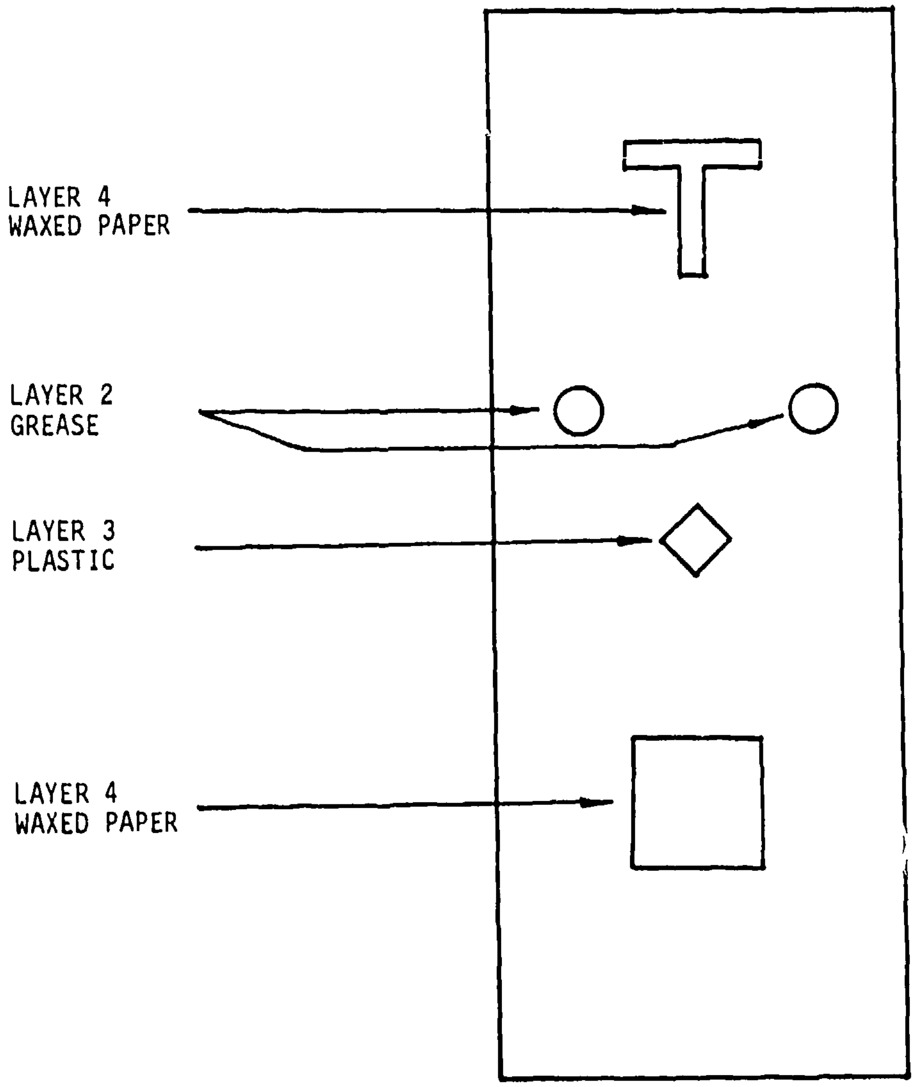
LAYER 4
WAXED PAPER
LAYER 2
GREASE
LAYER 3
PLASTIC
LAYER 4
WAXED PAPER

Fig. 6-12 Schematic diagram of intentionally manufactured flaws in graphite-epoxy laminate

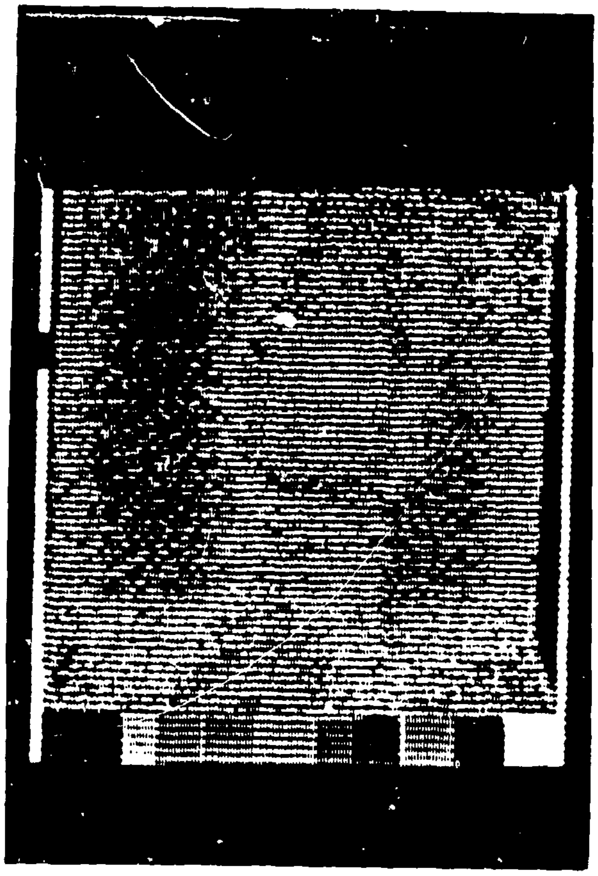

Fig. 6-13 Thermograph showing heat pattern developed by waxed paper square inclusion

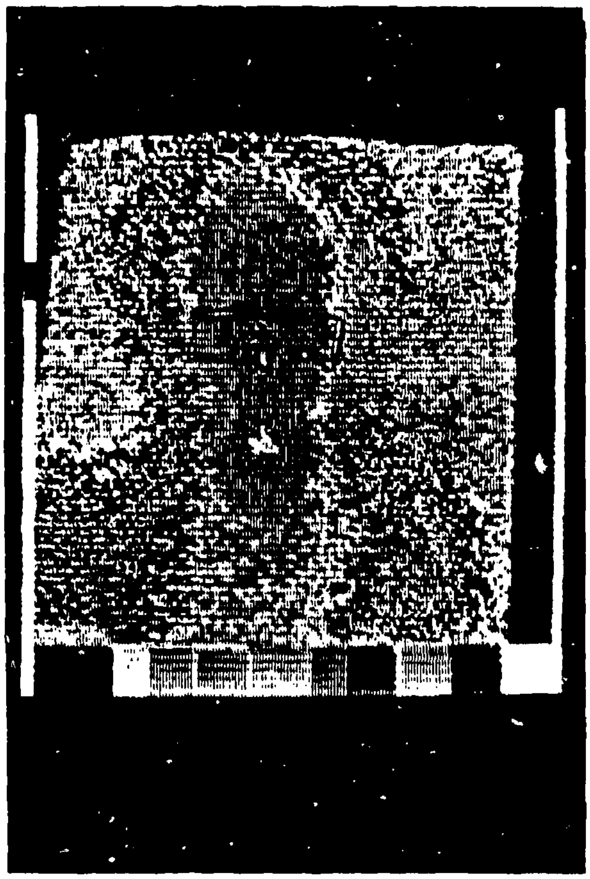

Fig. 6-14 Thermograph showing heat pattern developed by waxed paper "T" inclusion

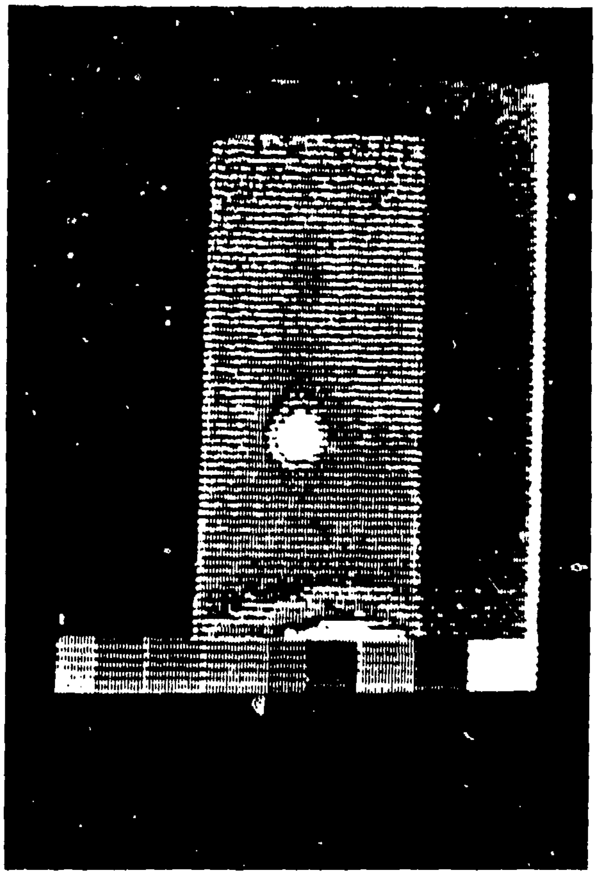

Fig. 6-15 Thermograph showing heat pattern p developed by plastic diamond inclusion

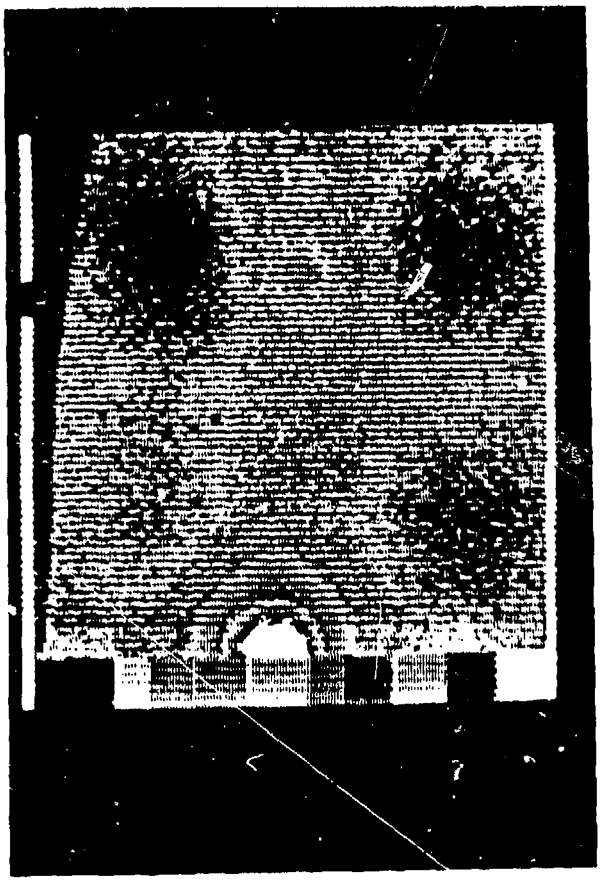

Fig. 6-16 Close-up of thermograph showing heat pattern developed by plastic diamond and waxed paper "T" inclusions

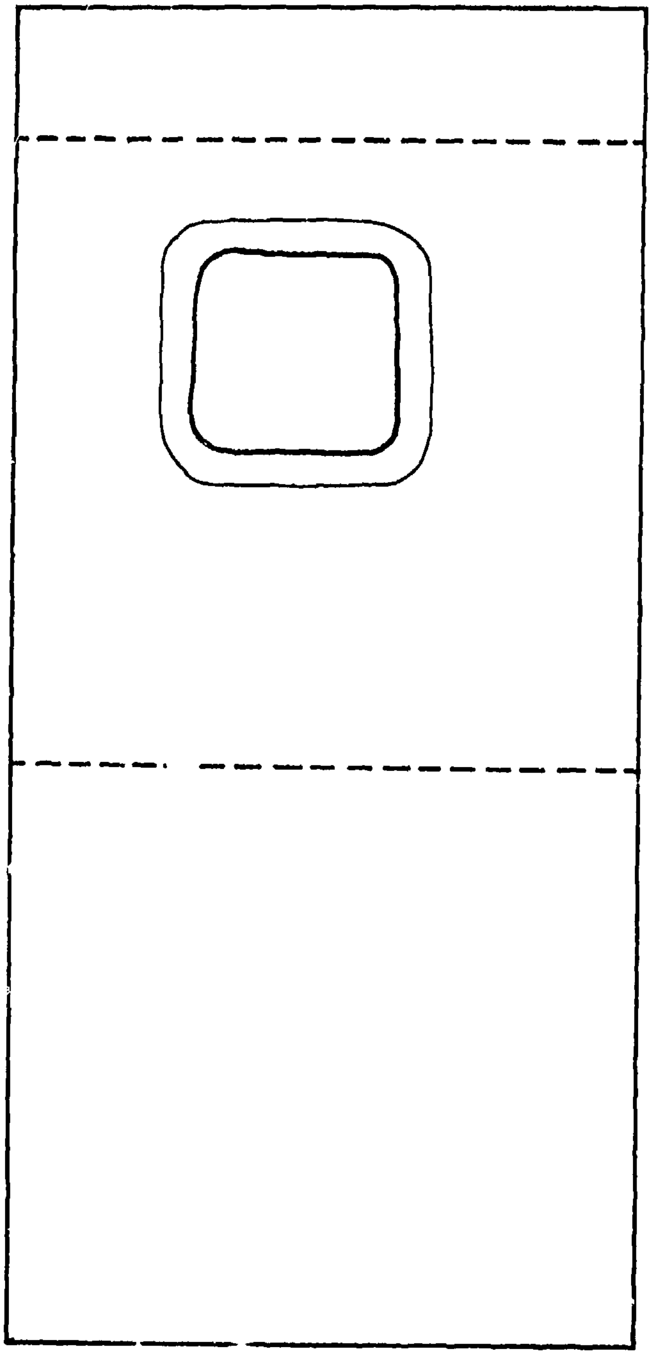

Fig. 6-17 Computer generated thermograph modeling square inclusion in graphite-epoxy laminate

the anisotropic conduction of heat from the square. It is probable that the additional high temperature area is due to a failure of the material bond during curing. This could be a result of having placed the inclusion between the plies relatively near the edge of the specimen.

The experimental thermograph produced by the waxed paper "T" inclusion in the graphite-epoxy plate number one was seen in Fig 6-14. The heat generators responsible for this temperature pattern were modeled as middle layer, elements 24, 25, 26 and 45. A computer simulation with these generators resulted in the pattern in Fig 6-18. A comparison of Fig 6-18 with Fig 6-14 shows only moderately close resemblance. The top part of the "T" is a bit wider in the computer generated pattern. Also, the upward extension of the high temperature pattern can again be seen in the experimentally obtained thermograph as pointed out above. In all cases, except the "T", for which a distinguishable temperature pattern was obtained, the actual shape of the inclusion was clearly visible or at least the entire inclusion appeared to act as a source of heat. In the case of the "T", only the lower tip and the center of the cross appear to act as sources of heat. The reason for this is not fully understood at this time.

The experimentally obtained thermograph produced by the plastic, diamond-shaped inclusion in the graphite-epoxy plate number one was seen in Fig 6-15. The heat sources for this defect were modeled as being in the third layer from the surface, elements 35, 44, 45, 46 and 55. The resulting computer generated temperature pattern for this damage is seen in Fig 6-19. The comparison between the experimental and the computer generated pattern is very good for this case. The diamond shape is a bit more distinctive in the computer generated pattern, but the angular

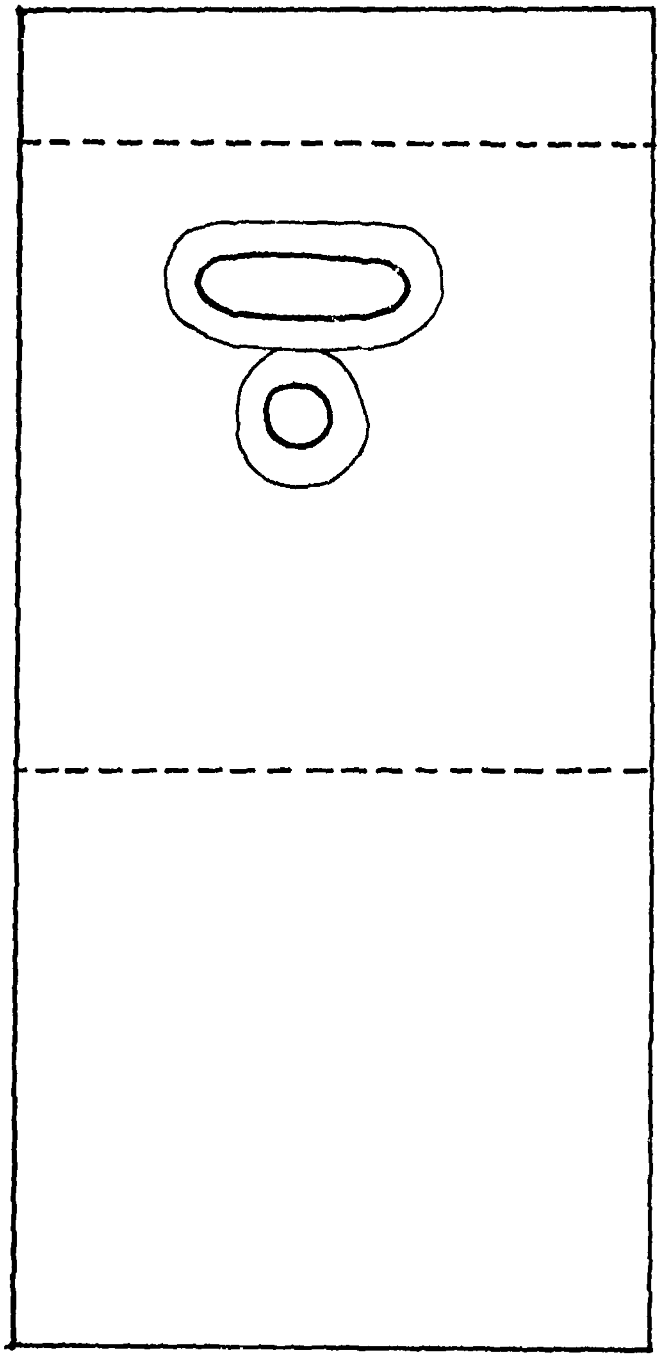

Fig. 6-18 Computer generated thermograph modeling "T" inclusion in graphite-epoxy laminate

sides of the experimental pattern can be seen in both Fig 6-15 and the lower part of Fig 6-16.

A second graphite-epoxy plate $[(0,90)_2]_s$ was fabricated with different materials inserted to represent flawed areas. At the midplane and in the center of the specimen, three small squares of mylar, approximately one-eighth inch by one-eighth inch (0.3 by 0.3 cm), were placed in a row across the width of the specimen. At one end of the specimen and one ply away from the midplane, two squares of teflon release cloth roughly one-half inch square (1.3 by 1.3 cm) were placed side by side. Below the teflon cloth squares and in the same layer, a diamond-shaped piece of mylar about three-eights inch (1.0 cm) across was inserted. At the other end of the plate and still one layer away from the midplane, a dab of graphite grease, about one-quarter inch (0.6 cm) in diameter, was placed. In this case, no effort was made to clean off excess grease as was done in the first of these specimens. Figure 6-20 shows the relative locations of the inclusions in this specimen.

When the vibrothermography technique was applied, the grease spot in this specimen showed up very clearly. The intense temperature pattern around this flaw can be seen in Fig 6-21. The squares of teflon release cloth also showed distinct temperature patterns as can be seen in the thermograph in Fig 6-22. None of the pieces of mylar included in the specimen were visible in the thermographs. It was found after curing that the mylar tends to bond with the epoxy resin reasonably well. If the pieces of mylar included in the specimen did indeed bond to the matrix, this would produce a continuity and very little heat would be generated at the interface.

The computer simulated heat source for the grease dab seen in Fig

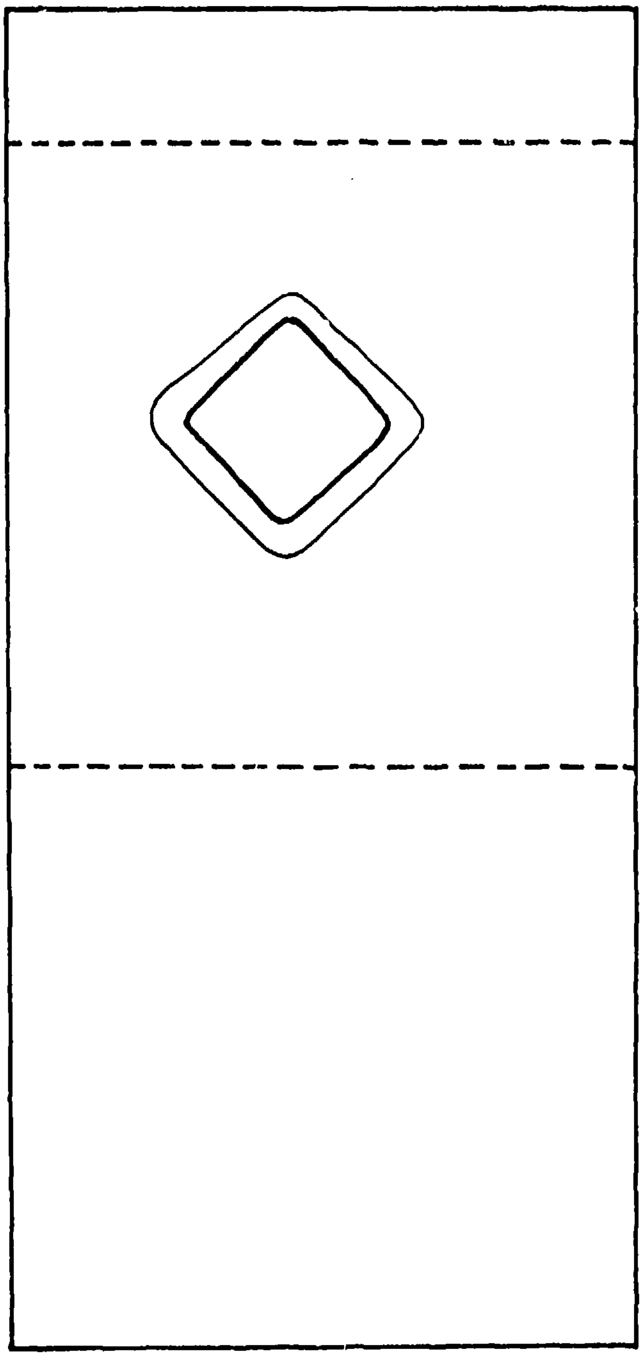

Fig. 6-19 Computer generated thermograph modeling diamond inclusion in graphite-epoxy laminate

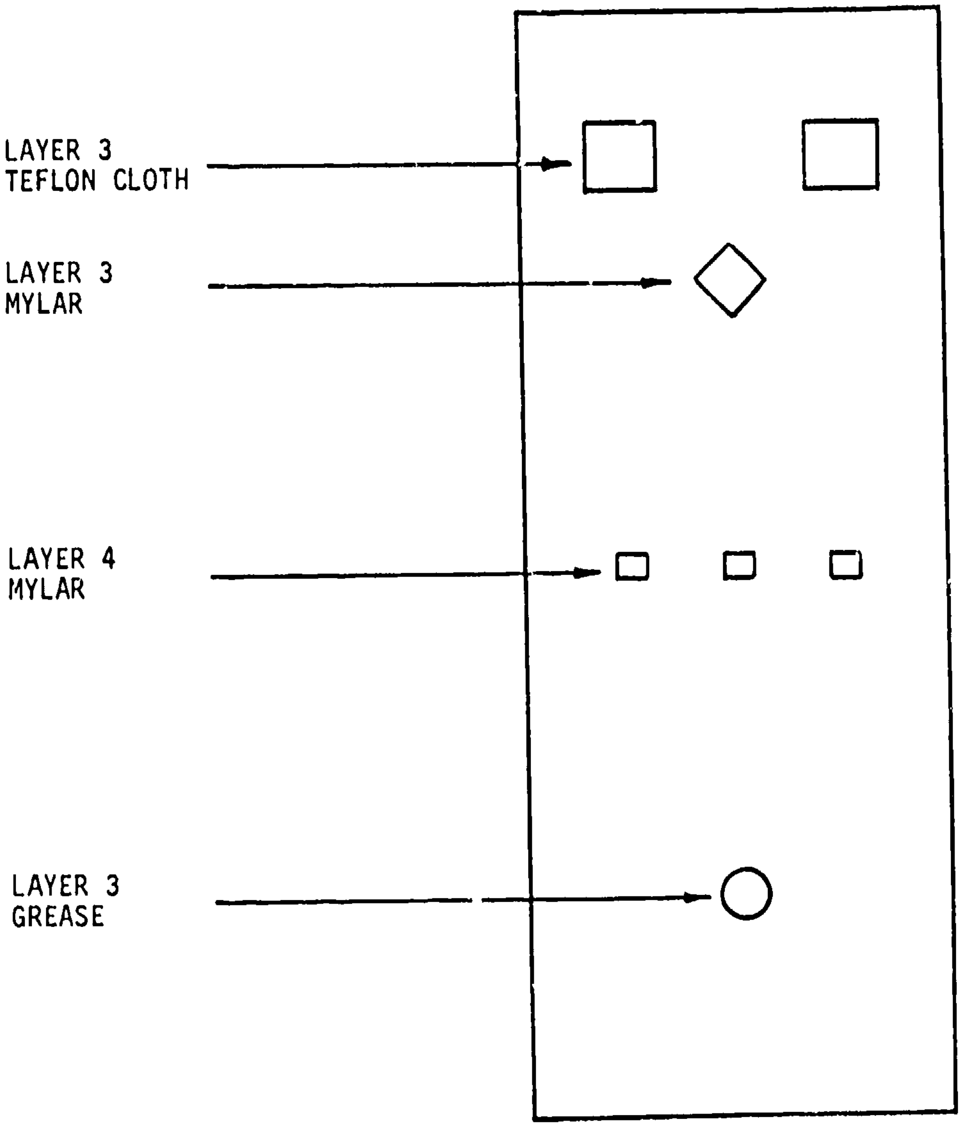
LAYER 3
TEFLON CLOTH
LAYER 3
MYLAR
LAYER 4
MYLAR
LAYER 3
GREASE

Fig. 6-20 Schematic diagram of intentionally manufactured flaws in second graphite-epoxy laminate

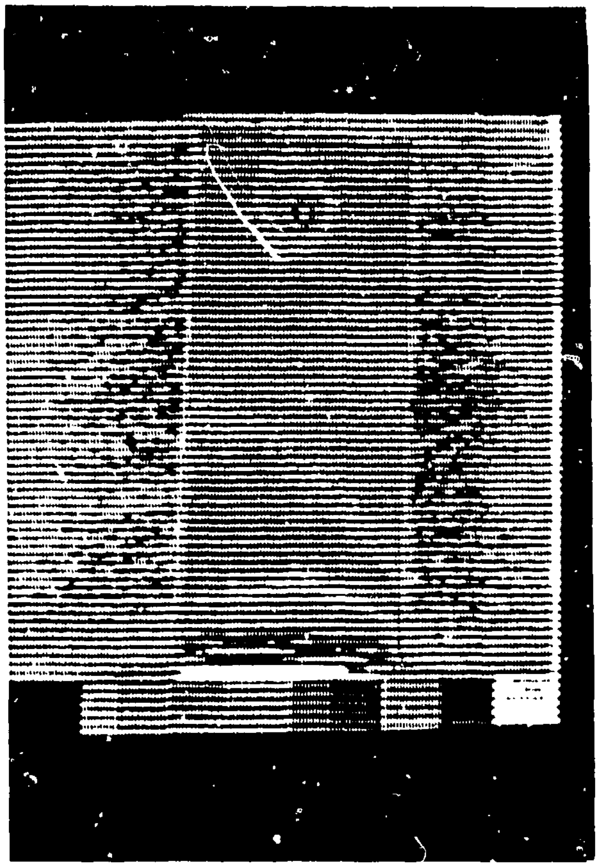

Fig. 6-21 Thermograph showing heat pattern developed by grease dab in second graphite-epoxy laminate

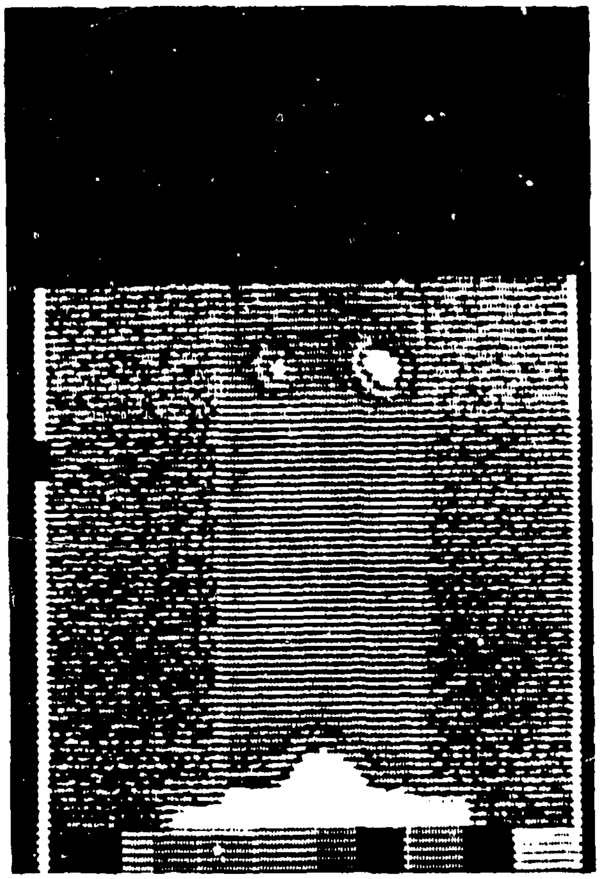

Fig. 6-22 Thermograph showing heat pattern developed by teflon cloth squares in second graphite-epoxy laminate

6-21 was modeled as being in the third layer from the surface, element 25. The resulting thermograph, as seen in Fig 6-23, looks very much like the experimental pattern.

The experimentally obtained temperature pattern resulting from the two teflon cloth sequares was presented in Fig 6-22. For the purposes of the computer analysis of this conduction problem, the damage was modeled as layer three, elements 23, 24, 27, 28, 33, 34, 37 and 38, Fig 6-24. It can be seen in the experimental thermograph that the high temperature pattern on the right appears larger than that on the left. As might be expected, this was not predicted by the computer simulation. The reason for the enlarged pattern on the right in the experimental pattern is not known at this time.

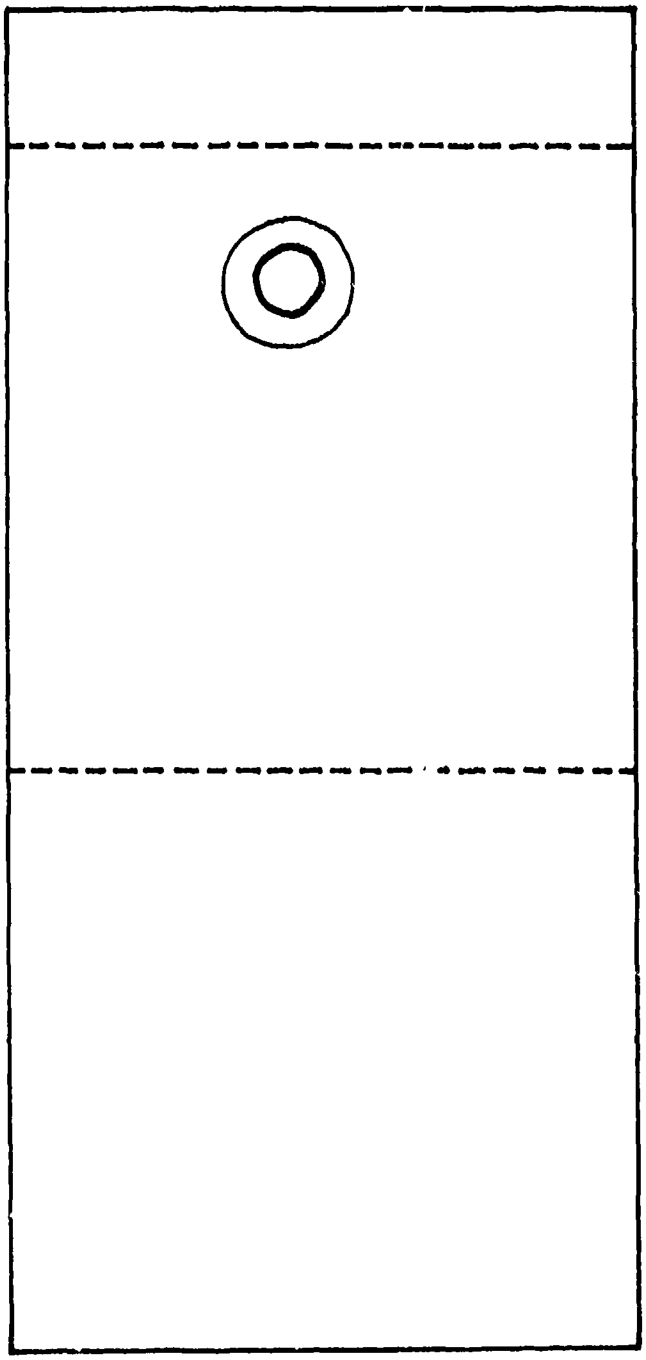

Fig. 6-23 Computer generated thermograph modeling grease dab inclusion in second graphite-epoxy laminate

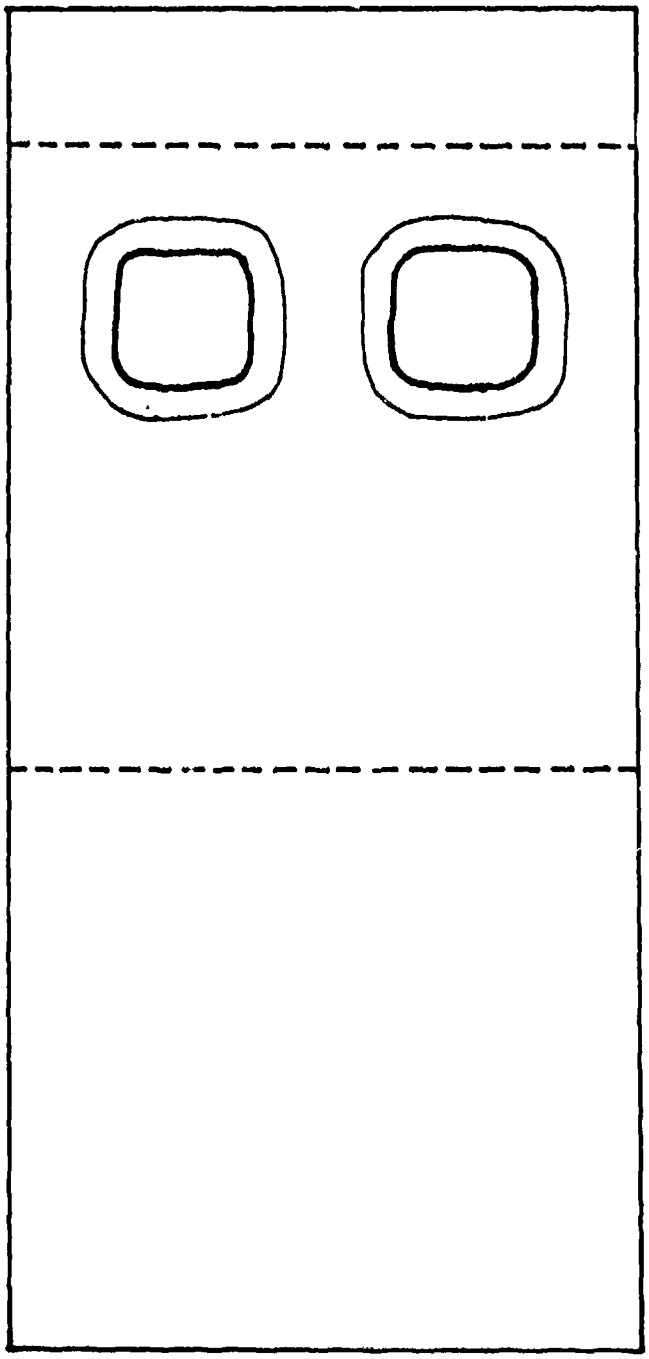

Fig. 6-24 Computer generated thermograph modeling teflon square inclusions in second graphite-epoxy laminate

SECTION VII

CLOSURE

The following items summarize the activity completed during this investigation to date.

1. The precise nature of "first ply failure" has been determined.
2. The effect of thermal residual stress on "first ply failure" has been predicted and demonstrated.
3. A characteristic damage state has been identified and predicted analytically.
4. An effect of stacking sequence on the internal stress distributions in the damaged condition has been identified.
5. An extensive record of internal damage, residual strength, and life as a function of load history has been collected.
6. A one dimensional closed form solution and a three dimensional finite difference solution for stresses around internal damage has been completed.
7. The dependence of the final fracture process on stacking sequence has been investigated.
8. The effect of initial defects has been studied.
9. Several damage mechanisms have been identified.
10. A new ultrasonic technique has been developed which is extremely sensitive to the development of internal damage.
11. A new video-thermography technique called vibrothermography has been developed for the detection and analysis of complex damage in composite materials.
12. The technique of replication has been adapted to composite materials enabling permanent records of surface damage detail to be quickly recorded to facilitate damage development studies.

13. Closed circuit color television (video) recordings of ten-color isotherm video-thermography patterns have been used to investigate the dynamic nature of fracture events, to identify the point of fracture initiation and the nature of the energy release during the fracture event, for example.

These activities have provided a large data base for the development of an understanding and the creation of a philosophy of damage development in laminated composite materials. It is anticipated that this information will support the development of the ability to predict the damaged response of composite laminates based on a rational combination of principals rather than on phenomenological empiricism. The analytical models developed so far should also serve that end.

REFERENCES

1. Smith, C. W., "Limitations of Fracture Mechanics as Applied to Composites," Inelastic Behavior of Composite Materials, Proc. 1975 ASME Winter Annual Meeting, Houston, Texas, C. T. Herakovitch, Ed., pp. 151-169.

2. Reifsnider, K. L., Henneke, E. G., II and Stinchcomb, W. W., "Defect-Property Relationships in Composite Materials," AFML-TR-76-81, (April, 1976).

3. Reifsnider, K. L., Henneke, E. G., II and Stinchcomb, W. W., "Defect-Property Relationships in Composite Materials," AFML-TR-76-81, Part II, (June 1977).

4. Reifsnider, K. L., Henneke, E. G., II and Stinchcomb, W. W., "Delamination in Quasi-Isotropic Graphite-Epoxy Laminates," Composite Materials Testing and Design (Fourth Conference), ASTM STP 617, American Society for Testing and Materials, (1977), pp. 93-105.

5. Stalnaker, D. O., "An Investigation of Edge Damage Development in Quasi-Isotropic Graphite-Epoxy Laminates," Thesis, Department of Engineering Science and Mechanics, School of Engineering, Virginia Polytechnic Institute and State University, (April, 1976).

6. Reifsnider, K. L., "Some Fundamental Aspects of the Fatigue and Fracture Response of Composite Materials," Proc. 14th Annual Society of Engineering Science Meeting, Nov. 14-16, 1977, Lehigh University.

7. Zweben, C., "On the Strength of Notched Composites," Journal of Mechanics and Physics of Solids, Vol. 19, pp. 103-116, 1971.

8. Kulkarni, S. V., McLaughlin, P. V., Jr. and Pipes, R. B., "Fatigue of Notched Fiber Composite Laminates," NASA CR-145039, April, 1976.

9. Kulkarni, S. V. and Rosen, B. W., "Design Data for Composite Structure Safelife Prediction Analysis Evaluation," AFML-TR-73-225, Air Force Materials Laboratory.

10. Trezek, G. J. and Balk, S., "Provocative Techniques in Thermal NDT Imaging," Materials Evaluation, Vol. 34, August, 1976, pp. 172-176.

11. Maewal, A., Bache, T. C. and Hegemier, G. A., "A Continuum Model for Diffusion in Laminated Composite Media," Journal of Heat Transfer, Vol. 98, February, 1976, pp. 133-138.

12. Estes, R. C. and Mulholland, G. P., "Diffusion Through Orthotropic Rectangular Laminated Composites," Fibre Science and Technology, Vol. 7, October, 1974, pp. 257-279.

13. Carslaw, H. S. and Jaeger, J. C., Conduction of Heat in Solids, Oxford University Press, London, 1947.

14. Chapman, A. J., Heat Transfer, MacMillan, New York, 1974.

15. Hofer, K. E., Larsen, D. and Humphreys, V. E., "Development of Engineering Data on the Mechanical and Physical Properties of Advanced Composite Materials," Technical Report AFML-TR-74-266, Air Force Materials Laboratory, Wright-Patterson Air Force Base, Ohio, February, 1975.

16. Hofer, K. E., Rao, N. and Larsen, D., "Development of Engineering Data on the Mechanical and Physical Properties of Advanced Composite Materials," Technical Report AFML-TR-72-205, Part II, Air Force Materials Laboratory, Wright-Patterson Air Force Base, Ohio, February, 1974.

17. Kasen, M. B., "Mechanical and Thermal Properties of Filamentary-Reinforced Structural Composites at Cryogenic Temperatures, 2: Advanced Composites," Cryogenics, December, 1975, pp. 701-722.

☆U.S.Government Printing Office: 1978 — 657-002/212